UNIVERSITY OF CALIFORNIA,
IRVINE

Voltage Control of Spin Waves in Nanostructures

DISSERTATION

submitted in partial satisfaction of the requirements
for the degree of

DOCTOR OF PHILOSOPHY

in Physics

by

Yu-Jin Chen

Dissertation Committee:
Professor Ilya N. Krivorotov, Chair
Professor Zuzanna Siwy
Professor Jing Xia

2017

TABLE OF CONTENTS

LIST OF FIGURES

ACKNOWLEDGMENTS

I would first like to thank my advisor, Professor Ilya Krivorotov, who has given me the great opportunity to study and solve interesting physics problems in his group. He has been patient and supportive throughout my research and has made the frustrations of setbacks much easier to deal with through his pragmatic personality. Most of all, I must thank him for teaching me how to be a good scientist by his example.

My thanks also go to my labmates in the Krivorotov Group, past and present, who have contributed to a positive and cooperative environment. It has been a pleasure to work with such supportive coworkers.

I would especially like to thank Graham Rowlands, who first taught me microwave measurements and magnetic dynamics. He also inspired me to return to my interest in programming and to use that knowledge to improve my research.

I would also like to thank my coworker who worked most closely with me on many of my projects, Han Kyu Lee. He has been a great labmate and friend, who spent many late hours with me discussing projects and making many of the measurements.

I would like to acknowledge the DARPA STT-RAM project that produced the films and knowledge on many of the devices I measured. In particular, I wish to thank Jordan Katine and Patrick Braganca at Western Digital for fabricating the magnetic tunnel junctions and spin wave devices I have measured for my work.

I also wish to thank our theory collaborators Roman Verba, Vasil Tiberkevich, and Andrei Slavin for developing the theory we used to analyze our data and helping to guide the project while it was under way.

Most importantly, I cannot adequately express the gratitude I have for my family and friends who have supported me in my research.

I would like acknowledge the American Chemical Society for publishing part of this work in Nano Letters. Parts of the article are reproduced here as part of detailing the entire experiment. The following is the required statement of permission: Adapted with permission from Nano Lett., 2017, 17 (1), pp 572-577. Copyright 2017 American Chemical Society.

CURRICULUM VITAE

Yu-Jin Chen

EDUCATION

Doctor of Philosophy in Chemical and Material Physics **2017**
University of California, Irvine *Irvine, California*

Master of Science in Chemical and Material Physics **2016**
University of California, Irvine *Irvine, California*

Bachelor of Arts in Physics **2008**
New York University *New York, New York*

RESEARCH EXPERIENCE

Graduate Student Researcher **2010–2017**
University of California, Irvine *Irvine, California*

TEACHING EXPERIENCE

Teaching Associate **Spring 2016**
University of California, Irvine *Irvine, California*

Teaching Assistant **2009–2010**
University of California, Irvine *Irvine, California*

REFEREED JOURNAL PUBLICATIONS

Parametric resonance of magnetization excited by electric field **2017**
Nano Letters

Material parameters of perpendicularly magnetized tunnel junctions from spin torque ferromagnetic resonance techniques **2016**
Applied Physics Letters

Highly textured $IrMn_3$(111) thin films grown by magnetron sputtering **2016**
IEEE Magnetics Letters

Wireless current sensing by near field induction from a spin transfer torque nano-oscillator **2016**
Applied Physics Letters

Magnetic phase transitions in Ta/CoFeB/MgO multilayers **2015**
Applied Physics Letters

Spin torque ferromagnetic resonance with magnetic field modulation **2013**
Applied Physics Letters

Voltage-induced ferromagnetic resonance in magnetic tunnel junctions **2012**
Physical Review Letters

Sub-200 ps spin transfer torque switching in in-plane magnetic tunnel junctions with interface perpendicular anisotropy **2011**
Journal of Physics D: Applied Physics

Switching current reduction using perpendicular anisotropy in CoFeB-MgO magnetic tunnel junctions **2011**
Applied Physics Letters

ABSTRACT OF THE DISSERTATION

Voltage Control of Spin Waves
in Nanostructures

By

Yu-Jin Chen

Doctor of Philosophy in Physics

University of California, Irvine, 2017

Professor Ilya N. Krivorotov, Chair

This dissertation describes the experiments that investigate new methods to control spin waves by electric field. In one experiment, we excite parametric resonance of magnetization in nanoscale magnetic tunnel junctions, which are multilayer thin film devices patterned into nanopillar shape. One of the layers possesses strong perpendicular magnetic anisotropy and exhibits strong voltage-controlled magnetic anisotropy. This magneto-electric effect allows one to modulate the perpendicular magnetic anisotropy of the layer and parametrically excite large-amplitude oscillations of the magnetization. The results of this experiment show that it is possible to parametrically excite resonance in a magnetic nanostructure using electric field and that the threshold voltage for this process is low: it is found to be well below 1 Volt. In addition, we developed nanodevices which allow us to test the effects of voltage-controlled magnetic anisotropy on spin wave propagation. It is hoped that this work will pave the way towards developing energy-efficient spintronic devices based on manipulation of spin waves using electric field.

Chapter 1

Introduction

Manipulation of magnetization by electric field is a central goal of spintronics. Recent progress towards this goal includes magnetization reversal [13, 14] and ferromagnetic resonance [15, 16] driven by electric field. In particular, the effect known as voltage-controlled magnetic anisotropy is a prominent magneto-electric mechanism for controlling magnetization by electric field. This dissertation will describe the experiment that demonstrates how this magneto-electric effect can efficiently manipulate magnetization by electric field through parametric excitation. The results of this experiment further the development of spintronic devices for technologically relevant applications, such as spin wave logic devices. [36] As a continuing work, devices and experiments have been designed to demonstrate the control of spin wave propagation using voltage-controlled magnetic anisotropy.

In chapter 2, I give background information that is necessary for understanding the physics in the experiments and simulations. It will include an overview of several significant effects in nanostructures, such as magnetic tunnel junctions and nanowires, that are used in the experiment. It will also describe the physics of some experimental methods used in characterizing the samples.

In chapter 3, I describe the experiment which demonstrates the ability to excite parametric resonance of magnetization in a nanodevice via electric field. It describes the experimental methods, including specific sample configuration, some details of the preparation of the setup, and the results which are compared to theory.

In chapter 4, I describe the design of nanowire spin wave devices meant to test the control of spin waves by voltage-controlled magnetic anisotropy. In this work, micromagnetic simulation packages are used to model the devices' magnetic behavior. The Object-Oriented MicroMagnetic Framework software and the MuMax3 software were used to predict applications of voltage-controlled magnetic anisotropy for controlling spin waves in nanowires.

In chapter 5, I describe the characterization of a nanomagnet's thermal stability by measuring the Stoner-Wohlfarth astroid as a function of temperature. The astroid characterizes the nanomagnet's switching behavior due to magnetic field, which is a measure of the nanomagnet's anisotropy energy.

Finally, I present a short summary of the work and discuss future work and outlook in chapter 6.

Chapter 2

Background

2.1 Magnetic Tunnel Junctions

The devices under study are nanoscale magnetic tunnel junctions (MTJs), which in their most basic form are trilayer structures with two ferromagnetic layers separated by an insulating layer. As depicted in FIg. 2.1, typical thicknesses of the layers range from a few nanometers down to less than one nanometer. Typically, MTJs are patterned into a nanopillar structures with lateral dimensions that range from sub-micron down to tens of nanometers.

One useful property of MTJs is the tunneling magnetoresistance (TMR) effect, with which we can electrically read out the relative orientation of the ferromagnetic layers by measuring the resistance of the MTJ. The tunneling magnetoresistance value then describes the difference in resistance between the parallel (low resistance) and anti-parallel (high resistance) orientations of the two magnetizations.

$$TMR = \frac{R_{AP} - R_P}{R_P} \tag{2.1}$$

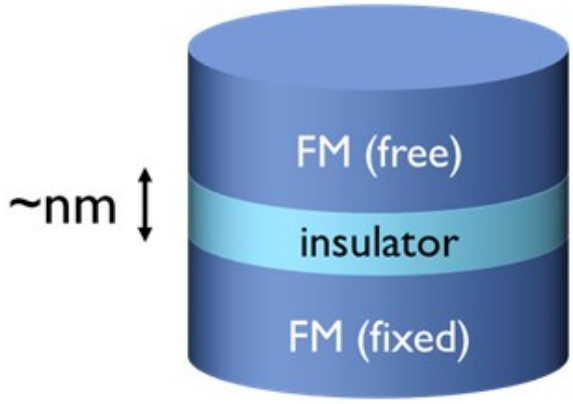

Figure 2.1: **Magnetic tunnel junction.** Schematic of a magnetic tunnel junction, a nanoscale trilayer structure with two ferromagnets separated by an insulating spacer.

The TMR model developed by Julliere [11]) is schematically illustrated in Fig. 2.2 and is valid for amorphous barriers. The origin of the effect is attributed to spin-dependent tunneling through the MTJ's insulating barrier when voltage is applied perpendicular to the plane of the MTJ layers (CPP or current-perpendicular-to-plane geometry). The electrons must tunnel through the insulating barrier, and the tunneling conductance of the MTJ depends on the density of states for majority and minority bands of both ferromagnets:

$$G \propto D_{\uparrow,1} D_{\uparrow,2} + D_{\downarrow,1} D_{\downarrow,2} \tag{2.2}$$

$$G_p \propto D_1^{maj} D_2^{maj} + D_1^{min} D_2^{min} \tag{2.3}$$

$$G_{Ap} \propto D_1^{maj} D_2^{min} + D_1^{min} D_2^{maj}. \tag{2.4}$$

Here G_P and G_{AP} are the conductances for the parallel and anti-parallel magnetization configurations, respectively. The $D_\uparrow$ and $D_\downarrow$ are the density of states for up and down spins, respectively, and the superscripts maj and min denote majority and minority bands, respectively. The numbers 1 and 2 denote the corresponding ferromagnet. As shown in Fig. 2.2 and equations (2.3) and (2.4), the current is essentially split into two currents. The majority band dominates in the parallel case and ends up being the high conductance (low

resistance) state while the anti-parallel case results in low conductance for both channels (high resistance).

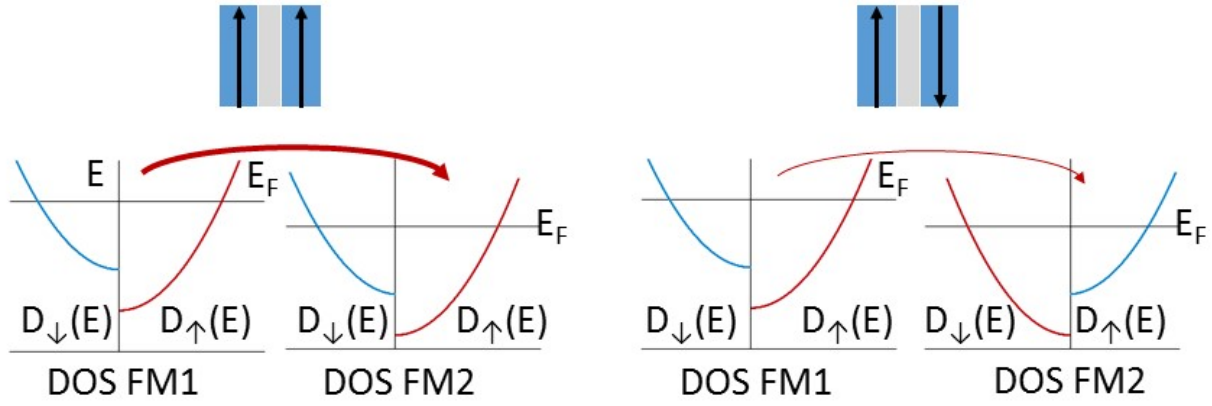

Figure 2.2: **Tunneling magnetoresistance schematic.** Basic schematic of tunneling magnetoresistance through an amorphous barrier. The different orientations of magnetization lead to different density of states and therefore different tunneling conductance.

Tunneling through crystalline MgO barriers is more complex but also results in different resistance states depending on relative orientation of the magnetizations. The conductance is strongly dependent on the density of states of the Bloch states. In particular, it is strongly dependent on the symmetry of the Bloch states in the ferromagnets as well as the evanescent states in the insulator. These, in turn, depend on the relative orientation of the magnetizations of the ferromagnets. [10]

The TMR effect by itself does not help to study magnetization dynamics if both layers in the MTJ are free to move and thus obscure the finer details of the behavior of a single ferromagnet. To compensate for this, there are several ways to effectively pin one of the layers against easy manipulation by magnetic field. One way is to simply make one of the layers thicker, thereby requiring more energy to rotate the magnetization. Another way is to place an antiferromagnet adjacent to one of the layers. This couples the ferromagnetic layer to the antiferromagnet by exchange bias [6] and can leave the ferromagnet strongly pinned.

In our structures, both methods are used to pin one of the ferromagnetic layers (called the fixed layer), and the layer that is relatively easy to manipulate is called the free layer.

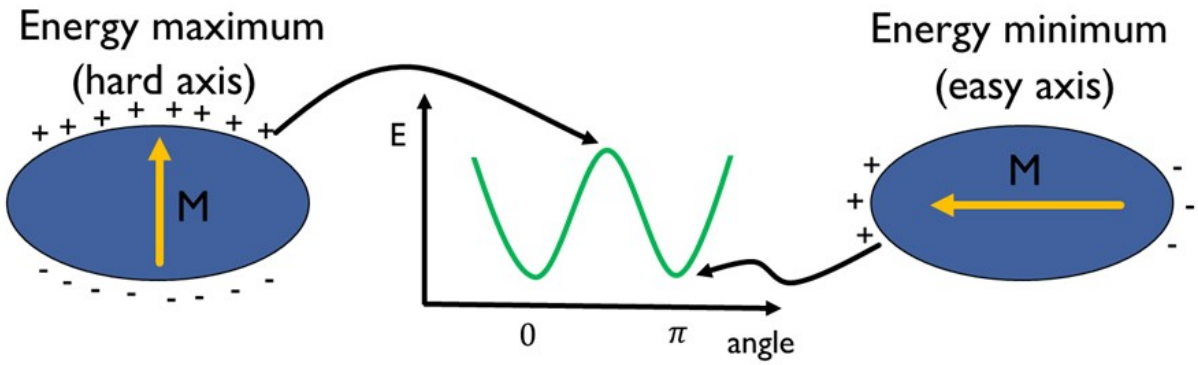

Figure 2.3: **Shape anisotropy.** Shape anisotropy creates stable states for the free layer magnetization. In the case of uniaxial anisotropy, the magnetization prefers to lie along an easy axis (parallel or anti-parallel).

Typically, the MTJs we study are patterned into nanopillar structures, and the lateral cross section can be a non-circular shape. Often, as in this thesis, we use samples that have elliptical cross section, as shown in Fig. 2.3. This gives rise to an in-plane shape anisotropy (a preferred direction for magnetization) that also helps to define the parallel and anti-parallel orientations of the magnetization. The shape anisotropy is due to the demagnetization energy, which arises from buildup of magnetic charge at the boundaries of a sample due to the shape of the sample. [6] In the case of a uniaxial anisotropy, the magnetization lies along a preferred easy-axis (or along a preferred easy-plane). In particular, the parallel and anti-parallel alignments of the free and fixed layers are usually along the easy-axis of the sample.

In order to read orientations of magnetizations other than parallel or anti-parallel, the resistance of the structure must be determined for intermediate angles. The angular dependence

of the *conductance* is modelled as:

$$G(\theta) = \langle G \rangle (1 + P_1 P_2 \cos(\theta)) \tag{2.5}$$

where $\langle G \rangle = (G_P + G_{AP})/2$ is the average of the parallel and anti-parallel state conductances, P_1 and P_2 are the spin polarizations of each ferromagnet, and the angle θ is the angle between the magnetizations of the two layers. [1] This makes the conductance proportional to the projection of the free layer magnetization along the direction of the fixed layer.

2.2 Magnetization Dynamics

Magnetization dynamics for a single spin (or macrospin) is often instructive when trying to understand the dynamics of the free layer in a magnetic nanostructure. The macrospin magnetization dynamics can be described by the Landau-Lifshitz-Gilbert (LLG) equation, which has the form:

$$\frac{\mathrm{d}\mathbf{M}}{\mathrm{d}t} = -\gamma \mathbf{M} \times \mathbf{H}_{\text{eff}} + \frac{\alpha}{M_s} \mathbf{M} \times \frac{\mathrm{d}\mathbf{M}}{\mathrm{d}t} \tag{2.6}$$

where $\mathbf{M}$ is the magnetization (with M_s as the saturation magnetization), γ is the gyromagnetic ratio, $\mathbf{H}_{\text{eff}}$ is the effective field, and α is the Gilbert damping. The effective field $\mathbf{H}_{\text{eff}}$ is the gradient of the free energy with respect to the magnetization and typically includes contributions from exchange field, demagnetization, anisotropy, and applied field. [9]

The first term causes the magnetization to precess around the effective field, which is also the equilibrium direction of magnetization in the steady state ($d\mathbf{M}/dt = 0$). The second term is the phenomenological Gilbert damping term that represents dissipation in the system and tends to decrease the amplitude of precession and realign the magnetization with the equilibrium direction.

2.3 Spin Transfer Torque

Besides manipulation by magnetic field, the free layer of the MTJ can be manipulated by injection of electric current. In 1996, Slonczewski [2] and Berger [3] independently predicted the effect known as spin transfer torque (STT), also referred to as spin torque (ST). The origin of the effect comes from mutual exchange of angular momentum between the local magnetization and the polarization of electron spins in the current. A ferromagnet acts as a spin filter at its interface, absorbing the transverse components of spin angular momentum and leaving a spin-polarized current exiting the ferromagnet. The spin-polarized current is polarized collinear to the ferromagnet, and when this current is injected into another spin filter (another ferromagnet), the same spin filtering effect occurs (see Fig. 2.4). The components of the polarization transverse to the magnetization of the second ferromagnet are absorbed and apply a torque to the magnetization, which is the spin transfer torque.

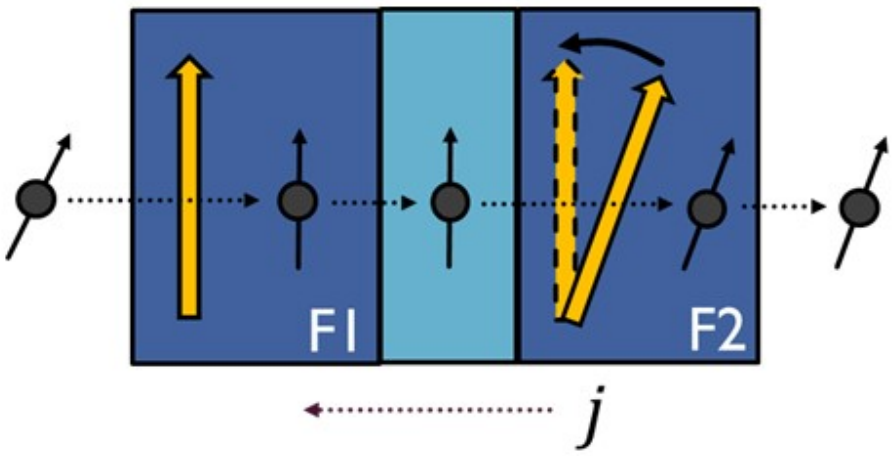

Figure 2.4: **Spin transfer torque.** Spin filtering at the interfaces of ferromagnets leads to spin-polarized currents and the spin transfer torque effect. j is the direction of conventional current, and the circles traveling through the layers represent electron current.

Therefore, the spin-polarized current would apply a torque to the magnetization of the second ferromagnet if the spin polarization of the current and the magnetization are non-collinear.

The torque tends to mutually align the polarization of the current and the magnetization, as shown in Fig. 2.4 and Fig. 2.5.

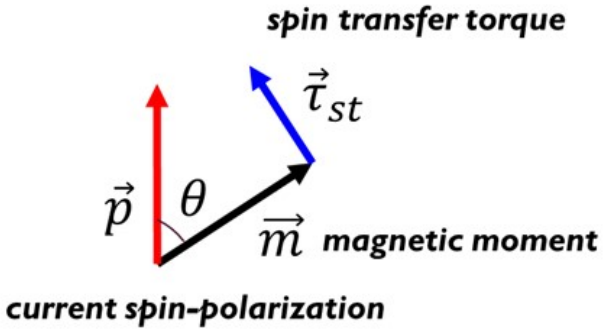

Figure 2.5: **Direction of spin transfer torque.** The spin transfer torque acts to either align or turn away the magnetization from its direction of spin polarization. The torque is proportional to the current and therefore changes sign on reversal of the current polarity.

Magnetization dynamics in the presence of spin torque can be described by the addition of a spin torque term to the LLG equation. The new equation is known as the Landau-Lifshitz-Gilbert-Slonczewski (LLGS) equation, which has the form:

$$\frac{\mathrm{d}\mathbf{M}}{\mathrm{d}t} = -\gamma \mathbf{M} \times \mathbf{H}_{\text{eff}} + \frac{\alpha}{M_s} \mathbf{M} \times \frac{\mathrm{d}\mathbf{M}}{\mathrm{d}t} - \beta(I) g(\theta) \mathbf{M} \times (\mathbf{M} \times \mathbf{p}) \tag{2.7}$$

where $\beta(I)$ is proportional to the current and represents the magnitude of the spin torque, $g(\theta)$ is the angular dependence of the spin torque, and $\mathbf{p}$ is the unit vector describing the spin-polarization of the current. [2, 9] The spin torque term contains a double cross product that captures the geometry of the angular momentum transfer, and the term is proportional to the polarity and amplitude of injected current (see Fig. 2.5).

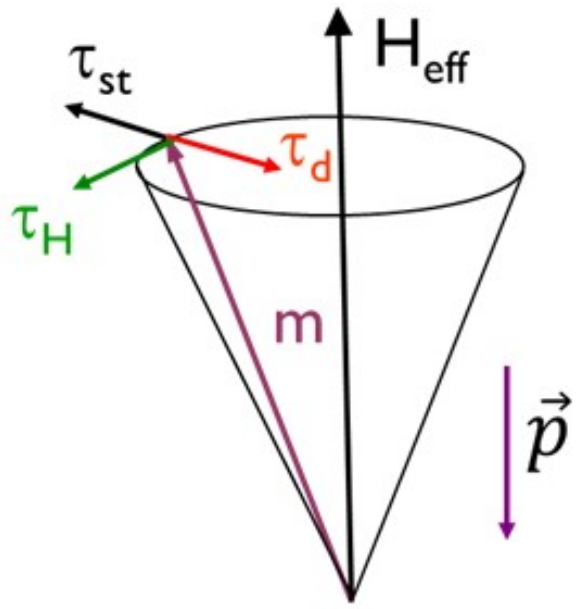

Figure 2.6: **Magnetization dynamics torque diagram.** Schematic of torques for magnetization dynamics involving spin torque. The τ_H is the field and precession torque, the τ_d is the damping torque, and the τ_{ST} is the spin transfer torque. The spin transfer torque can act as anti-damping if the polarization is opposite to the direction of the effective field.

In the appropriate geometry, the spin torque term can act as anti-damping, as shown in Fig. 2.6. This happens when the polarization of the spin current has a component opposite to the direction of effective field. When this is the case, there are three possible regimes of excited magnetization dynamics: damped oscillations, steady-state precession, and switching of the ferromagnet. [2, 9] In the low-current regime, damping still dominates over the effect of spin torque, and the resulting oscillations continue to damp towards the equilibrium direction. In a high current regime, the energy delivered to the system by spin torque cancels the energy lost due to damping and a steady-state precession can occur. At yet higher currents, the spin torque becomes strong enough to overcome the anisotropy energies and reverses direction of the magnetization.

2.4 Voltage-Controlled Magnetic Anisotropy

In addition to spin torque, there has been great interest in manipulation of magnetization by electric field, which relies on the magneto-electric (ME) effect in magnetic solids [18]. One prominent manifestation of the ME effect is modification of magnetic anisotropy in response to applied electric field [24, 25, 26]. A recently discovered ME effect at the interface between a ferromagnetic metal (e.g. Fe) and a non-magnetic insulator (e.g. MgO) [26, 27, 28, 29] is promising for ultra-fast manipulation of magnetization in nanoscale spintronic devices [14]. This interfacial ME effect called voltage-controlled magnetic anisotropy (VCMA) originates from different rates of filling of d-like electron bands at the Fe/MgO interface in response to electric field applied perpendicular to the interface. Since electrons in different bands contribute unequally to the uniaxial perpendicular magnetic anisotropy (PMA) at the Fe/MgO interface, electric field modulates PMA [28, 29]. This electric field induced anisotropy is promising for energy-efficient manipulation of magnetization because, unlike spin torque, it does not rely on high electric current density resulting in large Ohmic losses [30].

VCMA appears in the LLG as an anisotropy term in the effective field. One can write the first-order uniaxial anisotropy energy density as:

$$\varepsilon = K_{u1}\sin^2(\theta) = K_{u1}(1-(\mathbf{m}\cdot\mathbf{u})^2). \tag{2.8}$$

Here, K_{u1} is the uniaxial anisotropy constant, $\mathbf{m} = \mathbf{M}/M_s$ is the normalized magnetization, and the unit vector $\mathbf{u}$ is along the symmetry axis of the uniaxial anistropy. The VCMA effective field is then:

$$\mathbf{H}_{\text{VCMA}} = -\frac{1}{M_s}\frac{\partial\varepsilon}{\partial\mathbf{m}} = \frac{2K_{u1}}{Ms}(\mathbf{m}\cdot\mathbf{u})\mathbf{u}. \tag{2.9}$$

This leaves the torque due to VCMA as:

$$\tau_{VCMA} = -\gamma \mathbf{M} \times \mathbf{H}_{\mathrm{VCMA}} \propto \frac{2K_{u1}}{Ms} \cos(\theta) \sin(\theta). \tag{2.10}$$

The torque is then maximized when the angle between magnetization and the uniaxial anisotropy axis is at 45 degrees. In the experiment described later, it is not the direct VCMA torque that plays a role in exciting magnetization dynamics but the modulation of the uniaxial anisotropy energy.

2.5 Ferromagnetic Resonance (FMR)

One standard technique to measure magnetic properties of materials is the ferromagnetic resonance (FMR) technique. In the typical measurement geometry, the sample is placed in a magnetic field that, ideally, can saturate the sample. A small amplitude microwave magnetic field (small compared to the static field and the magnetization) is applied perpendicular to the external field direction. When in the saturated state, the excitation field is also perpendicular to the static magnetization direction.

Using the magnetization dynamics described by the LLG (Eq. (2.6)), the response of the magnetization to the external microwave field results in resonance. One can derive the expression for the resonance condition, the external field at which a magnetic sample will resonate for a given frequency of the microwave drive (or vice versa). In addition, one can derive an expression for the lineshape of the measured FMR spectra.

We begin with a few simple assumptions. The magnetization, which will be the $+\mathbf{z}$ direction in our Cartesian coordinate system, is aligned to the external field direction. The microwave excitation field $\mathbf{h}$ is applied perpendicular to the magnetization, in the $x - y$ plane, and is

assumed to be spatially uniform. The magnetization response can be expressed as:

$$\mathbf{m} = \chi \cdot \mathbf{h} \tag{2.11}$$

where $\mathbf{m}(t) = (m_x \exp^{i\omega t}, m_y \exp^{i\omega t}, m_z(t))$ is the dynamic magnetization, χ is the susceptibility tensor, and $\mathbf{h} = (\mathbf{h}_x \exp^{i\omega t}, \mathbf{h}_y \exp^{i\omega t}, 0)$ is the microwave excitation field.

Starting from the LLG, we have:

$$\frac{\mathrm{d}\mathbf{M}}{\mathrm{d}t} = -\gamma \mathbf{M} \times \mathbf{H}_{\text{eff}} + \frac{\alpha}{M_s} \mathbf{M} \times \frac{\mathrm{d}\mathbf{M}}{\mathrm{d}t} \tag{2.12}$$

where $\mathbf{M} = M_s \mathbf{z} + \mathbf{m}$ and $\mathbf{H}_{\text{eff}} = H_{ext}\mathbf{z} + \mathbf{H}_{\text{an}} + \mathbf{h}$. H_{ext} is the external applied field, $\mathbf{H}_{\text{an}}$ represents the anisotropy fields, and M_s is the saturation magnetization.

Assuming we have purely uniaxial anisotropies, the effective field becomes

$$\mathbf{H}_{\text{eff}} = (h_x - N_x m_x) e^{i\omega t} \mathbf{e}_x + (h_y - N_y m_y) e^{i\omega t} \mathbf{e}_y + H_{ext} \mathbf{e}_z, \tag{2.13}$$

and the magnetization is

$$\mathbf{M} = m_x e^{i\omega t} \mathbf{e}_x + m_y e^{i\omega t} \mathbf{e}_y + M_s \mathbf{e}_z \tag{2.14}$$

where we have assumed that $m_z(t) \approx 0$ for small angle oscillations.

Each term of the LLG is then

$$\frac{\mathrm{d}\mathbf{M}}{\mathrm{d}t} = i\omega m_x e^{i\omega t}\mathbf{e}_x + i\omega m_y e^{i\omega t}\mathbf{e}_y \tag{2.15}$$

$$-\gamma\mathbf{M}\times\mathbf{H}_{\text{eff}} = -\gamma\begin{vmatrix} \mathbf{e}_x & \mathbf{e}_y & \mathbf{e}_z \\ m_x e^{i\omega t} & m_y e^{i\omega t} & M_s \\ (h_x - N_x m_x)e^{i\omega t} & (h_y - N_y m_y)e^{i\omega t} & H_{ext} \end{vmatrix} \tag{2.16}$$

$$= -\gamma\Big\{[H_{ext}m_y - (h_y - N_y m_y)M_s]\mathbf{e}_x \tag{2.17}$$

$$+ [(h_x - N_x m_x)M_s - H_{ext}m_x]\mathbf{e}_y\Big\}e^{i\omega t} \tag{2.18}$$

$$\frac{\alpha}{M_s}\mathbf{M}\times\frac{\mathrm{d}\mathbf{M}}{\mathrm{d}t} = \frac{\alpha}{M_s}\begin{vmatrix} \mathbf{e}_x & \mathbf{e}_y & \mathbf{e}_z \\ m_x e^{i\omega t} & m_y e^{i\omega t} & M_s \\ i\omega m_x e^{i\omega t} & i\omega m_y e^{i\omega t} & 0 \end{vmatrix} \tag{2.19}$$

$$= \frac{\alpha}{M_s}(-i\omega M_s m_y\mathbf{e}_x + i\omega M_s m_x\mathbf{e}_y)e^{i\omega t} \tag{2.20}$$

where second order terms have been dropped (e.g., $m_x h_y$).

This results in the following coupled equations:

$$i\omega m_x = -\gamma[H_{ext}m_y - (h_y - N_y m_y)M_s] - i\alpha\omega m_y \tag{2.21}$$

$$i\omega m_y = -\gamma[(h_x - N_x m_x)M_s - H_{ext}m_x] - i\alpha\omega m_x \tag{2.22}$$

which become

$$i\frac{\omega}{\gamma}m_x = -H_{ext}m_y + M_s h_y - N_y M_s m_y - i\alpha\frac{\omega}{\gamma}m_y \tag{2.23}$$

$$i\frac{\omega}{\gamma}m_y = -(h_x - N_x m_x)M_s + H_{ext}m_x - i\alpha\frac{\omega}{\gamma}m_x \tag{2.24}$$

$$\tag{2.25}$$

and finally become

$$i\frac{\omega}{\gamma}m_x + i\alpha\frac{\omega}{\gamma}m_y + N_yM_sm_y + H_{ext}m_y = M_sh_y \tag{2.26}$$

$$-N_xM_sm_x + H_{ext}m_x - i\alpha\frac{\omega}{\gamma}m_x - i\frac{\omega}{\gamma}m_y = M_sh_x \tag{2.27}$$

after rearranging.

$$\begin{bmatrix} i\frac{\omega}{\gamma} & +i\alpha\frac{\omega}{\gamma} + N_yM_s + H_{ext} \\ -N_xM_s + H_{ext} - i\alpha\frac{\omega}{\gamma} & -i\frac{\omega}{\gamma} \end{bmatrix} \begin{bmatrix} m_x \\ m_y \end{bmatrix} = M_s \begin{bmatrix} h_x \\ h_y \end{bmatrix} \tag{2.28}$$

To find the resonance condition, we can take the determinant of the matrix and set it to zero while dropping the α terms in the product:

$$\left(\frac{\omega}{\gamma}\right)^2 - \left(H_{ext} + N_yM_s + i\alpha\frac{\omega}{\gamma}\right)\left(H_{ext} - N_xM_s - i\alpha\frac{\omega}{\gamma}\right) = 0 \tag{2.29}$$

$$\left(\frac{\omega}{\gamma}\right)^2 \approx \left(H_{ext} + N_yM_s + i\alpha\frac{\omega}{\gamma}\right)\left(H_{ext} - N_xM_s - i\alpha\frac{\omega}{\gamma}\right) \tag{2.30}$$

$$\left(\frac{\omega}{\gamma}\right)^2 \approx \left(H_{ext} + N_yM_s\right)\left(H_{ext} - N_xM_s\right) \tag{2.31}$$

2.6 Spin Torque Ferromagnetic Resonance (ST-FMR)

One major application of spin torque to nanomagnetic systems is the spin torque ferromagnetic resonance (ST-FMR) technique. A diagram of the typical circuit for this type of measurement is shown in Fig. 2.7. It consists of a microwave generator, a bias tee, a lock-in amplifier, and optionally a dc bias source of some type (current or voltage). In this technique, an amplitude-modulated microwave current is sent through the ac arm of the bias tee

to the device under test and excites magnetization dynamics. Due to the presence of magnetoresistance effects, magnetic oscillations result in oscillations of the device resistance. The ac resistance oscillations then mix with the ac microwave current to produce a dc rectified voltage. The lock-in amplifier detects the voltage by locking in to the modulation frequency of the microwave drive. [31, 32]

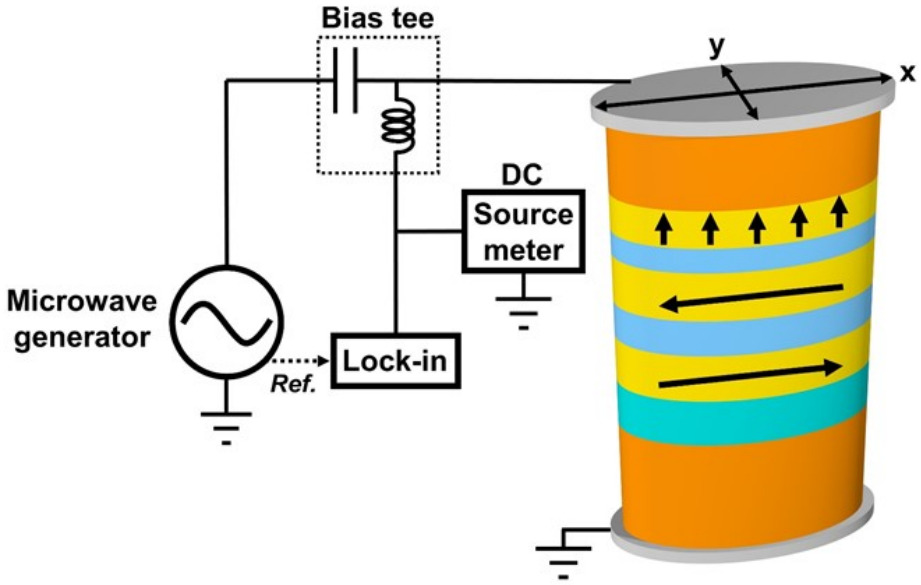

Figure 2.7: **Spin torque ferromagnetic resonance.** Schematic of a spin torque ferromagnetic resonance setup. An amplitude-modulated microwave current is sent through the bias tee to the device and excites magnetization dynamics. The resistance oscillations due to these dynamics mixes with the microwave current to produce a rectified voltage that is detected by lock-in technique.

Typically, one sweeps the microwave drive frequency while holding a constant external magnetic field. When the drive frequency matches that of a magnetic resonance (a spin wave eigenmode), the rectified voltage shows a peak. By changing the applied field, one can record the resonance frequency and field to fit for anisotropy values using the appropriate Kittel formula. One can also fit the linewidth as a function of resonance frequency to obtain a measure of the Gilbert damping of the system. [4] In contrast, conventional ferromagnetic resonance measurements do a field sweep while holding a constant drive frequency. This is

also possible in the ST-FMR setup, and it often results in spectra that are easier to interpret if one is interested in fitting the linewidth for damping.

The lineshapes one can see in the ST-FMR spectra have also been thoroughly studied [33, 32]. The curves can generally be well-fitted to symmetric Lorentzian and anti-symmetric Lorentzian line shapes. The different types of torques have also been associated with different lineshapes. The Slonczewski or in-plane spin torque shows up as a symmetric Lorentzian. There is also the field-like spin torque which results in anti-symmetric Lorentzians. [33] The torque due to VCMA also appears as an anti-symmetric Lorentzian in ST-FMR spectra. [16]

2.7 Micromagnetic Simulations

While the macrospin dynamics described by the LLG equation are applicable to uniformly magnetized elements that also uniformly rotate, non-uniform magnetization profiles arise when magnetic elements become larger than the exchange length:

$$\lambda_{ex} = \sqrt{\frac{2A}{4\pi M_s^2}} \quad \text{(CGS)} \tag{2.32}$$

$$\lambda_{ex} = \sqrt{\frac{2A}{\mu_0 M_s^2}} \quad \text{(SI)} \tag{2.33}$$

where A is the exchange stiffness constant, μ_0 is the permeability of vacuum, and M_s is the saturation magnetization. In micromagnetic simulations, the exchange length is the length within which the magnetization is locally uniform. In this way, the entire magnet can be broken down into smaller pieces of uniform magnetization at an intermediate length [8] between full atomistic calculations (which would be computationally taxing and time-consuming) and a macrospin model (which does not capture complex magnetic states). Typical exchange lengths for Fe or Co based alloys are on the order of 3-5 nm. In the case of Py, with material

parameters $A = 15 \times 10^{-7}\,\mathrm{erg/cm} = 15\,\mathrm{pJ/m}$ and $M_s = 800\,\mathrm{emu/cm^3} = 800,000\,\mathrm{A/m}$, the exchange length is found to be $\lambda_{ex} \approx 6.1\,\mathrm{nm}$.

Micromagnetic texture can develop in nanostructures mainly due to the competition between demagnetization energy and exchange energy: the cost in exchange energy by having non-uniform magnetization is offset by the gains in demagnetization energy. Depending on the exact geoemtry of the sample, magnetic textures such as domain walls, vortices, or more complicated structures can arise.

In nanostructured magnetic elements, many magnetic energies can compete with each other at similar scales and complex electronic and spin transport can take place. Both effects can drive the magnetization into various micromagnetic states. Numerical micromagnetic simulations are often necessary to study these complex dynamics. In this approach, the magnetic sample is discretized in space, and magnetization dynamics described by the LLG are solved for the grid. One can choose either the finite difference method or the finite element method to solve the LLG. In the finite difference approach, the problem is defined on a rectangular grid and is relatively easier to implement. The finite element method, however, allows solutions for a wider range of system geometries.

The most commonly used finite difference micromagnetic package has been the Object-Oriented MicroMagnetic Framework (OOMMF), developed by Michael Donahue and Donald Porter at NIST with contributions from users. GPU-accelerated codes have also become available, such as MuMax. In many cases, the OOMMF file formats have been adopted for output of scalar and vector quantities.

Mainly, I will describe the workings of micromagnetic code as it functions in the OOMMF or MuMax3 packages. Both codes solve the LLG by taking an interative approach, calculating a magnetic state and then comparing the energy difference between the new state and the previous state to determine whether error has occured. In the default setup, both solvers

adapt their timesteps to try to minimize errors within the allowed energy threshold, and deviations force a smaller timestep.

The typical energies considered for each micromagnetic cell are the exchange energy, demagnetization energy, Zeeman energy, and the anisotropy energies. Each of these is accounted for in the calculation of the effective field that appears in the LLG, but calculated on a site-by-site basis. The exchange energy, for example, is typically calculated by using the six nearest neighbor spins. In contrast, the demagnetization energy must be calculated by taking into account the entire magnetic texture. Thus, micromagnetic packages typically implement a Fourier transform approach using the Green functions to speed up calculations.

2.7.1 Analysis

The analysis of micromagnetic simulation data often necessitates a software suite that can be customized for the sample geometry. Much work has been done to develop analysis of micromagnetic spectra and modes. [41]. In our group, I have helped develop our ability to simulate the ferromagnetic resonance spectrum as well as spatial mapping of magnetic resonances at a given frequency. In addition, there has been some work on calculating the spin wave dispersion relation for spatially extended structures.

In order to simulate the ferromagnetic resonance spectrum in a timely manner, it is favorable to use a *sinc* excitation pulse:

$$sinc(\omega_c t) = \frac{sin(\omega_c t)}{\omega_c t} \tag{2.34}$$

where $\omega_c = 2\pi f_c$ is the cut-off (angular) frequency, which is the frequency up to which the magnetization will be excited. One can see in the Fourier transform of the sinc function that the band from zero (DC) up to the cut-off frequency will be non-zero, while the rest of the

spectrum remains zero. The magnetization as a function of time will capture the response to this broadband excitation, and its Fourier transform will reveal the resonance spectrum as a function of frequency. Typically, multiple simulations are run, each at different magnetic fields, so that the resonance frequencies as a function of field can be mapped. Such a mapping can qualitatively capture experimental contributions to magnetic resonance spectra, usually by turning on or turning off different excitation mechanisms in the simulations and comparing with experiment.

When we wish to understand the possible spin wave modes excited in our system, we typically simulate full vector magnetization response to the above mentioned sinc drive. Then, we spatially map the profile of the spin wave by performing a Fourier transform for each cell and mapping the amplitude and phase of the Fourier component at a given frequency as a function of spatial position on the grid. The analysis is usually performed by custom scripts written in Python. One must also remember to take care that the magnetization response as a function of time is given in a uniform time step, since the FFT algorithm in Numpy relies on this. If the magnetization files are not output in uniform time steps (as is the case in MuMax3), then one can interpolate magnetization as a function of time and sample at uniform time steps. This data can then be fed into the FFT analysis.

For the calculation of dispersion relations for nanowire systems, a similar approach is taken. Typically a sinc excitation is applied in the appropriate geometry and full vector magnetization data is output as a function of time. Since this analysis is usually done for large systems like nanowires, this can be very data storage intensive. Care must be taken to store as little data as possible while obtaining the data needed for analysis. Efficient data analysis codes should also be written so that memory consumption on analysis machines does not cause an overload.

2.8 Parametric Excitation

Parametric excitation of magnetic systems is analogous to parametric excitation in classical systems. One prominent example is that of a child on a swing, changing her moment of inertia by moving her legs back and forth in a periodic fashion. The child is modulating a parameter of the system, in this case the moment of inertia of the swing-child pendulum (and thus the resonance frequency), and will excite large-amplitude oscillations at the proper frequency of modulation. This is parametric resonance, and it occurs when a parameter of the system such as the resonance frequency or the damping is modulated at nearly twice the natural frequency of the system.

Parametric excitation of magnetization by external magnetic field has been thoroughly studied in bulk and thin-film ferromagnets [4]. In these experiments, a parameter of the magnetic system (external field) is modulated with a frequency near twice the ferromagnetic resonance frequency f_0 of the system. Parametric excitation is a nonlinear process, in which the parametric drive acts as negative effective magnetic damping competing with positive intrinsic damping [4, 5]. At a threshold amplitude of the parametric drive, the negative damping exceeds the intrinsic damping and magnetization oscillations with a frequency near f_0 are excited.

Parametric excitation of magnetization has several important advantages over direct excitation by external magnetic field with a frequency near f_0. First, parametric excitation efficiently couples not only to the uniform precession of magnetization but also to other spin wave eigenmodes. This allows excitation of short wavelength spin waves by simply choosing the parametric drive frequency to be twice the desired spin wave frequency. Second, parametric pumping can be used for frequency-selective amplification of spin waves [23]. Third, it can be employed for spin wave amplification and phase error corrections [19]. All these properties of parametric pumping are highly desirable for manipulation of magnetization in the

field of nanomagnonics [20, 21]. However, parametric excitation of spin waves by microwave magnetic field in metallic ferromagnets is not energy efficient because of the relatively high threshold fields (tens of Oe) [22] and the relatively high currents needed to generate them. Replacing magnetic field pumping by electric field (VCMA) pumping solves this problem and allows parametric excitation of magnetic oscillations in metallic ferromagnets by a low-power microwave drive.

Chapter 3

Parametric Resonance Excited by Electric Field

Here I show that magnetic oscillations in a nanoscale magnetic tunnel junction can be generated via electric field induced parametric resonance. In the experiment, microwave electric field at twice the ferromagnetic resonance frequency modulates perpendicular magnetic anisotropy of the MTJ free layer and thereby parametrically excites oscillations of its magnetization.

3.1 Device and DC Characterization

The devices under study are elliptical nanoscale magnetic tunnel junctions with lateral dimensions 70 nm×150 nm, schematically shown in Fig. 3.1. The junctions are patterned from (bottom lead)/ Ta(5)/ PtMn(15)/ SAF/ MgO(0.83)/ $Co_{20}Fe_{60}B_{20}$(1.58)/ Ta(5)/ (cap) multilayers (thicknesses in nm) deposited by magnetron sputtering. Here SAF = $Co_{70}Fe_{30}$(2.3)/ Ru(0.85)/ $Co_{40}Fe_{40}B_{20}$(2.4) is the pinned synthetic antiferromagnet, which has magnetic

moments lying in the plane of the sample. The equilibrium direction of the $Co_{20}Fe_{60}B_{20}$ free layer magnetization is normal to the sample plane due to interfacial PMA [16]. Prior to patterning, the multilayers are annealed for 2 hours at 300 °C in a 10 kOe in-plane magnetic field that sets the pinned layer exchange bias direction parallel to the MTJ long axis.

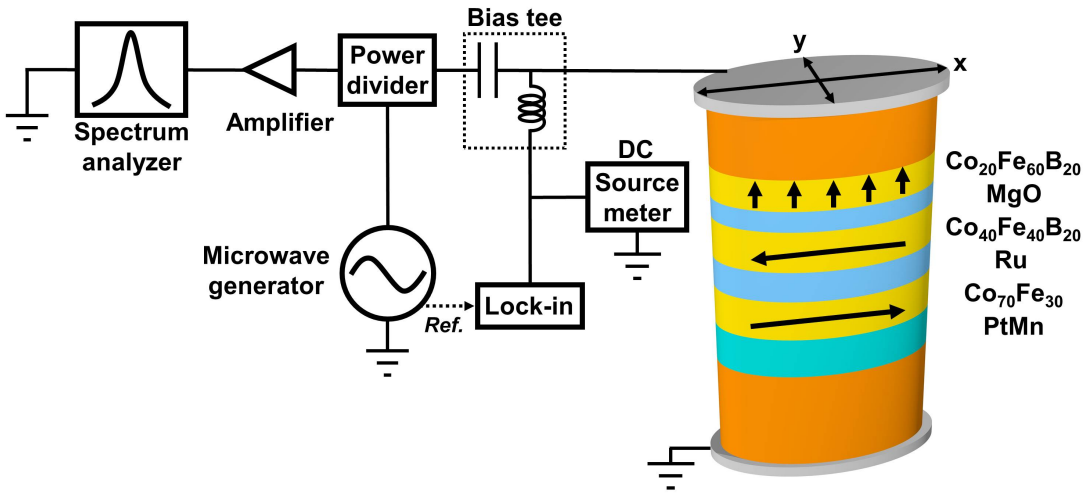

Figure 3.1: **Measurement setup for electrical characterization.** Schematic of the measurement setup. Reprinted with permission from Nano Lett., 2017, 17 (1), pp 572-577. Copyright 2017 American Chemical Society.

All measurements were made in the setup schematically shown in Fig. 3.1. The setup has a microwave generator, a spectrum analyzer, a microwave amplifier, and a DC sourcemeter connected through a bias tee and power divider. The circuit is connected to the sample by a microwave probe. This setup allows application of DC and microwave voltages to the MTJ, and it also allows measurement of DC and microwave signals generated by the MTJ.

First, a DC measurement is made to characterize the device resistance, which will be important for figuring out the magnetic state and calculating the amplitude of microwave drive. Fig. 3.2 shows conductance G of the MTJ measured as a function of in-plane magnetic field H_x applied parallel to the MTJ long axis. The shape of the $G(H_x)$ curve is congruent to the shape of the $M_x(H_x)$ hysteresis loop [16], where M_x is the normalized projection of the free layer magnetization onto the applied field direction. The hysteresis loop confirms the

out-of-plane easy axis of the free layer. The center of the loop is shifted from zero field due to a residual 0.06 kOe stray field from the SAF.

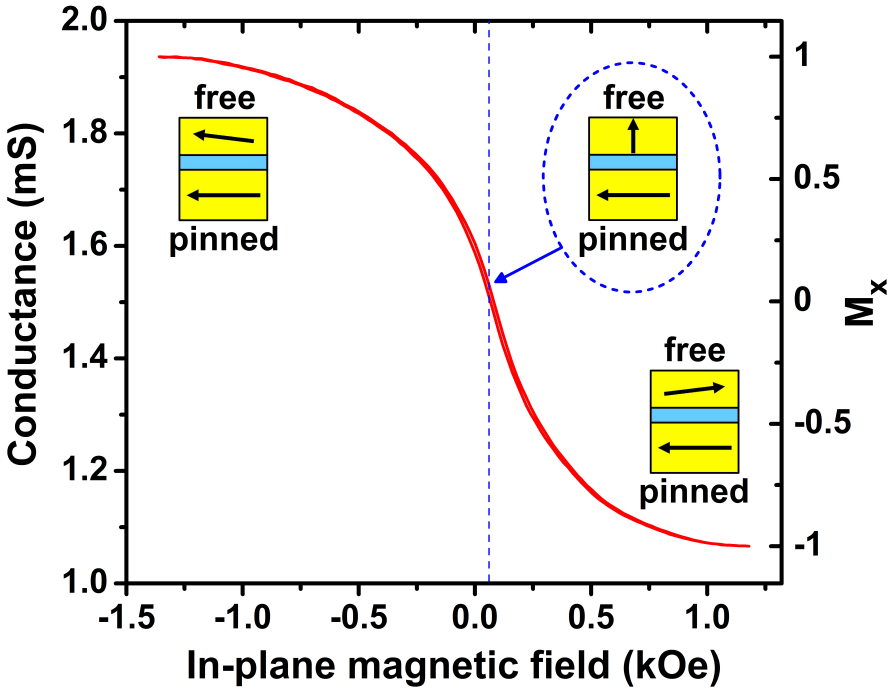

Figure 3.2: **MTJ conductance and magnetic configuration.** MTJ conductance as a function of in-plane magnetic field H_x applied parallel to the MTJ long axis. The diagrams indicate the magnetic configuration at different parts of the conductance curve. Reprinted with permission from Nano Lett., 2017, 17 (1), pp 572-577. Copyright 2017 American Chemical Society.

3.2 Spin Torque Ferromagnetic Resonance

Prior to performing microwave measurements, the circuit without the sample was calibrated so the microwave generator would source flat power as a function of excitation frequency. Since the parametric excitation amplitude is a function of microwave drive frequency and amplitude, this calibration is key to ensuring consistent measurement of the threshold required for parametric resonance. The calibration was done by placing a power meter in place of the sample location and sourcing microwave signal from the generator while the amplifier

was powered on. Power flatness was calibrated to within less than 0.1 dB of the setpoint power, as delivered to a 50 Ω load. Impedance mismatch between the microwave equipment and the MTJ will change the microwave current and voltage at the sample, which is taken into account through characterization of the MTJ resistance as mentioned above. In principle, imaginary parts of the impedance could come into play through parasitic capacitances or inductances, but this was not taken into account in this experiment and is thus assumed to be negligible. [7]

We employ spin torque ferromagnetic resonance to characterize the spectral properties of the spin wave eigenmodes of the MTJ. I will briefly review the technique and introduce notation that is used later in describing the parametric resonance signal. As mentioned previously, a small amplitude microwave drive current $GV_{\mathrm{ac}} \sin(2\pi f_{\mathrm{d}} t)$ is applied to the MTJ and excites oscillations of magnetization at the drive frequency f_{d}. Here, G is the device conductance, V_{ac} is the amplitude of the microwave voltage, and f_{d} is the drive frequency. The resulting resistance oscillations $R_{\mathrm{ac}} \sin(2\pi f_{\mathrm{d}} t + \phi)$ of the MTJ at the drive frequency lead to partial rectification of the microwave drive voltage V_{ac} and generate a direct voltage V_{r}. Here, R_{ac} is the amplitude of the ac resistance oscillations and ϕ is the phase difference between resistance oscillations and microwave drive, which can be different from zero. Peaks (or dips) in ST-FMR spectra $V_{\mathrm{r}}(f_{\mathrm{d}})$ arise from resonant excitation of spin wave eigenmodes of the MTJ [31, 32].

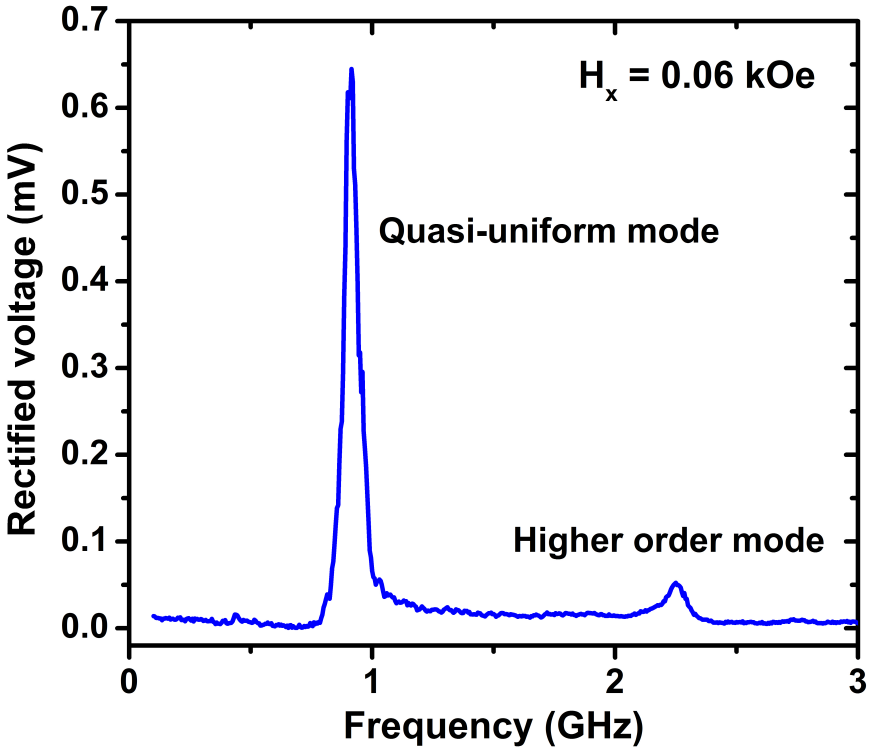

Figure 3.3: **ST-FMR spectrum.** ST-FMR spectrum measured at $H_x = 0.06$ kOe. Reprinted with permission from Nano Lett., 2017, 17 (1), pp 572-577. Copyright 2017 American Chemical Society.

Fig. 3.3 shows an ST-FMR spectrum of the MTJ measured at $H_x = 0.06$ kOe. Two spin wave eigenmodes are present in this spectrum with the lowest-frequency ($f_0 = 0.91$ GHz) mode being the quasi-uniform mode of the free layer [35]. From the spectral linewidth of the quasi-uniform mode we can estimate the Gilbert damping parameter to be $\alpha \sim 0.0384$, which is typical for a CoFeB layer of this thickness [16]. Dependence of ST-FMR spectra on H_x is summarized in Fig. 3.4. The frequency of the quasi-uniform mode increases with increasing absolute value of the net in-plane field due to the second order uniaxial PMA present in this system [16].

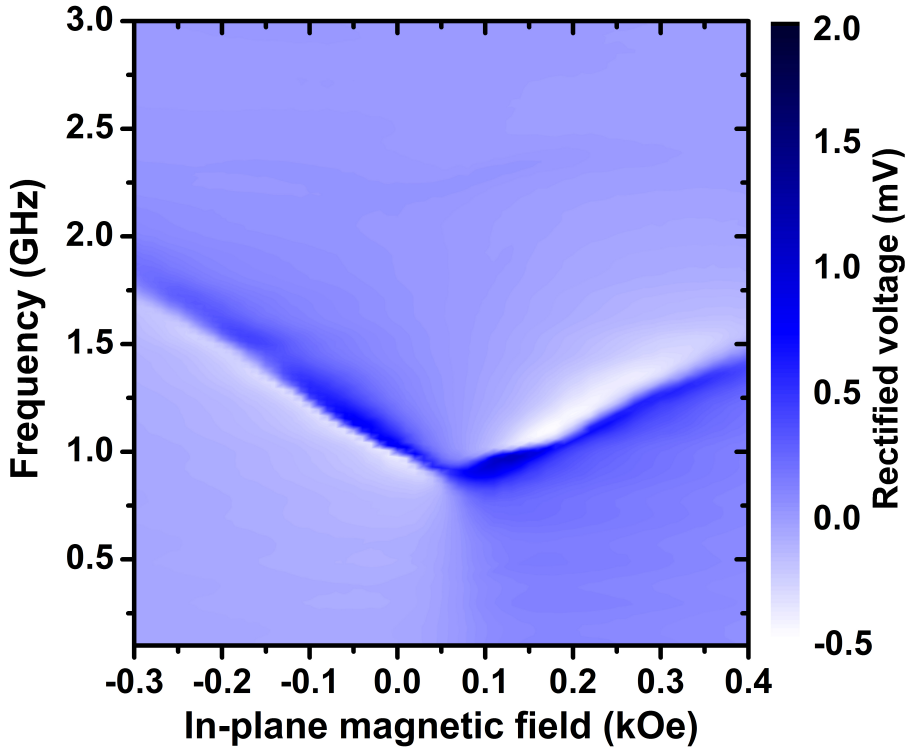

Figure 3.4: **ST-FMR f(H) contour plot.** Dependence of ST-FMR spectra on H_{x}. Reprinted with permission from Nano Lett., 2017, 17 (1), pp 572-577. Copyright 2017 American Chemical Society.

Fig. 3.5 shows dependence of the quasi-uniform mode frequency on direct voltage bias V_{dc} applied to the MTJ. The observed linear frequency shift arises exclusively from VCMA because Ohmic heating, damping-like ST, and field-like ST are all expected to induce quadratic frequency shifts in V_{dc} for the perpendicular orientation of the SAF and free MTJ layers employed in this experiment. The slope of the line in Fig. 3.5 is approximately equal to $(\gamma/2\pi)(\mathrm{d}H_{\mathrm{u}}/\mathrm{d}V_{\mathrm{dc}})$, where the gyromagnetic ratio γ is taken to be 176 GHz/T and H_{u} is the PMA effective field. The data in Fig. 3.5 gives VCMA efficiency $\mathrm{d}H_{\mathrm{u}}/\mathrm{d}V_{\mathrm{dc}} = 526$ Oe/V, which is typical for this material system [16].

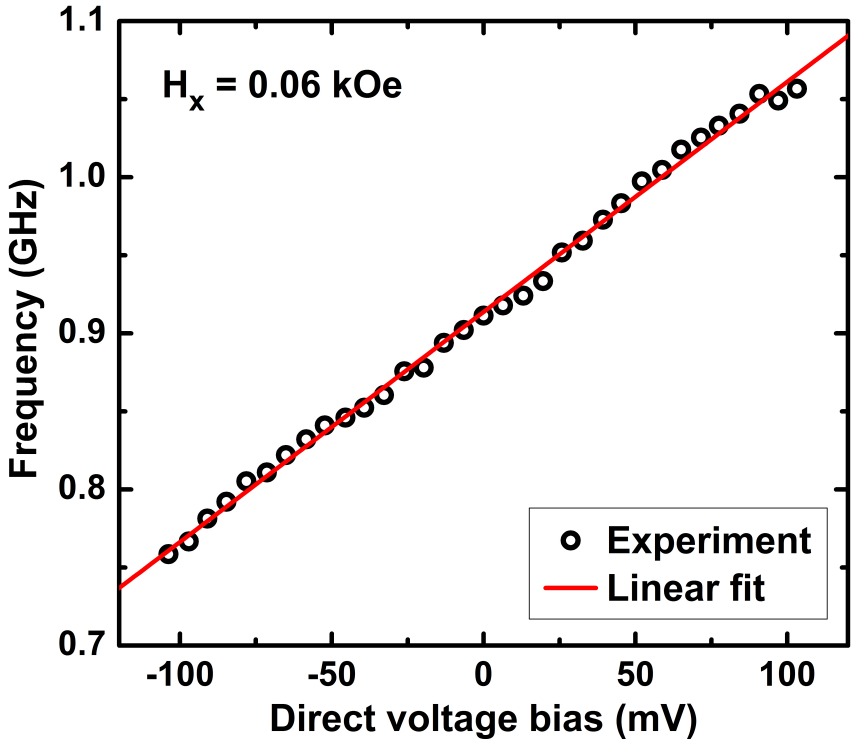

Figure 3.5: **Quasi-uniform mode frequency vs. voltage.** Quasi-uniform mode frequency versus direct voltage bias V_{dc} measured at $H_{\mathrm{x}} = 0.06$ kOe. Reprinted with permission from Nano Lett., 2017, 17 (1), pp 572-577. Copyright 2017 American Chemical Society.

3.3 Microwave Emission Measurements

After we have characterized the possible excitation modes via ST-FMR, we can attempt to excite these modes parametrically (through vCMA) rather than by direct excitation (through ST). We use the so-called parallel pumping geometry to parametrically excite the free layer quasi-uniform mode [17]. In this geometry, magnetization of the free layer is parallel to the oscillating PMA effective field H_{u}. We apply a constant 0.06 kOe in-plane magnetic field along the long axis of the ellipse to compensate the in-plane SAF stray field acting on the free layer. We then apply a parametric drive voltage V_{ac} to the MTJ at drive frequency f_{d} near $2f_0$ (twice the resonance frequency of the quasi-uniform mode). The microwave

voltage results in modulation of PMA at the drive frequency, f_{d}, due to VCMA. This can parametrically excite magnetization oscillations at half the drive frequency, $f_{\mathrm{d}}/2$, [17] which gives rise to the MTJ resistance oscillations

$$R_{\mathrm{ac}} \cos(2\pi \frac{f_{\mathrm{d}}}{2} t + \phi). \tag{3.1}$$

These resistance oscillations can be detected via their mixing with the microwave current

$$G V_{\mathrm{ac}} \cos(2\pi f_{\mathrm{d}} t) \tag{3.2}$$

through the junction, which generates voltage signals proportional to R_{ac} at frequencies $f_{\mathrm{d}}/2$ and $3f_{\mathrm{d}}/2$:

$$\begin{aligned} V_{\mathrm{mix}}(t) &= G V_{\mathrm{ac}} \cos(2\pi f_{\mathrm{d}} t) \cdot R_{\mathrm{ac}} \cos\left(2\pi \frac{f_{\mathrm{d}}}{2} t + \phi\right) \\ &= \frac{1}{2} G V_{\mathrm{ac}} R_{\mathrm{ac}} \left[\cos\left(2\pi \frac{f_{\mathrm{d}}}{2} t - \phi\right) + \cos\left(2\pi \frac{3 f_{\mathrm{d}}}{2} t + \phi\right) \right]. \end{aligned} \tag{3.3}$$

Therefore, in order to detect the parametric resonance, we tune the spectrum analyzer to a window around the ferromagnetic resonance frequency f_0. As we sweep through the microwave drive frequencies near twice the resonance frequency $2f_0$, we should detect emissions on the spectrum analyzer if we do indeed excite parametric resonance.

As illustrated in Fig. 3.1, we amplify $V_{\mathrm{mix}}(t)$ and measure its spectrum with a microwave spectrum analyzer. We used a $+22\,\mathrm{dB}$ gain amplifier which operates in the frequency range $0.1\,\mathrm{GHz}$ to $1.5\,\mathrm{GHz}$, and this gain was accounted for in the later analysis of microwave drive amplitude.

3.4 Experimental Results

In this section, I present power spectra of $V_{\rm mix}(t)$ measured by the spectrum analyzer near $f_{\rm d}/2$. Similar spectra are observed near $3f_{\rm d}/2$. Fig. 3.6 displays power spectral density (PSD) $P(f)$ of $V_{\rm mix}(t)$ measured at several fixed values of the drive frequency $f_{\rm d}$ near $2f_0$ and drive amplitude $V_{\rm ac} = 0.185$ V. The maximum of each power spectrum is observed exactly at $f_{\rm d}/2$, clearly illustrating that magnetization dynamics of the free layer is excited parametrically at half the drive frequency. The linewidths of the measured spectral peaks are in the range of several MHz. This linewidth mostly arises from thermal fluctuations of the free layer magnetization (fluctuations of the phase ϕ and amplitude $R_{\rm ac}$ in equation (3.3)). Fig. 3.7 illustrates that parametric excitation of the quasi-uniform mode has well-pronounced resonant character: significant amplitude of the parametric oscillations is observed only in a narrow range of the drive frequencies near $2f_0$.

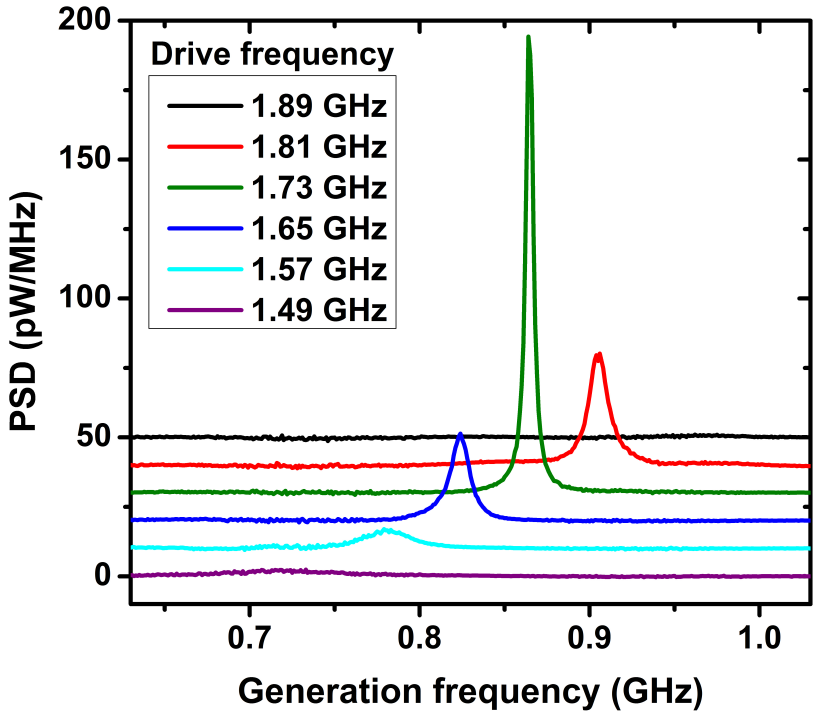

Figure 3.6: **Power spectral density of parametric resonance signal.** Power spectral density (PSD) of the microwave signal emitted by the MTJ under VCMA parametric drive of $V_{ac} = 0.185$ V. Curves are vertically offset for clarity. Reprinted with permission from Nano Lett., 2017, 17 (1), pp 572-577. Copyright 2017 American Chemical Society.

Fig. 3.8 displays dependence of $P(f_d/2)$ on the drive amplitude V_{ac} and drive frequency f_d. This figure illustrates the parametric excitation efficiency and clearly demonstrates that the observed microwave emission from the sample shows a threshold character in V_{ac}. This threshold behavior is expected for parametric resonance that is excited when effective negative damping from the parametric drive exceeds the positive natural damping of the excited mode [4, 5]. Fig. 3.8 also shows that the parametric resonance frequency f_{pr} (defined as the drive frequency f_d that gives maximum power $P(f_d/2)$ at a given value of microwave drive V_{ac}) shifts to lower values with increasing drive amplitude, as expected for a uniaxial ferromagnet [12]. The shape of the parametric instability region in Fig. 3.8 is a typical Arnold tongue of a nonlinear parametric oscillator [34].

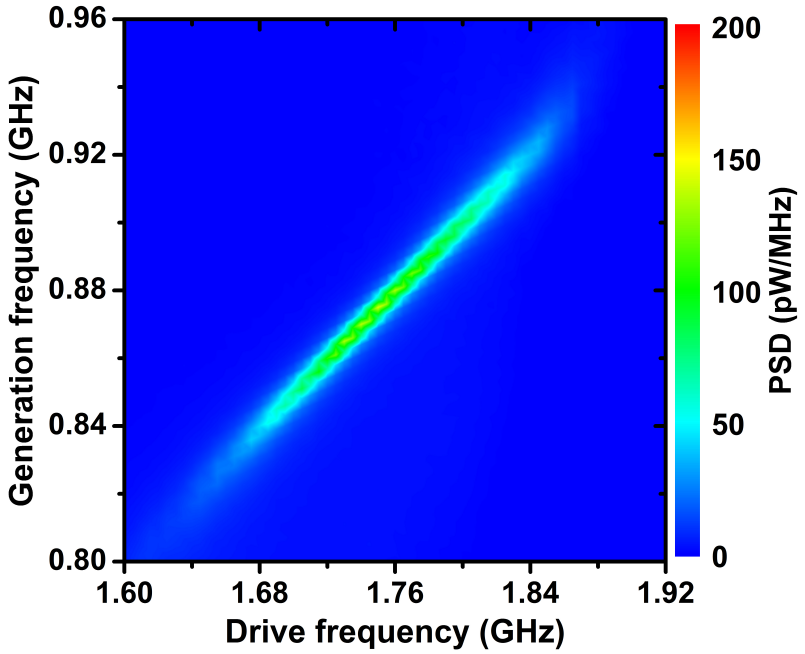

Figure 3.7: **Power spectral density contour plot.** Dependence of the parametrically generated emission spectra on the drive frequency. Reprinted with permission from Nano Lett., 2017, 17 (1), pp 572-577. Copyright 2017 American Chemical Society.

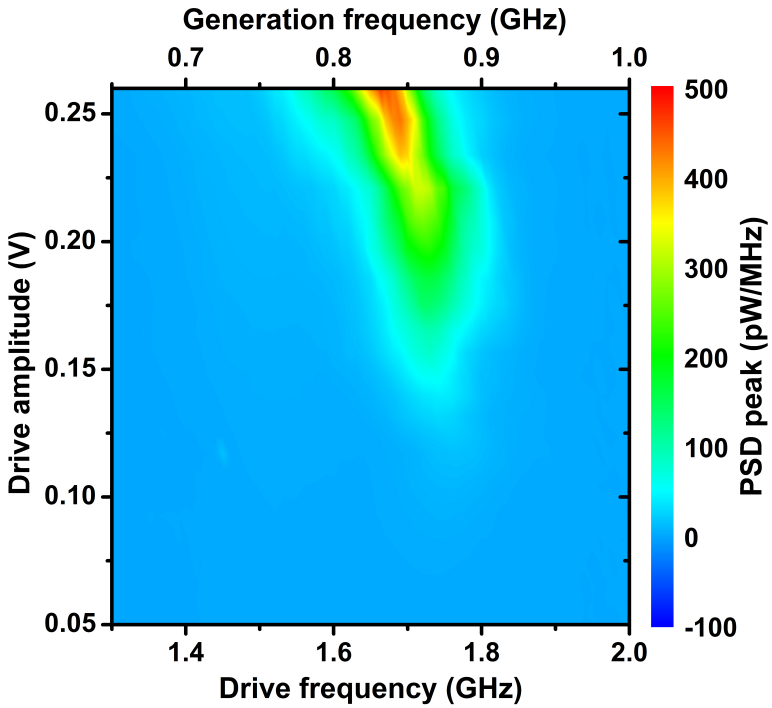

Figure 3.8: **PSD contour vs. frequency and drive amplitude.** PSD peak plotted versus drive frequency and drive amplitude reveals typical Arnold tongue shape characteristic of parametric excitation. Reprinted with permission from Nano Lett., 2017, 17 (1), pp 572-577. Copyright 2017 American Chemical Society.

3.4.1 Experimental Determination of the Threshold

In experiment, the exact position of the excitation threshold could be determined by fitting the dependence of oscillation power on microwave drive amplitude.

Data Analysis

In order to quantitatively determine the experimental value of the threshold drive voltage V_{th} needed to excite parametric resonance of the quasi-uniform mode, we analyze reduced power of this mode p as a function of the drive amplitude V_{ac}. By definition, $p = |c|^2$ where c is the dimensionless amplitude of the quasi-uniform mode as described previously. c is

proportional to the amplitude of the MTJ resistance oscillations, so that $p \sim (GR_{\rm ac})^2$. It is clear from equation (3.3) that PSD of the reduced power $p(f)$ is proportional to $P(f)/V_{\rm ac}^2$ for any $V_{\rm ac}$. In Fig. 3.9a, we plot its resonant value $P(f_{\rm pr}/2)/V_{\rm ac}^2$, which is proportional to $p(f_{\rm pr}/2)$, as a function of $V_{\rm ac}$.

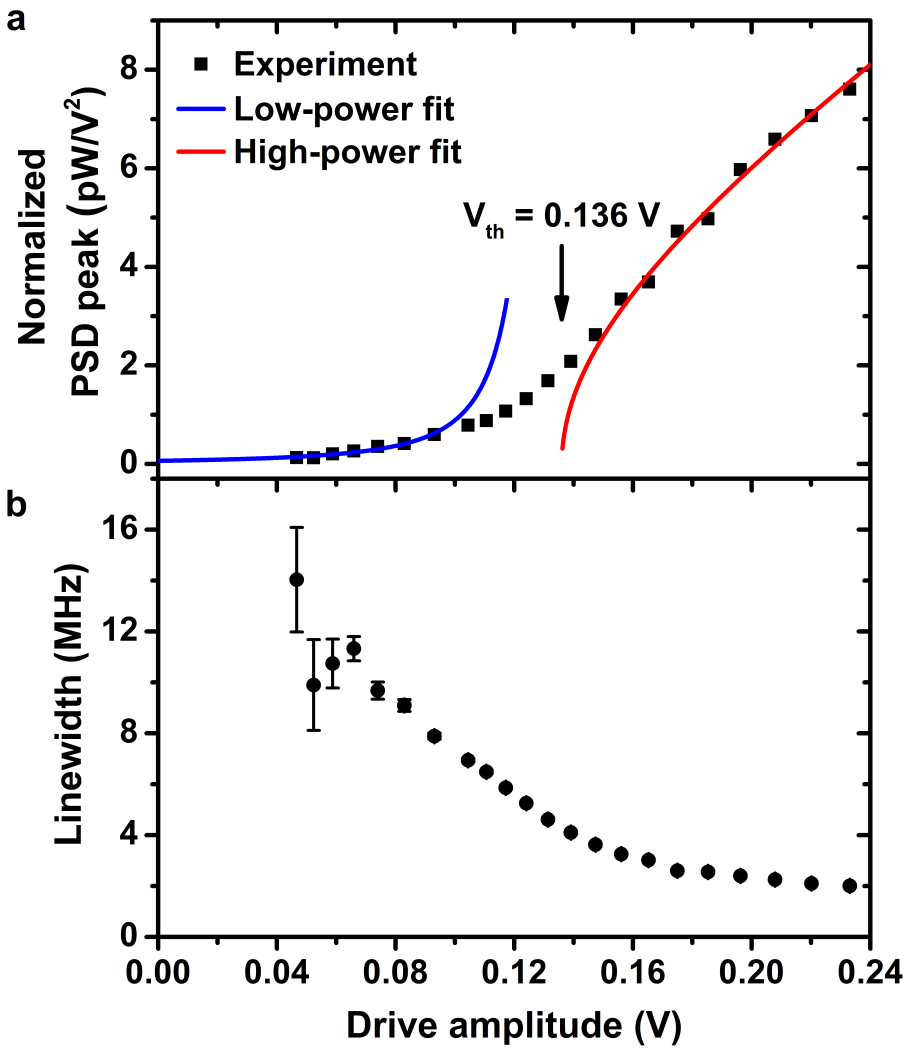

Figure 3.9: **Parametric resonance threshold.** **a**, Normalized PSD peak amplitude $P(f_{\rm pr}/2)/V_{\rm ac}^2$ measured at parametric resonance as a function of the parametric drive amplitude $V_{\rm ac}$. Best fits of equation (3.4) and equation (3.5) to the data (solid lines) give the parametric resonance threshold voltage $V_{\rm th} = 0.136$ V. **b**, Dependence of the PSD spectral linewidth (half width at half maximum) on the parametric drive amplitude $V_{\rm ac}$ measured at parametric resonance.

Analytic expressions for $p(f_{\mathrm{pr}}/2)$ have been derived in the limit of $V_{\mathrm{ac}} \ll V_{\mathrm{th}}$. In this limit, magnetization dynamics are small-amplitude thermal fluctuations amplified by the parametric drive:

$$p(f_{\mathrm{pr}}/2) = \frac{C_1}{(V_{\mathrm{th}} - V_{\mathrm{ac}})^2}. \tag{3.4}$$

In the opposite limit of $V_{\mathrm{ac}} \gg V_{\mathrm{th}}$, thermal fluctuations can be neglected and the following analytic expression for the reduced power p can be derived:

$$p = C_2\sqrt{V_{\mathrm{ac}}^2 - V_{\mathrm{th}}^2}. \tag{3.5}$$

For our system, p in equation (3.5) can be replaced by $p(f_{\mathrm{pr}}/2)$ because the measured spectral linewidth of $P(f)$ at $f_{\mathrm{d}} = f_{\mathrm{pr}}$ shown in Fig. 3.9b depends weakly on V_{ac} for $V_{\mathrm{ac}} > 0.16$ V. Therefore, we can fit the data in Fig. 3.9a using equation (3.4) in the small amplitude limit and equation (3.5) in the large amplitude limit. The best fit to the data in the $V_{\mathrm{ac}} \ll V_{\mathrm{th}}$ ($V_{\mathrm{ac}} \gg V_{\mathrm{th}}$) limit shown by the blue (red) line in Fig. 3.9a gives $V_{\mathrm{th}} = 0.136$ V. In this fitting procedure, C_1 and C_2 are free fitting parameters while V_{th} is treated as a common fitting parameter for both the small and large amplitude limits. (See the next section on fitting.)

It is instructive to compare the measured V_{th} to its theoretically expected value, which was calculated for the MTJ geometry and the measured VCMA efficiency. The calculated threshold voltage for the case of a uniform mode was $V_{\mathrm{th}} = 0.085\,\mathrm{V}$ while using a non-uniform mode profile from simulations yielded $V_{\mathrm{th}} = 0.156\,\mathrm{V}$. The experimental value is between these two values, which lends support to the VCMA origin of the observed parametric resonance. This indicates the experimentally excited mode is not entirely uniform, and the mode profile found in simulation might not match the one in experiment. We could reasonably attribute

the discrepancy to deviation of the sample shape from the ideal elliptical cylinder shape, which would have a large impact on the ellipticity of the excited mode.

In our experiment, spin-polarized tunneling current flows through the MTJ, which results in ST and Oersted field acting on the free layer. However, these types of drive play a negligible role in exciting parametric resonance compared to the VCMA drive. The Oersted field has nearly circular symmetry and therefore it poorly couples to the quasi-uniform mode. The field-like ST was shown to be small compared to the damping-like ST in previous studies of these samples [16]. The effective field of the damping-like ST lies in the sample plane, which corresponds to perpendicular pumping geometry. It is known that parametric excitation of the quasi-uniform mode is not possible in this geometry.

3.5 Parametric Resonance Detected by ST-FMR

Our experiment employs an MTJ magnetic configuration with in-plane SAF and out-of-plane free layer. It is convenient for unambiguous demonstration and quantitative analysis of parametric resonance excited by VCMA. However, we find that VCMA-driven parametric resonance is ubiquitous and can be observed in other types of MTJ configurations as well. Fig. 3.10 shows the out-of-plane magnetic field dependence of ST-FMR spectra measured for a 30 nm$\times$95 nm MTJ with out-of-plane equilibrium configuration of both the free and SAF layers. Because of the smaller amplitude of the ST-FMR rectified voltage in this collinear geometry, we employed ultra-sensitive ST-FMR with magnetic field modulation [35] rather than conventional ST-FMR with amplitude modulation.

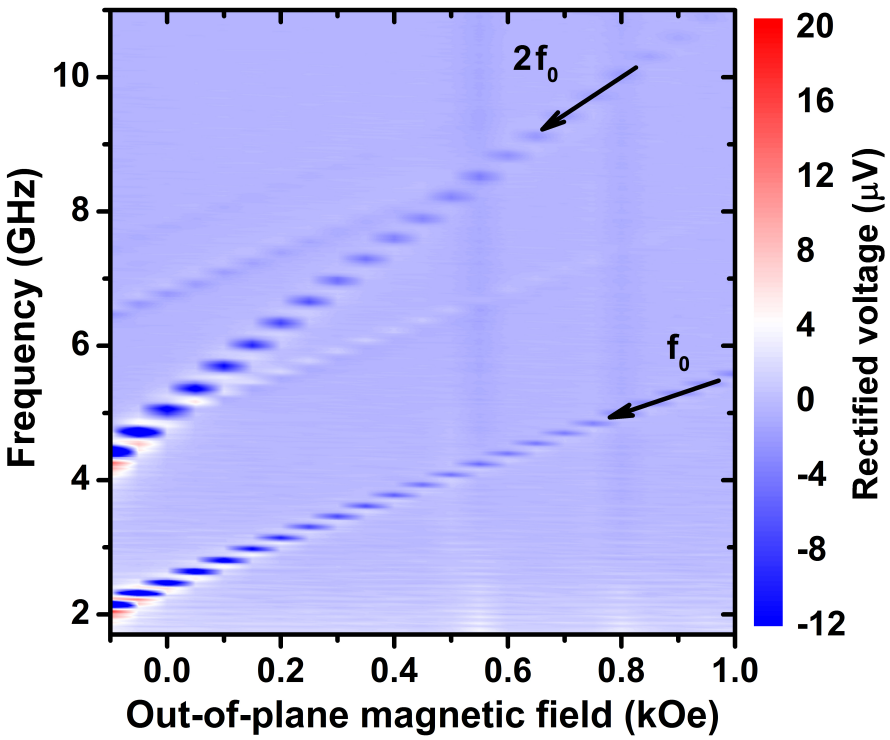

Figure 3.10: **Parametric resonance in ST-FMR.** ST-FMR spectra of an MTJ with out-of-plane SAF and free layers measured as a function of out-of-plane magnetic field. Resonance at twice the quasi-uniform mode frequency arises from parametric excitation of the quasi-uniform mode. Reprinted with permission from Nano Lett., 2017, 17 (1), pp 572-577. Copyright 2017 American Chemical Society.

The ST-FMR spectra measured at a large value of the microwave drive voltage $V_{\rm ac} = 0.396$ V reveal several spin wave eigenmodes of the free layer. Another prominent resonance is observed at twice the frequency of the lowest-frequency (quasi-uniform) spin wave eigenmode. In this collinear MTJ geometry, the microwave resistance oscillations of the device have a significant component at twice the excited spin wave mode frequency and mix with the parametric drive at twice the mode frequency to give rise to a rectified voltage peak at $2f_0$ measured by ST-FMR. The amplitude of this additional resonance at $2f_0$ relative to the amplitude of the resonance at f_0 increases with increasing $V_{\rm ac}$, which is a signature of a thermally smeared threshold behavior similar to that in Fig. 3.9a. The out-of-plane collinear geometry is commonly employed in spin transfer torque magnetic random access memory

(STT-MRAM), and parametric resonance signals in ST-FMR of STT-MRAM can potentially be used for characterization of the free layer properties such as magnetic damping.

3.6 Micromagnetic Simulations

To determine the magnetic ground state of the MTJ nanopillar studied in this work, we performed micromagnetic simulations of the entire nanopillar stack (including the free and the SAF layers) using OOMMF software [40]. The magnetic material parameters of the free and the SAF layers employed in the simulations were determined in previous studies of these MTJ devices [16, 35].

We simulate the hysteresis loops of the device at zero temperature as a function of in-plane magnetic field H_{x}. Figure 3.11a shows the major loop of the normalized free layer magnetization M_{x} as a function of H_{x} (the SAF layer magnetization does not switch for the range of H_{x} employed). This loop is shifted from zero field by a value similar to that observed in the experiment (see Fig. 1b of the main text) due to stray magnetic field from the SAF layer acting on the free layer.

The simulations reveal the presence of three stable states of the free layer magnetization at low fields as illustrated in Fig. 3.11c: two Néel domain wall states with opposite directions of magnetization in the middle of the domain wall (1 and 2) and the quasi-uniform state (3). A minor hysteresis loop shown in Fig. 3.11b demonstrates that the quasi-uniform state of the free layer is stable in a wide range of magnetic fields near zero, suggesting that this state is the ground state near zero field. This is directly confirmed by plotting the total micromagnetic energy of the MTJ as a function of H_{x} for all three micromagnetic states of the system (Fig. 3.11d). This plot clearly shows that the quasi-uniform state of the free layer magnetization is the lowest energy state in a significant range of fields near zero. The

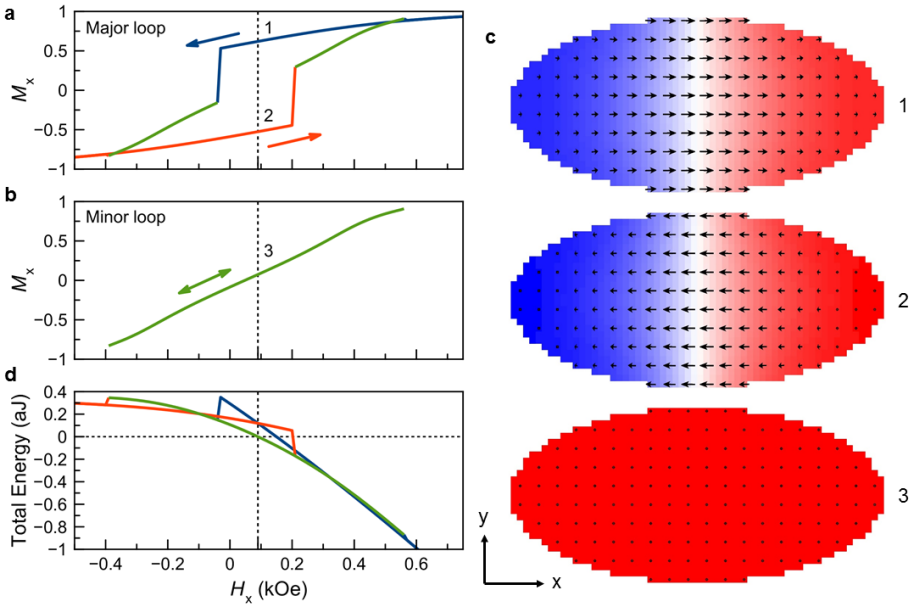

Figure 3.11: **Micromagnetic simulations.** **a**,**b**, Normalized magnetization of the free layer M_x as a function of in-plane magnetic field H_x applied parallel to the MTJ long axis, given by zero-temperature micromagnetic simulations (**a** - major loop of the free layer, **b** - minor loop of the free layer). Arrows indicate field sweep direction. **c**, Three stable micromagnetic states of the free layer in the middle of the hysteresis loop: two Néel domain wall states with opposite directions of magnetization in the middle of the domain wall (1 and 2) and the quasi-uniform state (3). Arrows show the in-plane magnetization component while the colors represent the out-of-plane magnetization component with red (blue) being positive (negative). **d**, Total micromagnetic energy of the MTJ as a function of H_x. Colors correspond to the free layer micromagnetic states shown in **a**, **b**, and **c**. Reprinted with permission from Nano Lett., 2017, 17 (1), pp 572-577. Copyright 2017 American Chemical Society.

asymmetry of the total energy in H_x is due to a non-zero net magnetic moment of the SAF layer.

Micromagnetic simulations of the hysteresis loop at room temperature ($T \approx 300\,\mathrm{K}$) and magnetic field sweep rate employed in our experiment are prohibitively time consuming. However, given the importance of thermal fluctuations for a free layer nanomagnet of the small size and low magnetic anisotropy employed in our measurements, we can expect the free layer is in its lowest energy state for magnetic field values near zero. This assumption is supported by the absence of hysteresis in the experimentally measured $M_x(H_x)$ curve shown in Fig. 1b of the main text. Furthermore, the data in Fig. 1d show that the Boltzmann

probability of the quasi-uniform state is much greater than that of the domain wall state in the middle of the hysteresis curve. For any two states, the Boltzmann ratio of probabilities of being in those states is:

$$\frac{p_i}{p_j} = \exp\left[-(E_i - E_j)/k_{\mathrm{B}}T\right], \tag{3.6}$$

where p_i and p_j are the probabilities of being in state i and state j, E_i and E_j are the total micromagnetic energies of the states, k_{B} is the Boltzmann constant, and T is the temperature. The energy difference between the domain wall state and the quasi-uniform state in the middle of the hysteresis loop is 1.19×10^{-19} J, with the quasi-uniform state being lower in energy as shown in Fig. 1d. Therefore, the Boltzmann probability of the domain wall state is 3.5×10^{-13} of that of the quasi-uniform state at $T = 300$ K.

3.7 Gilbert damping

The Gilbert damping of the free layer was estimated from the spectral linewidth of the quasi-uniform mode measured by ST-FMR technique at $H_{\mathrm{x}} = 0.06$ kOe. Assuming uniaxial anisotropy, the Gilbert damping parameter is given by the ratio of half width at half maximum Δf of the ST-FMR resonance curve $V_{\mathrm{r}}(f_{\mathrm{d}})$ to the quasi-uniform mode resonance frequency f_{SW} [4]:

$$\alpha = \frac{\Delta f}{f_{\mathrm{SW}}}. \tag{3.7}$$

In the experiment (see Fig. 1c of the main text), we find $\Delta f \approx 0.03$ GHz. By using this value of the linewidth and the measured resonance frequency $f_{\mathrm{SW}} = 0.91$ GHz, we obtain an estimate of the free layer Gilbert damping constant $\alpha \approx 0.033$.

3.8 VCMA efficiency

The observed linear shift of the quasi-uniform mode resonance frequency f_{SW} with applied direct voltage V_{dc} shown in Fig. 1e of the main text arises exclusively from VCMA. The effective fields due to field-like and damping-like spin torque are perpendicular to the free layer magnetization for the perpendicular orientation of the free and the SAF magnetic moments employed in our experiment. Such perpendicular fields can only induce a quadratic shift of the quasi-uniform mode frequency. The frequency shift due to Ohmic heating is independent of the current polarity and thus is also quadratic in V_{dc} to leading order. Given the linear relation between the resonance frequency f_{SW} and the anisotropy field H_{u} for a uniaxial ferromagnet, the slope of the line in Fig. 1e in the main text is

$$\frac{\gamma}{2\pi}\frac{dH_{\mathrm{u}}}{dV_{\mathrm{dc}}}, \tag{3.8}$$

where the gyromagnetic ratio γ is taken to be 176 GHz/T. The data in Fig. 1e in the main text gives VCMA efficiency $\frac{dH_{\mathrm{u}}}{dV_{\mathrm{dc}}} = 526\,\mathrm{Oe/V}$, which is typical for this material system [16].

3.9 Theory of parametric resonance threshold

For the theoretical description of parametric resonance of the MTJ free layer we employ a single-mode approximation. We expand the free layer magnetization into static and dynamic parts: $\mathbf{M}(\mathbf{r},t) = M_{\mathrm{s}}(\boldsymbol{\mu} + c(t)\mathbf{m}(\mathbf{r}) + c^*(t)\mathbf{m}^*(\mathbf{r}))$, where $\boldsymbol{\mu}$ is the unit vector in the direction of the static magnetization, $\mathbf{m}(\mathbf{r})$ is the coordinate-dependent vector structure of the spin wave mode, and c is the dimensionless amplitude of this mode. Starting from the Landau-Lifshitz-Gilbert equation, the following nonlinear equation describing the dynamics can be derived [4, 17]:

$$\frac{\mathrm{d}c}{\mathrm{d}t} + i(\omega_{\mathrm{SW}} + \Psi|c|^2)c + \Gamma c = hV_{00}e^{i\omega_{\mathrm{P}}t}c^* + \eta(t), \tag{3.9}$$

where $\omega_{\rm SW} = 2\pi f_{\rm SW}$ is the spin wave mode angular frequency, Ψ is the nonlinear frequency shift of the mode, Γ is the damping rate of the mode, h is the effective pumping field amplitude, $\omega_{\rm p}$ is the pumping frequency, V_{00} is the efficiency of parametric interaction, and $\eta(t)$ describes thermal noise (see Ref. [38] for details). In these notations, the parametric resonance threshold field is $h_{\rm th} = \Gamma/|V_{00}|$, where $|V_{00}| = \frac{\gamma\mu_0}{2}\varepsilon$, γ is the gyromagnetic ratio taken to be 176 GHz/T, $\mu_0 = 4\pi \times 10^{-7}$ T·m/A is the permeability of vacuum, and the damping rate $\Gamma = 2\pi\Delta f = 2\pi \times 0.03$ GHz [4, 17]. Averaged ellipticity of the spin wave mode ε is given by [17]:

$$\varepsilon = \left| \frac{\langle \mathbf{m}^* \cdot \mathbf{m}^* \rangle_{\mathbf{r}}}{\langle \mathbf{m}^* \cdot (\boldsymbol{\mu} \times \mathbf{m}) \rangle_{\mathbf{r}}} \right|, \tag{3.10}$$

where $\langle ... \rangle_{\mathbf{r}}$ denotes a spatial average over the free layer volume.

We calculate the quasi-uniform mode ellipticity from the micromagnetic mode profile. This calculation gives $\varepsilon = 0.26$, which results in $h_{\rm th} = 6.5$ kA/m = 82 Oe. This gives the threshold voltage for excitation of parametric resonance $V_{\rm th} = h_{\rm th}\frac{dV_{\rm dc}}{dH_{\rm u}} = 0.156$ V. This micromagnetic value of $V_{\rm th}$ is significantly higher than that given by the macrospin approximation with $\varepsilon = \omega_{\rm M}|N_{\rm x} - N_{\rm y}|/(2\omega_{\rm SW})$, where $\omega_{\rm M} = \gamma\mu_0 M_{\rm s}$ (with $M_{\rm s} = 950$ kA/m), $N_{\rm x} = 0.014$ and $N_{\rm y} = 0.040$ are components of the free layer demagnetization tensor [39], and $\omega_{\rm SW} = 2\pi \times 0.91$ GHz is the spin wave mode frequency. The higher value of ellipticity ($\varepsilon = 0.478$) in the macrospin approximation leads to a lower parametric threshold: $h_{\rm th} = 45$ Oe and $V_{\rm th} = 0.085$ V. As expected, the experimentally measured value of the threshold voltage $V_{\rm th} = 0.136$ V is much higher than that given by the macrospin approximation but it is similar to that appropriate for micromagnetic profile of the quasi-uniform mode. The 15% discrepancy between the measured and the theoretically predicted threshold could arise from deviation of the free layer shape from the ideal elliptical shape assumed in the simulations and from over-estimation of the damping parameter of the free layer.

3.10 Evaluation of the parametric resonance threshold from experiment

To determine the threshold voltage for parametric excitation $V_{\rm th}$ from the experimental data in Fig. 3 of the main text, we fit these data to theoretical expressions of the oscillation power as a function of the drive amplitude $V_{\rm ac}$. These expressions are derived below for two limits: $V_{\rm ac} \ll V_{\rm th}$ and $V_{\rm ac} \gg V_{\rm th}$.

3.10.1 Below the threshold

Well below the threshold ($V_{\rm ac} \ll V_{\rm th}$), the nonlinear frequency shift in Eq. (3.9) can be neglected and the parametric resonance frequency $f_{\rm pr}$ is equal to twice the spin wave mode frequency ($f_{\rm pr} = 2f_{\rm SW}$). In this limit, the reduced integrated power p of the spin wave mode is given by the expression below when the free layer is driven exactly at the parametric resonance frequency $f_{\rm pr}$:

$$p = \left\langle |c|^2 \right\rangle = \frac{C_1}{\Gamma - |hV_{00}|} + \frac{C_1}{\Gamma + |hV_{00}|} = \frac{D}{(V_{\rm th} - V_{\rm ac})} + \frac{D}{(V_{\rm th} + V_{\rm ac})}, \tag{3.11}$$

where $\langle ... \rangle$ denotes a thermal average. In deriving this expression, we assumed white thermal noise: $\langle \eta(t)\eta(\tau) \rangle = C_2\delta(t-\tau)$ and $\langle \eta(t)\eta^*(\tau) \rangle = C_1\delta(t-\tau)$, where C_1, C_2 and $D = C_1 V_{\rm th}/\Gamma$ are constants. Here we also employed the linear relation between the effective (VCMA) pumping field amplitude h and the microwave voltage amplitude $V_{\rm ac}$, which is evident from Fig. 1e of the main text.

By expanding the noise term into Fourier series, we obtain the following expression for reduced power spectral density $p(f)$ of the spin wave mode oscillations:

$$p(f) = \left\langle |c(f)|^2 \right\rangle = \frac{C_2}{(\Gamma - |hV_{00}|)^2 + (2\pi(f - f_{\rm SW}))^2} + \frac{C_2}{(\Gamma + |hV_{00}|)^2 + (2\pi(f - f_{\rm SW}))^2} \quad (3.12)$$

$$= \frac{A}{(V_{\rm th} - V_{\rm ac})^2 + (2\pi(f - f_{\rm SW})V_{\rm th}/\Gamma)^2} + \frac{A}{(V_{\rm th} + V_{\rm ac})^2 + (2\pi(f - f_{\rm SW})V_{\rm th}/\Gamma)^2}, \quad (3.13)$$

where $A = C_2 V_{\rm th}^2/\Gamma^2$ is a constant. Setting $f = f_{\rm SW}$ in Eq. (3.13), we obtain an expression for the peak value of the reduced PSD that is observed at $f = f_{\rm SW} = f_{\rm pr}/2$:

$$p(f_{\rm pr}/2) = \left\langle |c(f_{\rm pr}/2)|^2 \right\rangle = \frac{A}{(V_{\rm th} - V_{\rm ac})^2} + \frac{A}{(V_{\rm th} + V_{\rm ac})^2}. \quad (3.14)$$

The second term in Eq. (3.14) is much smaller than the first one for $V_{\rm ac}$ approaching $V_{\rm th}$ and it can be neglected in fitting the experimental data of Fig. 3 of the main text:

$$p(f_{\rm pr}/2) = \left\langle |c(f_{\rm pr}/2)|^2 \right\rangle = \frac{A}{(V_{\rm th} - V_{\rm ac})^2}. \quad (3.15)$$

3.10.2 Above the threshold

Well above the threshold ($V_{\rm ac} \gg V_{\rm th}$), the integrated power of the parametrically excited quasi-uniform mode is nearly temperature independent and can be approximated by its zero-temperature value [**?**]. Neglecting the thermal noise term in Eq. (3.9), we derive:

$$p = |c|^2 = \frac{1}{|\Psi|}\left(\sqrt{(hV_{00})^2 - (h_{\rm th}V_{00})^2} + 2\pi(f_{\rm pr}/2 - f_{\rm SW})\,{\rm sign}(\Psi)\right). \quad (3.16)$$

We assume that the deviation of $f_{\rm pr}$ from $2f_{\rm SW}$ is small, so that the second term in the parentheses can be neglected compared to the first term. In this case, Eq. (3.16) takes a

simple form:

$$p = B\sqrt{V_{\rm ac}^2 - V_{\rm th}^2}, \tag{3.17}$$

where $B = \Gamma/(|\Psi|V_{\rm th})$ is a constant.

3.10.3 Details of the fitting procedure

The fitting of the normalized peak power data shown in Fig. 3 of the main text to Eq. (3.15) and Eq. (3.17) was performed by the least squares method with A, B and $V_{\rm th}$ as fitting parameters. A range of data near the threshold voltage must be excluded in the fitting procedure because neither Eq. (3.15) nor Eq. (3.17) is valid at the threshold voltage. We chose the data range where $V_{\rm ac} < 0.1\,{\rm V}$ for the low-power fit and the data range where $V_{\rm ac} > 0.16\,{\rm V}$ for the high-power fit (the excluded data range is $0.1\,{\rm V}$ – $0.16\,{\rm V}$) because the best fit parameters do not change significantly upon further extension of the excluded data range. The threshold voltage given by this fitting procedure is $V_{\rm th} = 0.136\,{\rm V}$.

3.11 Parametric Resonance Signal Contributions

The sample

$$I(t) = I_{dc} + I_{ac}\cos(\omega_d t) \tag{3.18}$$

$$R(t) = R + \delta R_{PR}\cos(\omega t + \phi) + \delta R_{FMR}\cos(\omega_0 t + \psi) + \ldots \tag{3.19}$$

where R is the time averaged resistance (which can be measured in experiment).

The voltage signal measured in the experiment is due to mixing of the RF drive and resistance oscillations:

$$V(t) = I(t)R(t) \tag{3.20}$$

$$= [I_{dc} + I_{ac}\cos(\omega_d t)][R + \delta R_{PR}\cos(\omega t + \phi) + \delta R_{FMR}\cos(\omega_0 t + \psi) + \ldots] \tag{3.21}$$

Resistance oscillations account for first harmonic of PR at $\omega = \omega_d/2$. A thermal FMR term always at FMR frequency ω_0 mixes with RF as well.

$$V(t) = I_{dc}R \tag{3.22}$$

$$+ I_{dc}\delta R_{PR}\cos(\omega t + \phi) \tag{3.23}$$

$$+ I_{dc}\delta R_{FMR}\cos(\omega_0 t + \psi) \tag{3.24}$$

$$+ I_{ac}R\cos(\omega_d t) \tag{3.25}$$

$$+ I_{ac}\delta R_{PR}\cos(\omega_d t)\cos(\omega t + \phi) \tag{3.26}$$

$$+ I_{ac}\delta R_{FMR}\cos(\omega_d t)\cos(\omega_0 t + \psi) + \ldots \tag{3.27}$$

3.11.1 PR Terms

The PR term (3.26) is the mixing signal that dominates at higher powers:

$$V_{ac}^{PR}(t) = I_{dc}\delta R_{PR}\cos(\omega t+\phi) + I_{ac}\delta R_{PR}\cos(\omega_d t)\cos(\omega t+\phi) \tag{3.28}$$

$$= I_{dc}\delta R_{PR}\cos(\omega t+\phi) \tag{3.29}$$

$$+ \frac{1}{2}I_{ac}\delta R_{PR}[\cos(\omega_d t+\omega t+\phi)+\cos(\omega_d t-\omega t-\phi)] \tag{3.30}$$

$$V_{ac}^{PR}(t) = I_{dc}\delta R_{PR}\cos(\omega t+\phi) \tag{3.31}$$

$$+ \frac{1}{2}I_{ac}\delta R_{PR}\cos(\omega t-\phi) \quad \text{(SA signal)} \tag{3.32}$$

$$+ \frac{1}{2}I_{ac}\delta R_{PR}\cos(3\omega t+\phi) \tag{3.33}$$

3.11.2 FMR Terms

The FMR term (3.27) downmixes the drive frequency sweep so the signal appears to move in the SA window:

$$V_{ac}^{FMR}(t) = I_{dc}\delta R_{FMR}\cos(\omega_0 t+\psi) + I_{ac}\delta R_{FMR}\cos(\omega_d t)\cos(\omega_0 t+\psi) \tag{3.34}$$

$$= I_{dc}\delta R_{FMR}\cos(\omega_0 t+\psi) \tag{3.35}$$

$$+ \frac{1}{2}I_{ac}\delta R_{FMR}[\cos(\omega_d t+\omega_0 t+\psi)+\cos(\omega_d t-\omega_0 t-\psi)] \tag{3.36}$$

$$V_{ac}^{FMR}(t) = I_{dc}\delta R_{FMR}\cos(\omega_0 t+\psi) \tag{3.37}$$

$$+ \frac{1}{2}I_{ac}\delta R_{FMR}\cos[(\omega_d-\omega_0)t-\psi] \quad \text{(SA signal)} \tag{3.38}$$

$$+ \frac{1}{2}I_{ac}\delta R_{FMR}\cos[(\omega_d+\omega_0)t+\psi] \tag{3.39}$$

Voltage signal in SA window around $\omega = \omega_d/2$; $\omega_0 \approx \omega$:

$$V_{sig}(t) = I_{dc}\delta R_{PR}\cos(\omega t + \phi) + I_{dc}\delta R_{FMR}\cos(\omega_0 t + \psi) \tag{3.40}$$

$$+ \frac{1}{2}I_{ac}\delta R_{PR}\cos(\omega t - \phi) + \frac{1}{2}I_{ac}\delta R_{FMR}\cos[(\omega_d - \omega_0)t - \psi] \tag{3.41}$$

3.12 STO Power

Integrated power for STO (from Nat. Commun. 5, 5616 (2014)) first harmonic:

$$P_{int} = \frac{1}{2R_{50}}\left(I_{dc}\delta R_{ac}\frac{R_{50}}{R + R_{50}}\right)^2 \tag{3.42}$$

$$\delta R_{ac} = \frac{R + R_{50}}{I_{dc}\sqrt{R_{50}}}\sqrt{2P_{int}} \tag{3.43}$$

Derived from the DC-driven signal:

$$V_{sig}(t) = I_{dc}\delta R_{ac}\cos(\omega t) \tag{3.44}$$

$$V_{sig}^{rms} = \frac{1}{\sqrt{2}}I_{dc}\delta R_{ac} \tag{3.45}$$

$$V_{SA} = V_{sig}^{rms} \cdot \frac{R_{50}}{R + R_{50}} \tag{3.46}$$

$$P_{int} = \frac{V_{SA}^2}{R_{50}} = \frac{1}{2R_{50}}\left(I_{dc}\delta R_{ac}\frac{R_{50}}{R + R_{50}}\right)^2 \tag{3.47}$$

3.12.1 PR signal

But our mixing signal is different:

$$V_{sig}(t) = \frac{1}{2} I_{ac} \delta R_{PR} \cos(\omega t - \phi) \tag{3.48}$$

$$V_{sig}^{rms} = \frac{1}{2\sqrt{2}} I_{ac} \delta R_{PR} \tag{3.49}$$

$$P = \frac{1}{2R_{50}} \left(\frac{1}{2} I_{ac} \delta R_{PR} \frac{R_{50}}{R + R_{50}} \right)^2 \tag{3.50}$$

Should that P be peak power or integrated power?

$$\delta R_{PR} = \frac{R + R_{50}}{I_{ac}\sqrt{R_{50}}} \sqrt{8P} \tag{3.51}$$

3.13 Resistance Oscillations

Begin with time dependence of the angle between magnetizations as

$$\theta(t) = \theta_{mis} + \theta_{max} \sin(\omega t + \mathbf{p}) \tag{3.52}$$

where the θ_{mis} is misalignment with the reference layer and θ_{max} is the maximum precession cone angle.

And the tunneling magnetoresistance is

$$R(t) = \frac{1}{G_a} \frac{1}{1 + P_1 P_2 \cos(\theta(t))} \tag{3.53}$$

The expression to expand is

$$R(t) = \frac{1}{G_a} \frac{1}{1 + P_1 P_2 \cos[\theta_{mis} + \theta_{max} \sin(\omega t + \mathbf{p})]} \tag{3.54}$$

which has a component

$$\cos[\theta_{mis} + \theta_{max} \sin(\omega t + \mathbf{p})] = \tag{3.55}$$

$$\cos(\theta_{mis}) \cos(\theta_{max} \sin(\omega t + \mathbf{p})) - \sin(\theta_{mis}) \sin(\theta_{max} \sin(\omega t + \mathbf{p})) \tag{3.56}$$

which can be expanded in Bessel functions of the first kind.

3.13.1 Small Angle Approximation

Small angle approximation where θ_{max} is small compared to $\pi/2$; then we can expand the cosine and sine terms above in Taylor series:

$$\cos(x) = 1 - \frac{x^2}{2!} + \frac{x^4}{4!} + \ldots \tag{3.57}$$

$$\sin(x) = x - \frac{x^3}{3!} + \frac{x^5}{5!} + \ldots \tag{3.58}$$

where the small parameter will be $x = \theta_{max}\sin(\omega t + \mathbf{p})$.

$$\cos[\theta_{mis} + \theta_{max}\sin(\omega t + \mathbf{p})] \approx \cos(\theta_{mis})(1 - \frac{x^2}{2!} + \frac{x^4}{4!} + \ldots) - \sin(\theta_{mis})(x - \frac{x^3}{3!} + \frac{x^5}{5!} + \ldots) \tag{3.59}$$

$$\approx \cos(\theta_{mis})(1 - \frac{x^2}{2!}) - \sin(\theta_{mis})(x - \frac{x^3}{3!}) \tag{3.60}$$

$$\approx \cos(\theta_{mis})\left[1 - \frac{(\theta_{max}\sin(\omega t + \mathbf{p}))^2}{2!}\right] \tag{3.61}$$

$$- \sin(\theta_{mis})\left[\theta_{max}\sin(\omega t + \mathbf{p}) - \frac{(\theta_{max}\sin(\omega t + \mathbf{p}))^3}{3!}\right] \tag{3.62}$$

In our case, $\theta_{mis} \approx 90^\circ$, so $\sin(\theta_{mis})$ term remains. We can drop higher order terms in θ_{max} and keep first order

$$R(t) = \frac{1}{G_a}\frac{1}{1 - C_1\sin(\omega t + \mathbf{p})} \quad ; \quad C_1 = P_1 P_2 \sin(\theta_{mis})\theta_{max} \tag{3.63}$$

$$R(t) = \frac{1}{G_a}\frac{1}{1 - C_1\sin(\omega t + \mathbf{p})} \cdot \frac{1 + C_1\sin(\omega t + \mathbf{p})}{1 + C_1\sin(\omega t + \mathbf{p})} \tag{3.64}$$

$$= \frac{1}{G_a}\frac{1 + C_1\sin(\omega t + \mathbf{p})}{1 - C_1^2\sin^2(\omega t + \mathbf{p})} \tag{3.65}$$

$$\approx \frac{1}{G_a}(1 + C_1\sin(\omega t + \mathbf{p})) \tag{3.66}$$

which relies on $C_1 << 1$ (satisfied if $\theta_{max} \approx \sin(\theta_{max})$)

3.13.2 First Harmonic PR

Cone angle estimations for PR signal

$$R(t) = R + \delta R_{PR} \sin(\omega t + \mathbf{p}) + \dots \tag{3.67}$$

$$R(t) \approx \frac{1}{G_a}(1 + C_1 \sin(\omega t + \mathbf{p})) \tag{3.68}$$

$$R \approx \frac{1}{G_a} \tag{3.69}$$

$$\delta R_{PR} \approx \frac{1}{G_a} C_1 = \frac{1}{G_a} P_1 P_2 \sin(\theta_{mis}) \theta_{max} \tag{3.70}$$

$$\delta R_{PR} = \frac{R + R_{50}}{I_{ac}\sqrt{R_{50}}} \sqrt{8 P_{peak}} \tag{3.71}$$

$$\tag{3.72}$$

Amplitude of oscillations

$$\frac{1}{G_a} P_1 P_2 \sin(\theta_{mis}) \theta_{max} = \frac{R + R_{50}}{I_{ac}\sqrt{R_{50}}} \sqrt{8 P_{peak}} \tag{3.73}$$

$$\theta_{max} = \frac{G_a}{P_1 P_2 \sin(\theta_{mis})} \frac{R + R_{50}}{I_{ac}\sqrt{R_{50}}} \sqrt{8 P_{peak}} \tag{3.74}$$

Square of amplitude

$$\theta_{max} = 8 \left(\frac{G_a}{P_1 P_2 \sin(\theta_{mis})} \right)^2 \frac{(R + R_{50})^2}{R_{50}} \frac{P_{peak}}{I_{ac}^2} \tag{3.75}$$

Estimated δR_{PR} for a 10° cone angle, contants from hysteresis loop at $I_{dc} = 250\mu$A

$$\theta_{max} \approx 10^\circ = 0.1745329 \text{ rad} \tag{3.76}$$

$$P_1 P_2 \approx 0.2513 \approx 50\% \text{ polarization} \tag{3.77}$$

$$R = 636\,\Omega (H = 0.06 \text{ kG}) \tag{3.78}$$

$$G_a = 00015776826\,(1/\Omega) \tag{3.79}$$

$$\tag{3.80}$$

$$\rightarrow \sin(\theta_{mis}) = \sin(90.388^\circ) = 0.999977 \approx 1 \tag{3.81}$$

$$\rightarrow R \approx 633.84\,\Omega \tag{3.82}$$

$$\rightarrow \delta R_{PR} = 27.8003\,\Omega \tag{3.83}$$

3.13.3 First Harmonic ST-FMR

Cone angle estimation for amplitude-modulated ST-FMR signal

$$R(t) = R + \delta R_{FMR} \sin(\omega t + \mathbf{p}) + \ldots \tag{3.84}$$

$$R(t) \approx \frac{1}{G_a}(1 + C_1 \sin(\omega t + \mathbf{p})) \tag{3.85}$$

$$R \approx \frac{1}{G_a} \tag{3.86}$$

$$\delta R_{FMR} \approx \frac{1}{G_a} C_1 = \frac{1}{G_a} P_1 P_2 \sin(\theta_{mis}) \theta_{max} \tag{3.87}$$

ST-FMR signal amplitude

$$V_{mix}(t) = I_{ac}R\sin(\omega t + \mathbf{p}) + I_{ac}\sin(\omega t)\cdot\delta R_{FMR}\sin(\omega t + \mathbf{p}) \tag{3.88}$$

$$= I_{ac}R\sin(\omega t + \mathbf{p}) + I_{ac}\sin(\omega t)\cdot\delta R_{FMR}[\sin(\omega t)\cos(\mathbf{p}) + \cos(\omega t)\sin(\mathbf{p})] \tag{3.89}$$

$$= I_{ac}R\sin(\omega t + \mathbf{p}) + I_{ac}\delta R_{FMR}[\sin^2(\omega t)\cos(\mathbf{p}) + \sin(\omega t)\cos(\omega t)\sin(\mathbf{p})] \tag{3.90}$$

$$= I_{ac}R\sin(\omega t + \mathbf{p}) + \frac{1}{2}I_{ac}\delta R_{FMR}[(1 - \cos(2\omega t)\cos(\mathbf{p}) + \sin(2\omega t)\sin(\mathbf{p})] \tag{3.91}$$

$$= I_{ac}R\sin(\omega t + \mathbf{p}) + \frac{1}{2}I_{ac}\delta R_{FMR}[\cos(\mathbf{p}) - \cos(2\omega t + \mathbf{p})] \tag{3.92}$$

$$V_{dc} = \frac{1}{2}I_{ac}\delta R_{FMR}\cos(\mathbf{p}) \tag{3.93}$$

Amplitude of oscillations

$$\delta R_{FMR} = \frac{2V_{dc}}{I_{ac}\cos(\mathbf{p})} = \frac{1}{G_a}P_1P_2\sin(\theta_{mis})\theta_{max} \tag{3.94}$$

$$\theta_{max} = \frac{G_a}{P_1P_2\sin(\theta_{mis})}\frac{2V_{dc}}{I_{ac}\cos(\mathbf{p})} \tag{3.95}$$

Square of amplitude

$$\theta_{max}^2 = \left(\frac{G_a}{P_1P_2\sin(\theta_{mis})}\frac{2V_{dc}}{I_{ac}\cos(\mathbf{p})}\right)^2 \tag{3.96}$$

3.13.4 Estimated cone angle for P = -10 dBm

V_{dc} taken from single-Lorentzian fit to FMR amplitude

$$V_{dc} = 0.00497493979907068V \tag{3.97}$$

$$P_1P_2 \approx 0.2615 \approx 50\%\text{polarization} \tag{3.98}$$

$$G_a \approx 0.0015576277592278888(1/\Omega) \rightarrow 636.99\Omega \tag{3.99}$$

$$I_{ac} \approx 291.97\mu A(R \approx 635\Omega) \tag{3.100}$$

$$\cos(\phi) \approx 1; \sin(\theta_{mis}) \approx 1 \tag{3.101}$$

$$\theta_{max} = \frac{G_a}{P_1P_2\sin(\theta_{mis})}\frac{2V_{dc}}{I_{ac}\cos(\phi)} \tag{3.102}$$

$$\theta_{max} = 0.20458718133861728\text{rad} = 11.721982033180407^\circ \tag{3.103}$$

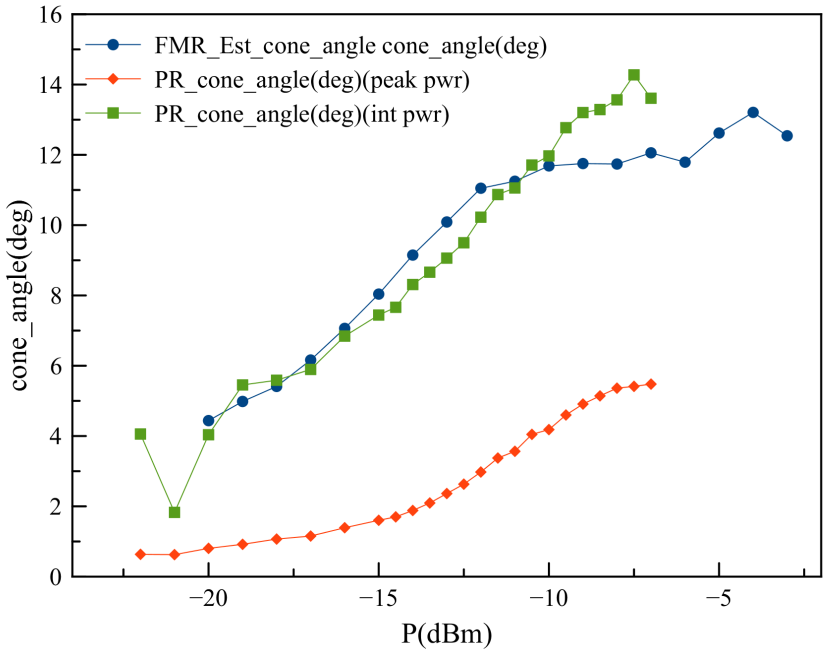

Figure 3.12: **Calculated Cone Angles.** Cone angles calculated using the small angle approximation and MR measurements.

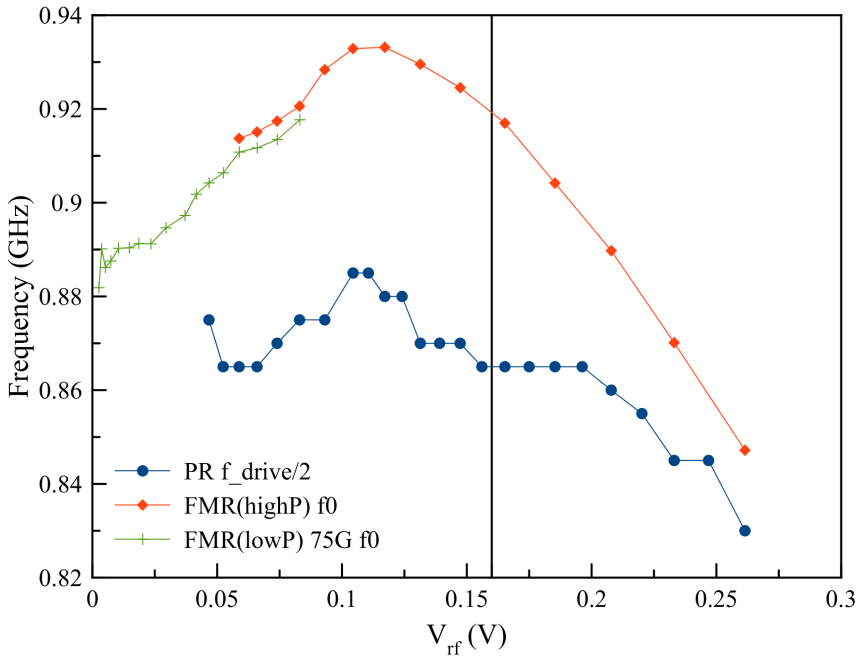

Figure 3.13: **Comparison of Resonance Frequencies.** Resonance frequencies of the measured ST-FMR (orange) and parametric resonance (blue).

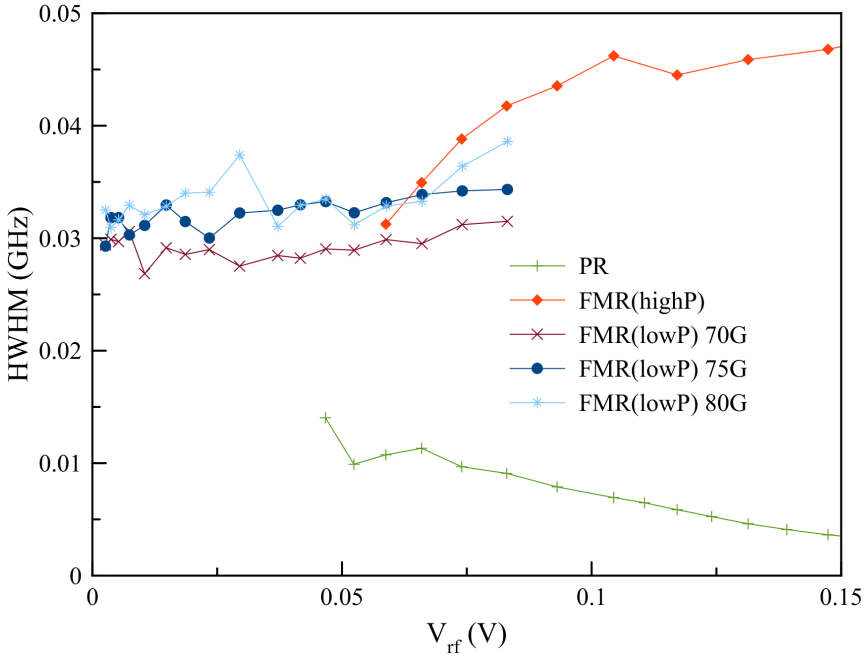

Figure 3.14: **Comparison of Resonance Linewidths.** Resonance linewidths of the measured ST-FMR and parametric resonance.

Chapter 4

Control of Spin Waves by VCMA

4.1 Spin Wave Logic

A spin wave-based logic has the potential to be very low energy [21]. The goal is to develop logic devices based on propagating spin waves in nanostructures. In this scheme, waveguides direct the propagation of spin waves through structures (called "gates") where logic operations can be carried out or information states can be read. Information can be carried in the spin wave amplitude and phase as it arrives at a gate. Logic operations are then carried out through manipulation of spin wave phase, spin wave amplitude, and interference between spin waves. [36, 21]

There are many schemes that have been proposed for an all-spin-wave logic system. [21] This thesis will focus on a scheme proposed which uses a majority logic gate, a spin wave amplifier, and a spin wave inverter as the fundamental elements to build more complex logic circuits. During the course of this work, the focus has been on achieving control of spin wave propagation by using voltage gates to adjust perpendicular anisotropy via the voltage-controlled magnetic anisotropy (VCMA) effect. In addition to the components listed for a

spin wave logic "toolbox", this work also considers how to handle errors in computation and how to correct them. The ultimate goal is to eventually develop all the basic parts necessary for a working spin wave logic that is able to perform all logic operations needed to build a computer.

4.2 Micromagnetic Simulations

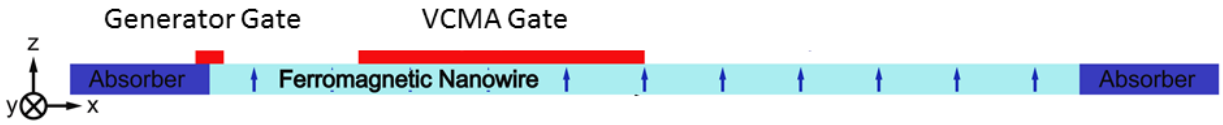

Figure 4.1: **Nanowire Schematic for Simulations.** Illustration of the simulated nanowire configuration in simulations. The absorbers remove reflections at the ends of the nanowire, which would produce standing spin wave modes rather than propagating waves.

I performed micromagnetic simulations for the described spin wave devices to show the ability of VCMA to control spin waves. I mainly used the MuMax3 code with some input from OOMMF simulations to help confirm repeatability. MuMax3 was chosen for several reasons. One reason is that the GPU-accelerated MuMax3 code improves computational time for large systems like nanowires and thin films. While a GPU-accelerated version of some modules in OOMMF has been developed at the time of this writing, not all modules important to nanomagnetic dynamics have been developed such as the spin transfer torque evolver (SpinXferEvolve) or the Dzyaloshinski-Moriya energy (Oxs_DMI). In addition, the MuMax3 code allows specification of a time-dependent perpendicular magnetic anisotropy in a simple way, which the OOMMF code does not support at all at the time of this writing. Figure 4.1 illustrates the configuration of the nanowires in subsequent simulations data.

Example simulation data is shown in Figure 4.2, illustrating the ability to take magnetization snapshots in the time domain or calculate the Fast Fourier Transform (FFT) for frequency domain analysis.

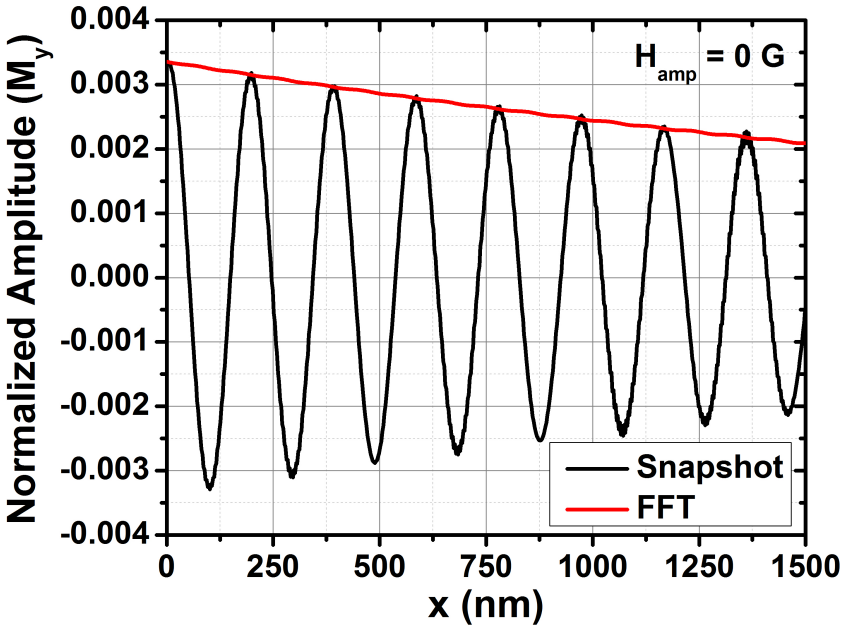

Figure 4.2: **Example Simulation Data.** (black) Magnetization amplitude at a particular moment in simulation time, essentially showing spin wave amplitude and phase, as a function of distance along the nanowire. (red) FFT analysis performed for the same simulation, which captures the same information.

4.3 Majority Logic Gate

The devices investigated in this work are based on ferromagnetic nanowire waveguides for spin waves and will utilize voltage gates to perform logic operations on the spin waves. The proposed scheme [43] uses the spin wave phase as the state variable to store information as a binary bit. For example, a spin wave with phase of 0 degrees arriving at a gate could represent a logical 0 state while a spin wave arriving with 180 degrees phase difference with respect to 0 can be called a logical 1 state.

The majority gate relies on having an odd number of at least three (3) input spin waves which meet at a junction and interfere. The spin wave interference results in a single output spin wave with logic state that is a majority of the input logic states. For example, with three inputs having logical states 0, 0, and 1, the output spin wave should have output logical state 0 after encountering the majority gate. The continuous nature of the spin wave phase also allows for non-Boolean logic schemes, but that is beyond the scope of the devices investigated in this thesis.

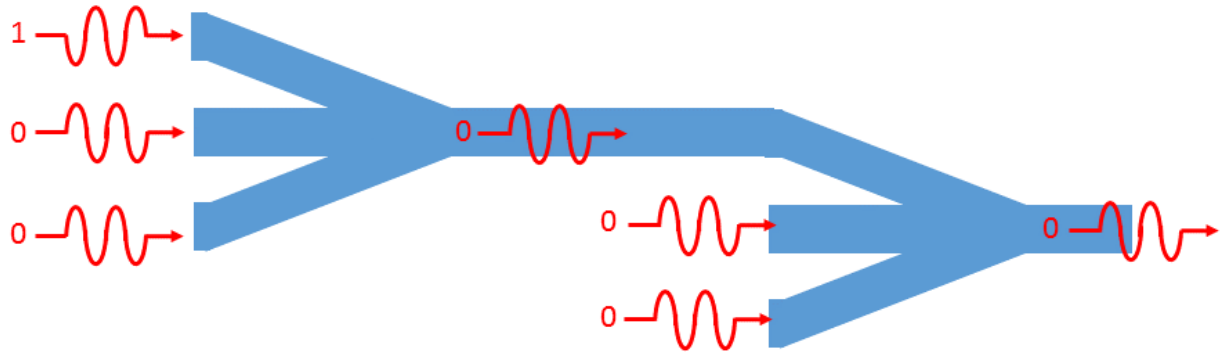

Figure 4.3: **Majority Logic Gate.** Illustration of the spin wave majority logic gate operation. Three spin waves with equal amplitude (possibly different phases) meet and interfere to produce an output spin wave with phase equal to the majority of the input phases.

As a fundamental piece of the spin wave logic toolbox, the majority gate has been shown to work for micrometer-scale devices through numerical simulations [46]. However, there remain unresolved issues that arise when considering the case of further operations with majority gates that are added after the first gate. When this cascading of majority gates occurs, the input spin waves of the second majority gate (and beyond) must have the same spin wave amplitudes. The logic operation requires this condition so that the spin wave interference will result in the output spin wave having the proper phase to represent the majority of the input logic states. As a consequence, the output spin wave amplitude should have the same amplitude as the input spin waves. Ideally, only its phase should indicate the logic operation.

In addition, the output spin wave from a majority gate will decay in amplitude before reaching a second majority gate. Thus, to maintain proper amplitudes for further operations, a spin wave amplifier is needed and should be implemented between successive majority logic gates.

4.4 Spin Wave Inverter and Phase Control

The spin wave inverter is used to perform a logicical NOT operation, which turns a logical state 0 into a logical state 1 and vice versa. In the scheme proposed by [Khitun and Wang], the phase encodes the 0s and 1s so the inverter adds a 180-degree phase shift to the incoming spin wave to perform the logic operation. Figure 4.4 schematically illustrates this function. Fundamentally, this operation requires the abilty to reliably control the phase of a propagating spin wave.

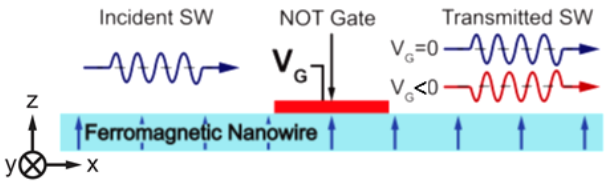

Figure 4.4: **NOT Gate.** Illustration of the spin wave NOT gate (or spin wave inverter) functionality. Spin waves transmit as normal with no voltage applied to the gate, but their phase is flipped when applying a DC voltage.

Another basic way to control spin wave propagation is to be able to turn on or turn off spin wave propagation through the waveguide. This can be accomplished by applying a direct voltage bias to the VCMA gate, which will locally change the PMA of the ferromagnet. Propagating spin waves will then encounter a region of sharply changed energy and reflect strongly, thus cutting off propagation through the waveguide. Schematically, this is shown in Figure 4.5, where the spin wave dispersion relation is locally changed so that the spin

waves are forbidden to travel through the region affected by the gate. There is a particular voltage beyond which the spin waves can no longer propagate.

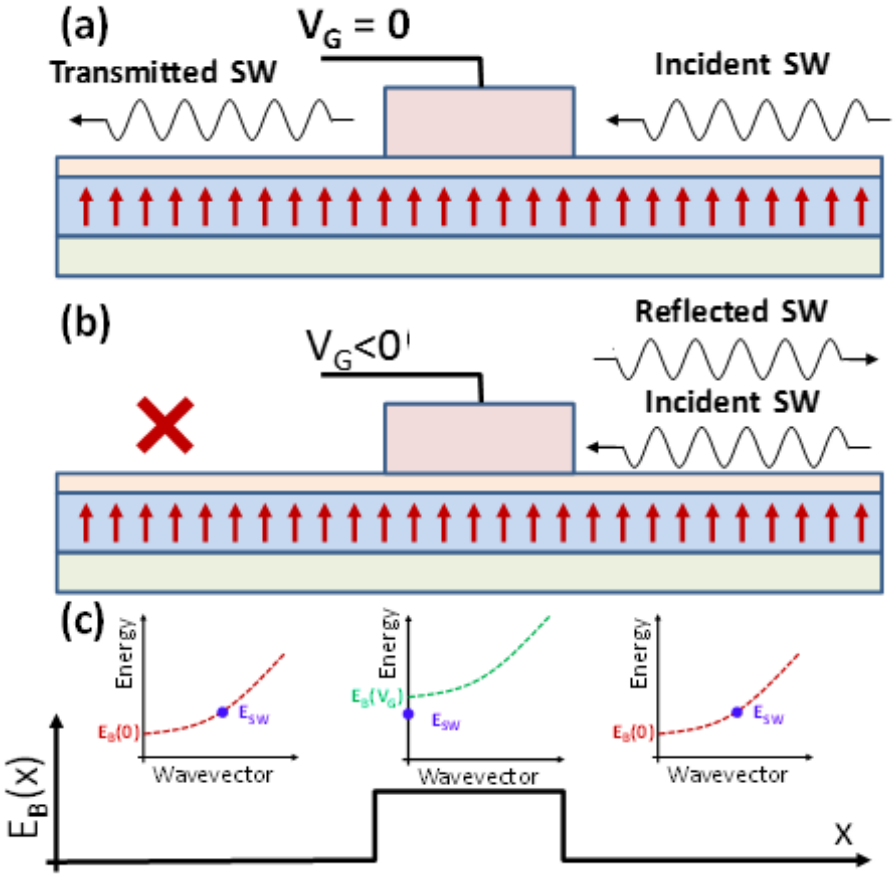

Figure 4.5: **Spin Wave Field Effect Transistor.** Illustration of the spin wave field effect transistor. (a) When no voltage is applied, spin waves propagate as usual. (b) Local anisotropy modified by VCMA stops spin wave propagation. (c) Schematics of spin wave dispersion relation depicting the situation in (b), where locally changed anisotropy raises a potential barrier for spin wave propagation.

We run simulations to test how the VCMA gate can manipulate the phase of spin waves as well as turn spin wave propagation on and off. This is made possible by varying the voltage applied to the gate. As seen in Figure 4.6 and Figure 4.7, the phase of the spin wave leaving the gate can be varied linearly with respect to the VCMA effective field. This, in turn, means that the spin wave phase can be varied linearly with direct voltage bias applied to

the gate. For a particular value of voltage bias, the phase of the propagating spin wave is changed from 0 degrees to 180 degrees out of phase.

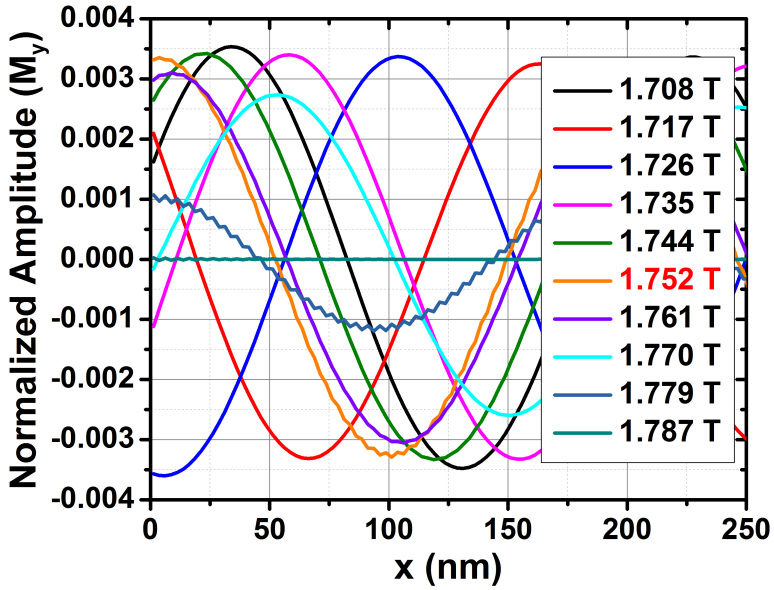

Figure 4.6: **Spin Wave Phase Control Snapshots.** Magnetization snapshots as a function of distance from the VCMA gate, showing a significant effect on the spin wave phase as well as the amplitude.

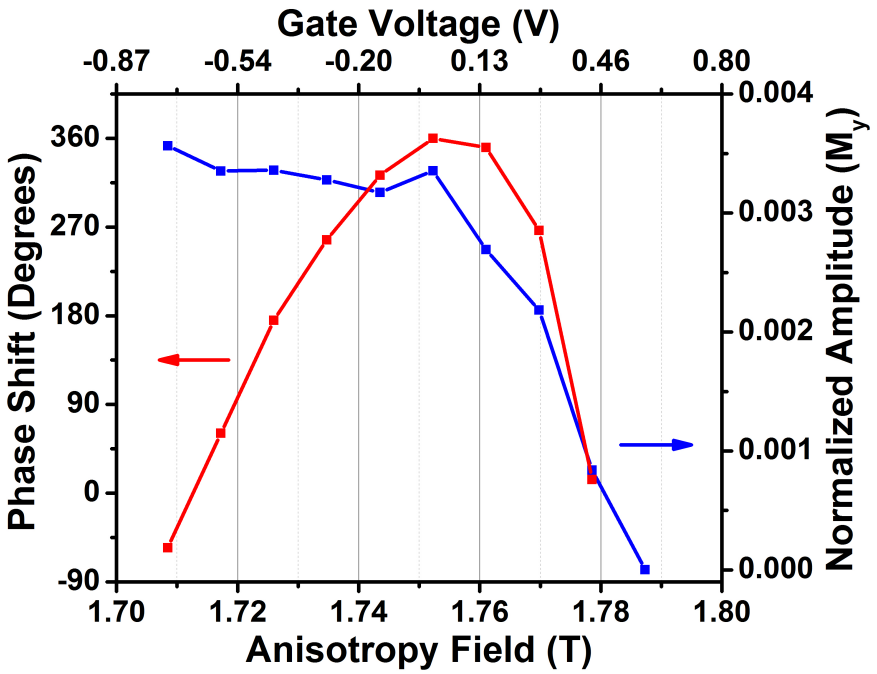

Figure 4.7: **Phase and Amplitude vs. Anisotropy.** Phase and amplitude of spin waves shown in Figure 4.6 plotted as a function of anisotropy field with equivalent voltage values for the Fe/MgO system.

In essence, this work is a demonstration of a basic NOT gate for propagating spin waves, along with a transistor-like control of spin wave propagation (i.e., turning on and off). Furthermore, it has been shown that voltage can manipulate the phase of spin waves arriving at later gates along the waveguide, allowing for another degree of freedom in perhaps more complex logic schemes.

4.5 Parametric Amplification

Another basic issue to be addressed in spin wave logic devices is the presence of damping. Once a spin wave leaves one logic gate, it must travel to another element for further logic operations or read out. Damping, which is intrinsic to all magnetic systems, will degrade

the amplitude of spin waves traveling along a waveguide. Therefore, there is a need for spin wave amplification to maintain proper fan out of logic operations. Figure 4.8 shows the basic schematic of a parametric amplifier and how it was implemented in simulations.

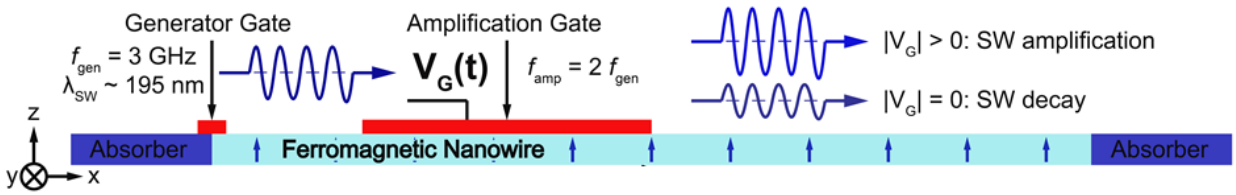

Figure 4.8: **Parametric Amplifier.** Schematic of a nanowire spin wave waveguide with absorbing boundary conditions and two gates: one generator gate to generate spin waves and one VCMA parametric amplifier gate to change local anisotropy at microwave frequencies.

Moreover, the basic majority logic gate which has been demonstrated numerically [46] requires multiple spin waves to arrive at the gate with *the same amplitude*, relying on interference of spin waves to perform the majority operation. However, the output of said majority gate can be different from the inputs by a factor of 3. This presents a problem for cascading majority logic gates, since the inputs for the second gate could have very different amplitudes and intereference would no longer result in the majority operation.

Fortunately, this set of simulations shows that the VCMA gate, when driven parametrically by microwave voltage, can not only amplify spin waves but also provides nonlinear gain to renormalize the amplitudes of outgoing spin waves. In an early set of simulations performed using OOMMF, the effect of parametric excitation is simulated by an external magnetic field that is applied in the amplification gate region at microwave frequencies.

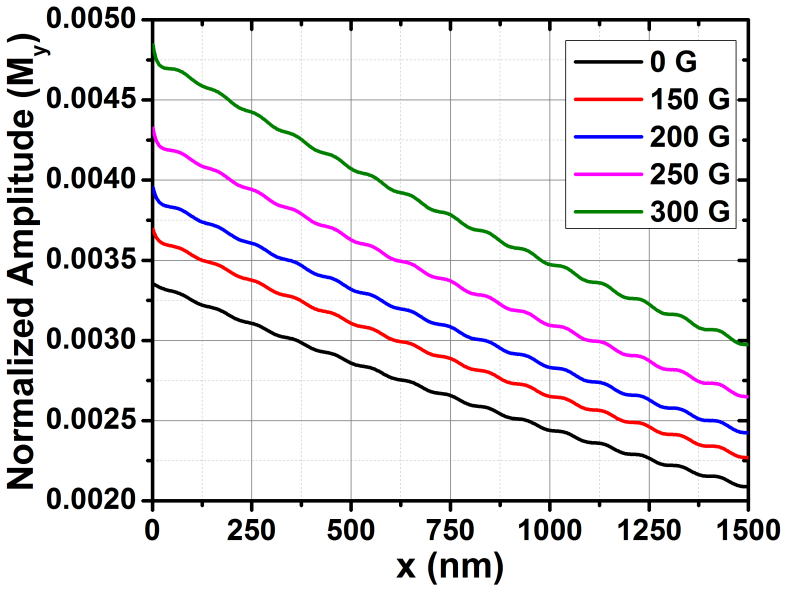

Figure 4.9: **Amplification as a Function of Excitation Amplitude.** Spin wave amplitude plotted as a function of distance from the amplifier gate. Different curves correspond to different amplitudes of parametric drive.

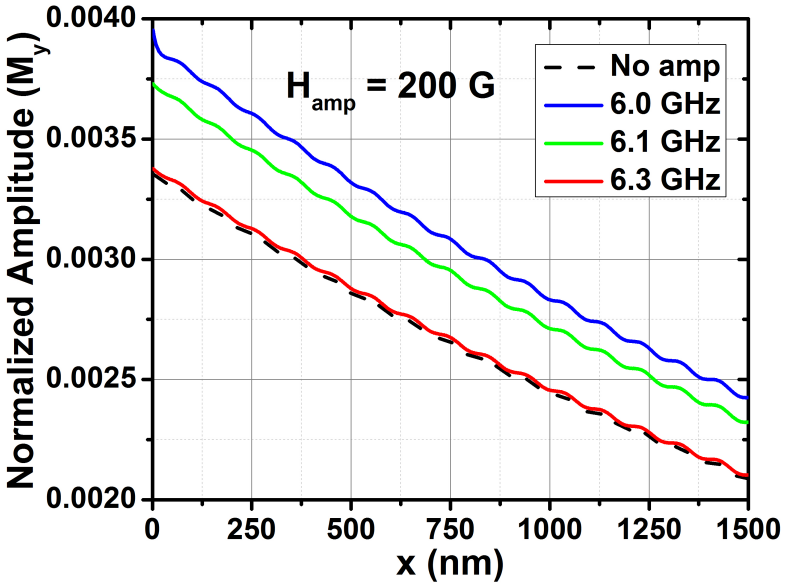

Figure 4.10: **Amplification as a Function of Excitation Frequency.** Spin wave amplitude plotted as a function of distance from the amplifier gate. Different curves correspond to different drive frequencies and illustrate the effect of moving away from exactly twice the spin wave's frequency.

At sufficient drive amplitudes, the parametric excitation shows amplification of spin waves. This can be seen in Figure 4.9, which shows the spin wave amplitude as a function of distance from the VCMA parametric gate. As the drive amplitude is increased, the spin wave amplitude increases as well. In addition, this is a resonant effect due to parametric drive, because changing the frequency of the drive away from exactly twice the spin wave frequency significantly reduces the amplification, as shown in Figure 4.10.

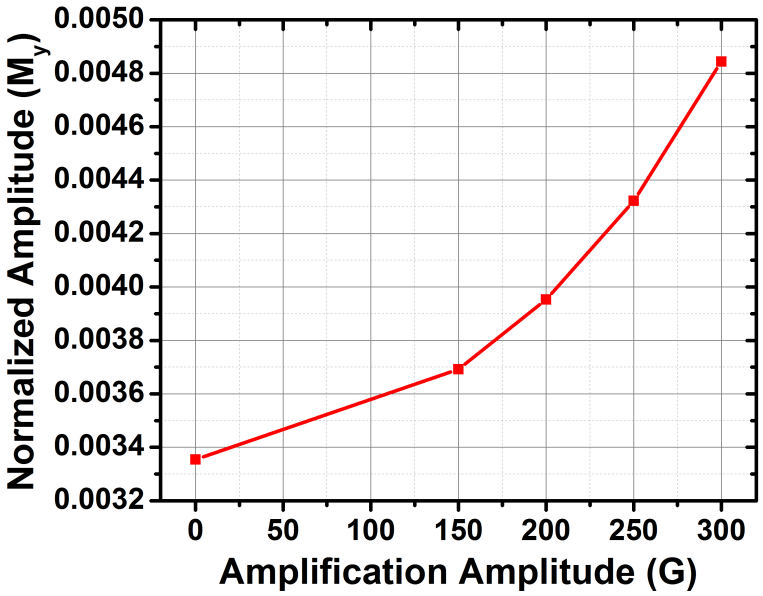

Figure 4.11: **Nonlinear Amplification.** Amplitude of spin waves as a function of parametric drive amplitude, showing a nonlinear amplification as drive amplitude is increased.

As seen in Figure 4.11, the gain of the VCMA parametric amplifier turns out to be nonlinear as a function of drive amplitude. In a second set of simulations, we explored this aspect of the amplifier in more detail. As seen in Figure 4.12, the newest set of simulations reproduce the earlier result and show amplification of spin waves at a drive amplitude corresponding to a 2 % change in the perpendicular anisotropy energy.

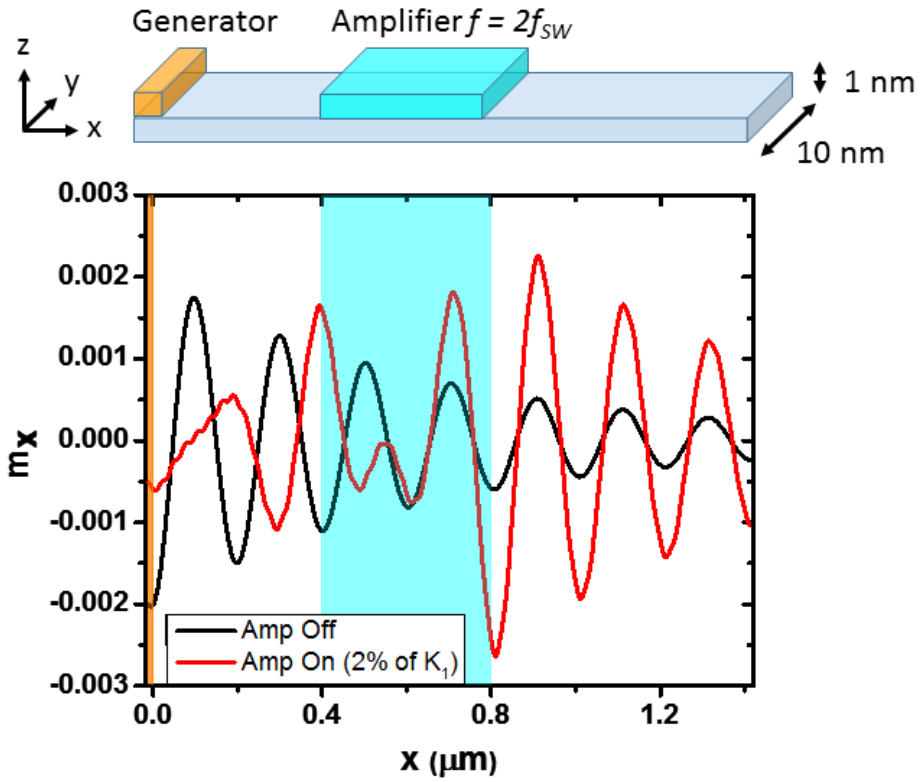

Figure 4.12: **Parametric Amplifier and Amplification.** (upper) Schematic of the nanowire configuration in simulation. Orange and cyan match the generator and amplifier regions, respectively. (lower) Plot of the spin wave amplitude as a function of distance along the nanowire with the amplifier OFF (black) and ON (red).

Also reproduced is the nonlinear gain as a function of drive amplitude, which can be seen in Figure 4.13. The gain is defined as the ratio of output spin wave amplitude to the input spin wave amplitude, after the gate. What is plotted is the power gain, which is proportional to the square of spin wave amplitude.

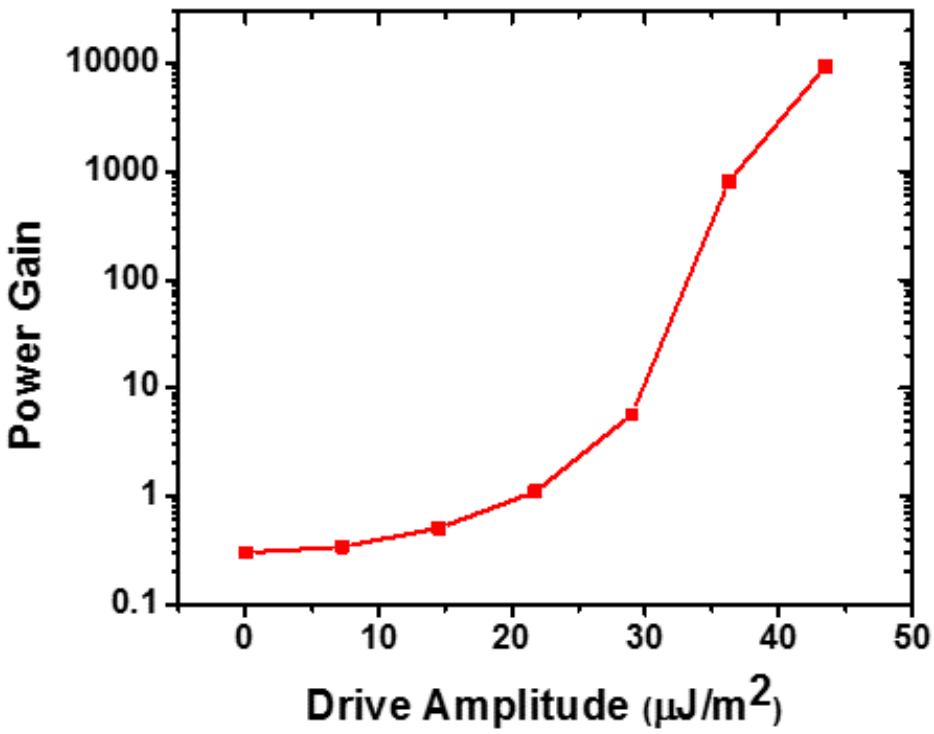

Figure 4.13: **Nonlinear Gain.** The parametric amplifier shows nonlinear gain as a function of drive amplitude, as shown in earlier simulations (Figure 4.11).

In addition, we explored the effects of the amplifier gate when the incoming spin wave phase is varied. Figure 4.14 shows the gain of the amplifier as a function of incoming spin wave phase at different drive amplitudes. At lower drive amplitudes, the gain is relatively insensitive to the phase. At sufficiently high amplitude, the gain has a strong dependence on the incoming spin wave phase.

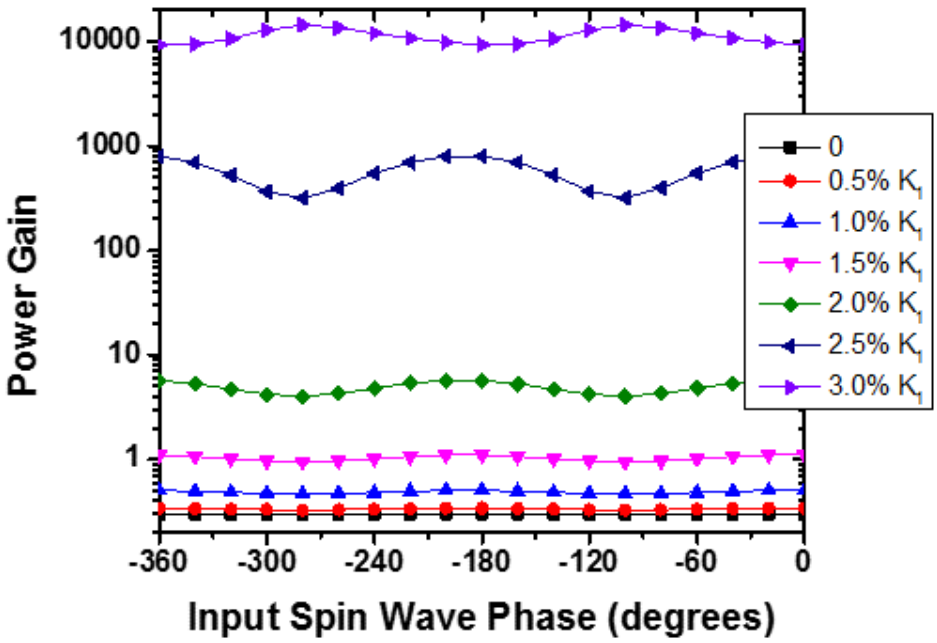

Figure 4.14: **Gain vs. Input Phase.** The amplifier gain has a strong dependence on input spin wave phase at sufficiently high drive amplitudes.

The dependence on the incoming spin wave phase warrants an examination of the outgoing spin wave phase, shown in Figure 4.15. The outgoing spin wave phase depends strongly on the incoming spin wave phase. One can see plateaus in the graph, which indicate regimes when many incoming spin wave phases exit the gate with the same phase. This is the desired phase correction described earlier, where logical 0s and 1s remain 0s and 1s because relatively large deviations of $\pm 45^\circ$ can be corrected to the intended spin wave phase.

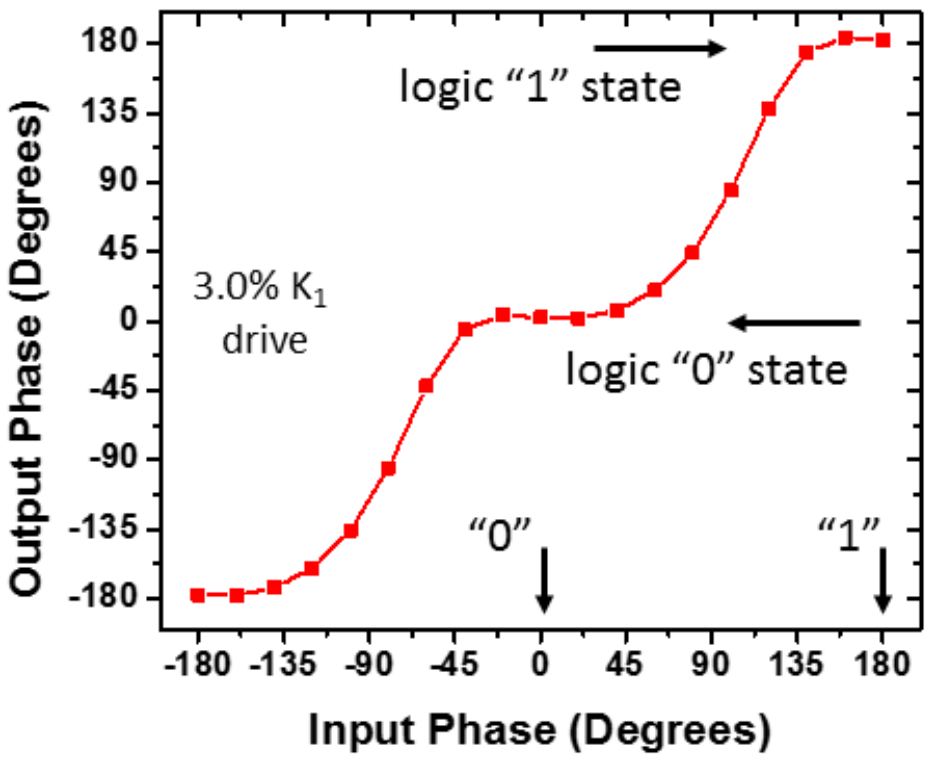

Figure 4.15: **Phase Correction.** The output spin wave phase has a strong dependence on the input spin wave phase at drive amplitude of 3 % of PMA energy. Plateaus indicate regions of input spin wave phase where accumulated phase errors would be corrected to the proper spin wave phase.

Additionally, the nonlinear gain of the VCMA parametric amplifier also provides amplitude correction in the context of the majority logic gate. In Figure 4.16, the parametric amplifier gate is turned off, and the incoming spin waves have amplitude ratio of 3:1. This case matches the possible outputs of the basic majority logic gate. When the amplifier is turned on, as shown in Figure 4.17, the outgoing spin waves have amplitude ratio 1:1.

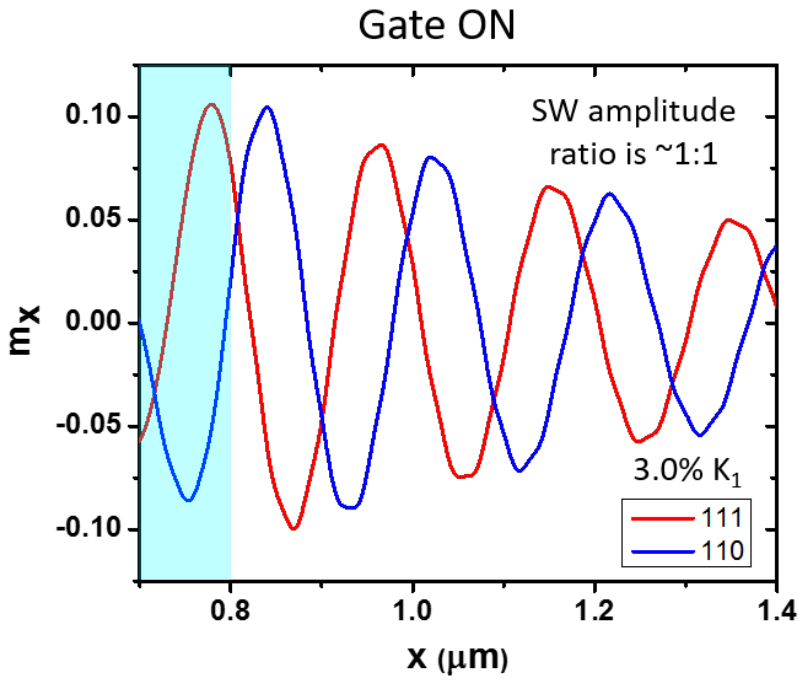

Figure 4.16: **Amplitude Correction OFF.** Simulated output spin wave amplitudes of a majority logic gate which have spin wave amplitude ratio of 3:1 when the amplifier is OFF.

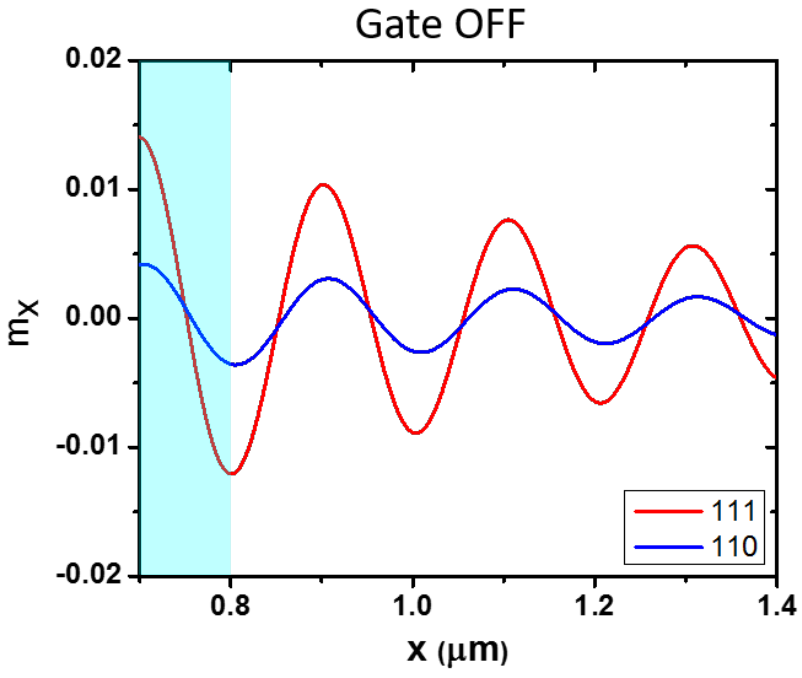

Figure 4.17: **Amplitude Correction ON.** Simulated output spin wave amplitudes of a majority logic gate which have spin wave amplitude ratio of 1:1 when the amplifier is ON.

One can note that there is a ≈45° phase shift introduced for this particular gate. With further optimization, the gate could be placed such that output spin waves have the same phase. In addition, the placement of a phase corrector gate after the amplitude correction gate can then eliminate the phase error.

The VCMA spin wave gate can be the element that provides the toolbox of spin wave control needed to build a working spin wave logic based on majority gates. An application of DC voltage in one polarity controls spin wave phase, allowing for creation of a spin wave inverter or NOT gate. Reversing the polarity of DC voltage can also suppress spin wave propagation, like a spin wave field effect transistor.

Applying a microwave voltage at the VCMA gate at twice the spin wave frequency amplifies the system parametrically. The nonlinearity of the amplifier gain re-normalizes the spin wave amplitudes of majority logic gate outputs. At sufficiently high drive amplitudes, the VCMA parametric amplifier also corrects for accumulated phase errors of spin waves that have propagated along various waveguides. The drive amplitude at which phase correction occurs is in the regime *above the parametric generation threshold*, a very nonlinear regime that our theory collaborators are exploring in further detail analytically.

Chapter 5

Temperature Dependence of the Stoner-Wohlfarth Astroid

5.1 The Stoner-Wohlfarth Astroid and Switching

The study of magnetic tunnel junctions has garnered a lot of interest recently due to their possible applications as memory elements. One type of memory element in development is the spin transfer torque magnetic random access memory (STT-MRAM). Its implementation typically involves a MgO-based MTJ that has a pinned synthetic antiferromagnet (usually comprised of Co and Fe alloys) and a free magnetic layer (typically CoFeB of some type) that easily manipulated by spin transfer torque. The memory bits "0" and "1" are encoded in the free layer magnetization direction, either parallel or anti-parallel to the reference layer (the top magnetic layer of the SAF). The memory readout is then done by reading the resistance state of the MTJ, since a low resistance indicates a parallel free layer and the high resistance state indicates an anti-parallel alignment.

Other MRAM schemes with MTJs use various methods of manipulating the free layer and switching (including research into VCMA switching), but generally studies of the free layer nanomagnets become critical for understanding the switching properties of MRAM elements. One of the key properties of a nanomagnet is its thermal stability, which is a measure of its ability to stay in a single magnetic state in the presence of thermal fluctuations. A common practice is to design devices with only uniaxial anisotropies to keep the nanomagnet thermally stable. This can be accomplished by shaping the nanopillar into elliptical cross section for in-plane magnetized devices or using circular cross sections for the nanopillars and implementing materials with high perpendicular anisotropy for out-of-plane oriented devices.

In either case, the energy landscape for uniaxial anisotropy energy provides two stable states at the bottom of two energy wells. In between are two saddle points which mark local maxima for the energy, and the difference between these energies and the bottom of the wells represent the energy barrier that must be crossed to switch the magnetization from one stable state to another. Assuming a uniaxial anisotropy of the form:

$$E = K_{u1} V \sin^2(\theta) = K_{u1} V (1 - (\mathbf{m} \cdot \mathbf{u})^2), \tag{5.1}$$

where the K_{u1} is the uniaxial anisotropy constant and V is the volume of the nanomagnet. The thermal stability of the nanomagnet is characterized by the energy barrier and can be expressed as:

$$\Delta = \frac{K_{u1}}{k_B T} \tag{5.2}$$

where k_B is the Boltzmann constant and T is the temperature.

The thermal stability parameter, Δ, also characterizes the probability of switching from one magnetic state to another. In the Arrhenius model, the fluctuations of magnetization due to

temperature are modelled as random attempts to switch the magnetization from one state to another. In this model, the probability is proportional to an exponential to the power of the thermal stability parameter:

$$\tau = \tau_0 e^{\Delta} \tag{5.3}$$

where τ is the lifetime of the magnetic state and τ_0 is the attempt time of the magnetization to switch.

There have been a few methods developed to measure the thermal stability parameter, including measuring the write error rate [47], measuring the read disturb rate , and measurements of the hard-axis hysteresis loops [44]. While these methods work to varying degrees, they have some caveats. The bit error rate measurement relies on delivering microwave switching pulses to a sample and measuring the high probability tail to error rates as low as 10^{-6} and below. This requires a high throughput of voltage pulses, which can heat the sample and change the effective barrier being measured. In the case of measuring the distribution of switching fields, the rate of the field sweep can affect the extracted thermal stability parameter. Finally, the hard-axis hysteresis loop is difficult to get exactly correct. Small misalignments between the field and the hard axis of the sample can significantly change the measured hysteresis curve. Since the parameter is extracted from the slope of this curve, the values can change significantly from the actual thermal stability.

Here, I will describe a method to measure the thermal stability of the sample using measurements of the Stoner-Wohlfarth astroid as a function of temperature. The Stoner-Wohlfarth model describes a nanomagnet with an ellipsoidal shape that is single-domain and uniformly rotates in the presence of an external magnetic field, which switches the nanomagnet and can be applied at various angles within one of the symmetry planes of the magnet. The Stoner-Wohlfarth astroid is the curve that characterizes the switching fields of the nanomag-

net, so named because the functional form of the curve is that of an astroid. The equation is:

$$h_x^{1/3} + h_y^{1/3} = 1 \tag{5.4}$$

where h_x and h_y are the x and y components of the applied field with respect to the symmetry axis of the ellipsoid. The fields are normalized to the switching field, which depends on the temperature of the sample.

5.2 Effect of Temperature on the Stoner-Wohlfarth Astroid of a Uniaxial Nanomagnet

The Stoner-Wohlfarth astroid of a uniaxial nanomagnet at a finite temperature has smaller area than the Stoner-Wohlfarth astroid at zero temperature. A schematic of this is shown in Figure 5.1, where the anisotropy field H_k is determined from the zero-temperature astroid as the hard-axis field (H_h) at which the width of the astroid curve becomes zero. At a non-zero temperature, the astroid curve shrinks due to thermally activated switching of magnetization. The width of the finite-temperature astroid curve becomes zero at a value of the hard-axis field smaller than H_k. We will refer to the field at which the width of the finite-temperature astroid curve becomes zero as H_0.

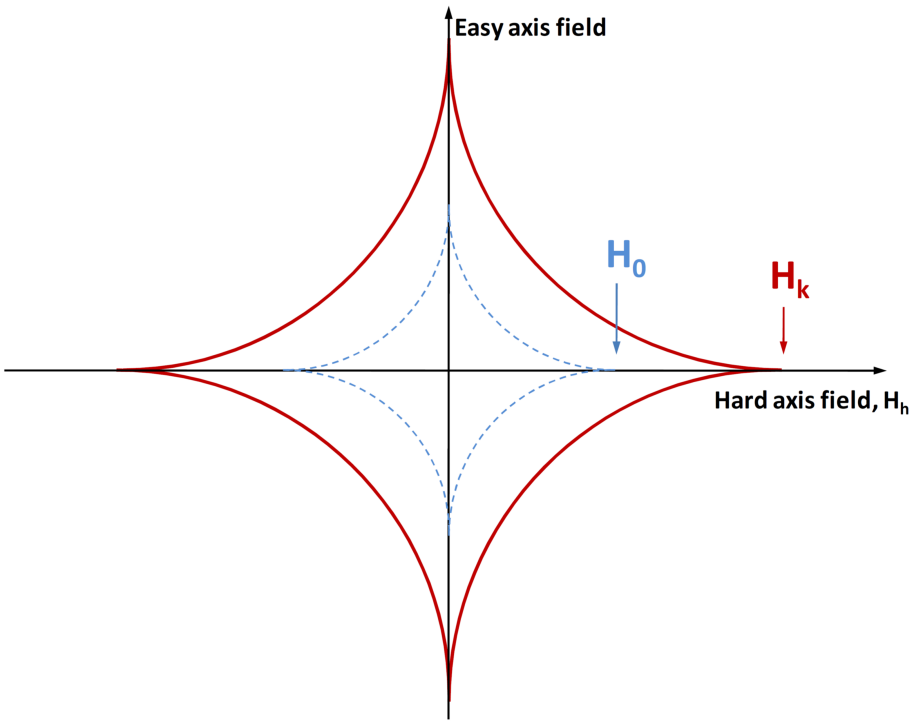

Figure 5.1: **Astroid Schematic.** Schematic Stoner-Wohlfarth astroid curve for a uniaxial nanomagnet. The red solid line is the zero-temperature astroid. The anisotropy field of the nanomagnet, Hk, can be determined from the astroid as the hard-axis field (H_h) at which the width of the astroid curve becomes zero (marked by a red arrow). At a non-zero temperature, the astroid curve shrinks due to thermally activated switching of magnetization. The width of the curve becomes zero at a smaller value of the hard-axis field, which we call H_0 (marked by blue a arrow).

Experimental finite-temperature measurements of the astroid curve give H_0, the minimum hard-axis field at which the easy-axis hysteresis loop width becomes zero. The goal is to derive a relation for extracting H_k from the measured value of H_0. This is an important procedure because H_k is the uniaxial anisotropy field that determines the zero-field thermal stability of the nanomagnet:

$$\Delta = \frac{H_k M_s V}{2k_B T} \tag{5.5}$$

where M_s is the saturation magnetization of the nanomagnet and V is its volume.

At a finite temperature, the width of the astroid curve on the hard axis field becomes zero when thermally-activated switching time becomes approximately equal to the hysteresis loop measurement time. The thermally activated switching time, t_s, is given by

$$t_s = \tau_0 \exp\left(\frac{E_b(H_h)}{k_B T}\right) \tag{5.6}$$

where $\tau_0 \approx 10^{-10}$ seconds is the attempt time (approximately inverse of the ferromagnetic resonance frequency) and $E_b(H_h)$ is the barrier between two energy minima of the nanomagnet as a function of hard-axis field bias. Assuming that the hysteresis loop measurement time is 1 second ($t_s = 1\,\text{sec}$, consistent with NIST rate of 1 Hz), we can solve Eq. 5.6 for H_h, and thereby find the value of H_h for which the hard-axis hysteresis loop width becomes zero (which by definition is the field H_0).

To solve Eq. 5.6, we need to find the functional form of $E_b(H_h)$. TO derive the expression for $E_b(H_h)$, let us write magnetic energy of a uniaxial ferromagnet subjected to a hard axis field as a function of angle, θ, between the easy axis of the uniaxial anisotropy and the directino of magnetization:

$$E(\theta) = \frac{H_k M_s V}{2} \sin^2(\theta) - H_k M_s V \sin(\theta) \tag{5.7}$$

(Unequal) maxima of the energy as a function of θ are found for $\theta_{max} = \pm\pi/2$. Minima of the energy are found at $\sin(\theta_{min}) = \frac{H_h}{H_k}$. The barrier energy can be found as the difference between energy at the local maximum separating two equivalent global minima and energy at one of the minima:

$$E_b(H_h) = E\left(\frac{\pi}{2}\right) - E(\theta_{min}). \tag{5.8}$$

Using Eq. 5.7, we obtain:

$$E_b(H_h) = \frac{H_k M_s V}{2}\left(1 - \frac{H_h}{H_k}\right)^2 \equiv k_B T \Delta \left(1 - \frac{H_h}{H_k}\right)^2 \tag{5.9}$$

where Δ is the dimensionless thermal stability of the nanomagnet in zero external field. Inserting Eq. 5.9, we obtain:

$$k_B T \Delta \left(1 - \frac{H_0}{H_k}\right)^2 = k_B T \ln\left(\frac{t_s}{\tau_0}\right) = k_B T \widetilde{\Delta} = 23 k_B T \tag{5.10}$$

Where we have introduced a dimensionless parameter $\widetilde{\Delta} = \ln\left(\frac{t_s}{\tau_0}\right) = 23$, which is the parameter characterizing crossover to superparamagnetism for a given measurement frequency. It is also convenient to rewrite Eq. 5.10 in the following form:

$$\left(1 - \frac{H_0}{H_k}\right)^2 = \frac{H_T}{H_k} \tag{5.11}$$

where we have introduced an effective "thermal" field H_T:

$$H_T \equiv \frac{2\widetilde{\Delta} k_B T}{M_s V} = 46 \frac{k_B T}{M_s V} \tag{5.12}$$

Solving Eq. 5.11 for H_k, we derive the expression for the uniaxial anisotropy field H_k as a function of the field H_0 obtained from the astrod measurements:

$$H_k = H_0 + \frac{H_T}{2}\left(1 + \sqrt{1 + 4\frac{H_0}{H_T}}\right) \tag{5.13}$$

Eq. 5.13 is the main result. Eq. 5.13 and Eq. 5.12 allow one to obtain the value of the uniaxial anisotropy of the nanomagnet from finite temperature astroid measurements.

The distance between the center of the astroid and one of the points on the hard axis direction is the anisotropy field for the given temperature. In addition, the area of the astroid is related

to this length by a simple expression:

$$H_k = \sqrt{\frac{8A}{3\pi}}. \tag{5.14}$$

Therefore, if we measure the Stoner-Wohlfarth astroid as a function of temperature, we can extract for each temperature an anisotropy field through the calculated area of the astroid. The experiment is carried out in a liquid helium cryostat from Cryo Industries of America. The sample is held in a custom-designed sample holder with four microwave ports (a 4-port sample holder as seen in Figure 5.2) and connected through microwave cables to a digital multimeter (Keithley Model 2400). The sample is inserted into the cryostat, and a GMW electromagnet is placed around the cold finger of the cryostat to apply the external magnetic field. The electromagnet is free to rotate on a platform that also marks the angle of the applied field.

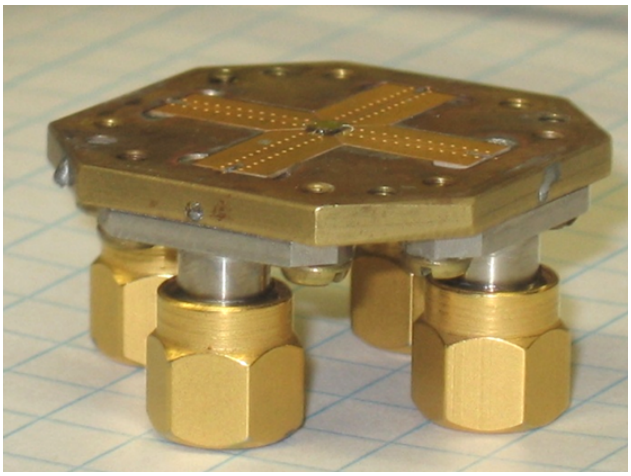

Figure 5.2: **Nonlinear Gain.** The parametric amplifier shows nonlinear gain as a function of drive amplitude, as shown in earlier simulations (Figure 4.11).

The measurement is carried out by first stabilizing the temperature of the sample. Depending on the setpoint temperature, this can take a few minutes (4 K) to more than an hour (closer to room temperature). Once the temperature is stabilized, the sample is measured by taking resistance versus field loops at a given field angle (see Figure 5.3). Care is taken to map the

astroid as best we can with 5-degree steps, with additional angles in between to map the corners of the astroid. The switching fields are recorded for the switches between low and high resistances and are then plotted as a function of angle in a 2-D plot, which gives us the experimentally measured astroid as shown in Figure 5.4.

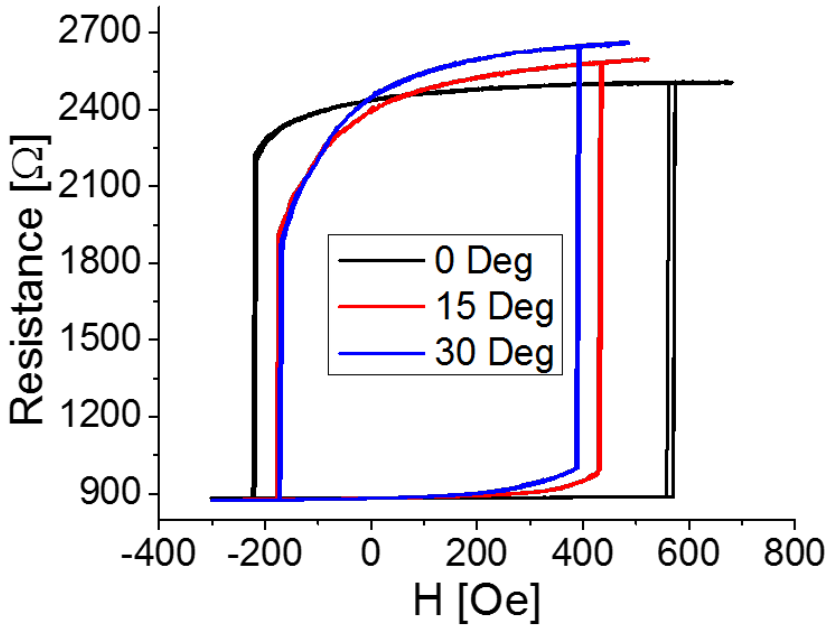

Figure 5.3: **Example R(H) Measurements.** Resistance vs external field is measured at different in-plane angles of applied field. Switching fields are part of the astroid curve for the nanomagnet.

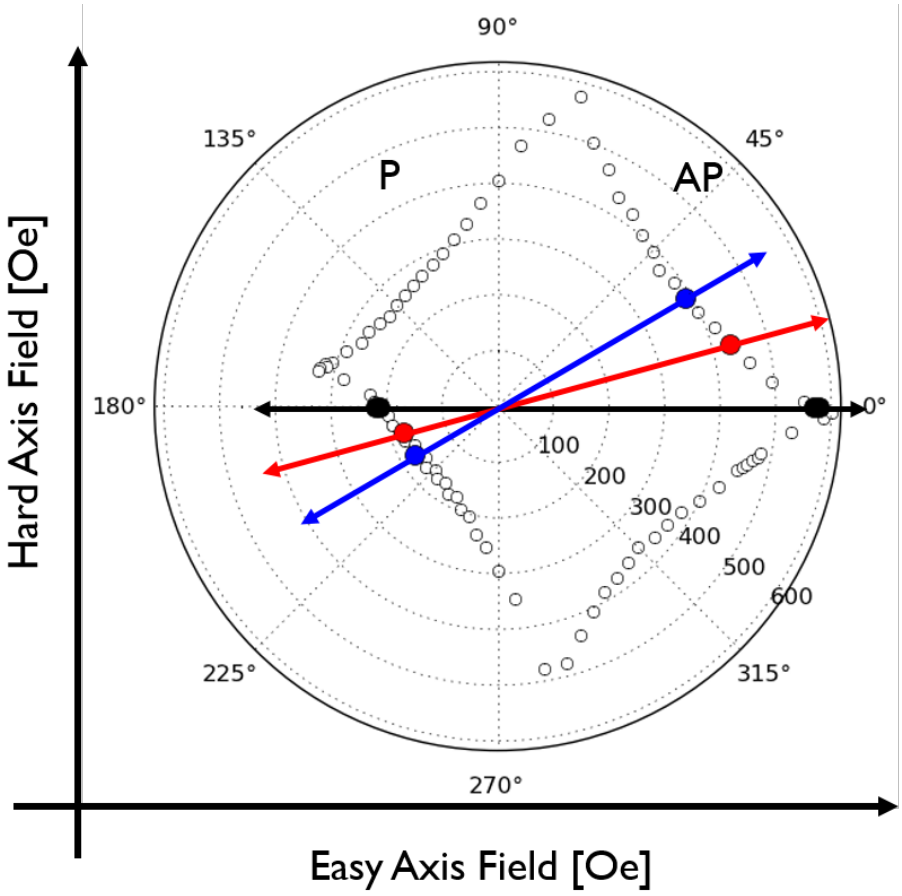

Figure 5.4: **Example Astroid Plot.** When plotting the switching fields on a 2D plot, one can see the astroid shape of the curve. Different colors correspond to the R(H) loops measured in Figure 5.3.

The astroids are measured at several different temperatures, as shown in Figure 5.5. From these experimentally measured astroids, a numerical calculation of the astroid's area is done via a Python code and Equation 5.14 is used to extract the switching fields.

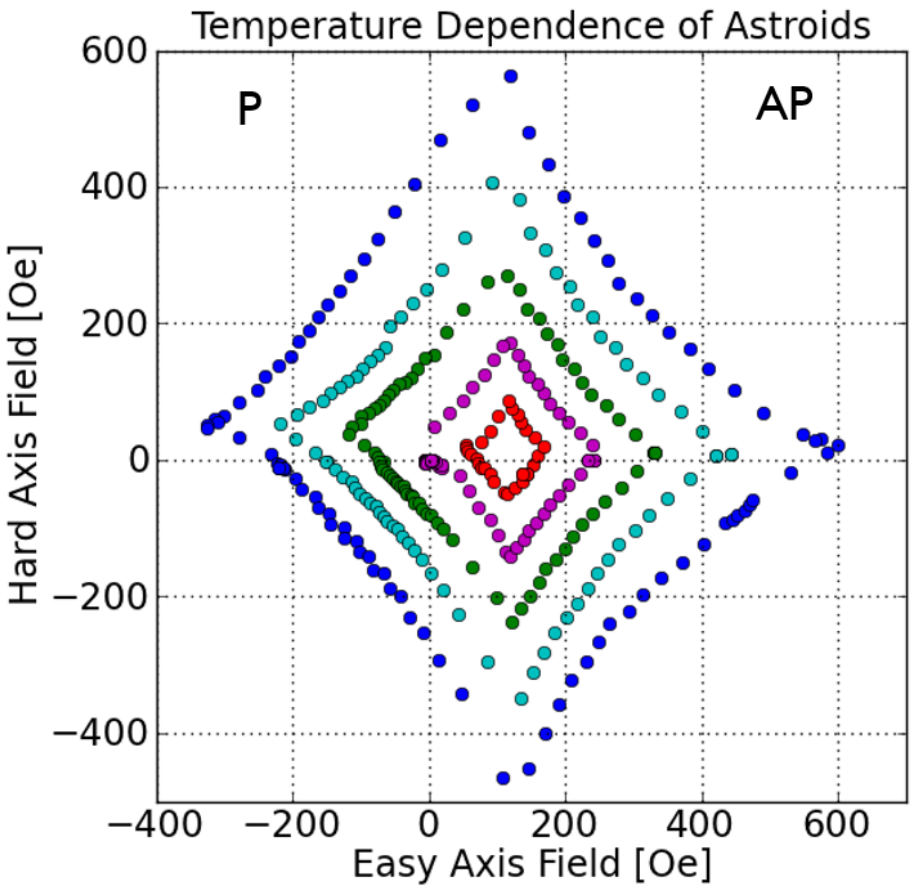

Figure 5.5: **2D Plot of Astroid Temperature Dependence.** 2D plots of astroids for the same device taken at different temperatures, corresponding to the colors indicated.

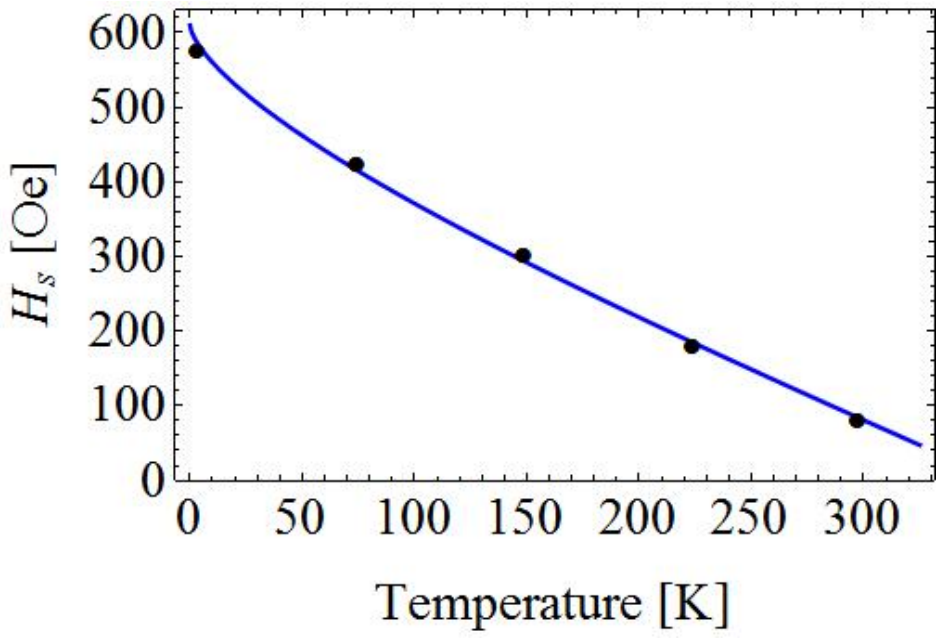

Figure 5.6: **Switching Fields vs. Temperature.** Switching fields extracted from the calculated area of each astroid and plotted as a function of temperature.

Once the switching fields are plotted as a function of temperature as shown in Figure 5.6, we can use our model to extract the zero-temperature anisotropy field.

$$t = \tau_0 \exp\left[\frac{E_b(H_{HA})}{k_B T}\right] \tag{5.15}$$

$$E_b = k_B T \Delta \left(1 - \frac{H}{H_k}\right)^n \tag{5.16}$$

For the case of pure macrospin, n = 2 as derived earlier. However, to account for multiple degrees of freedom from some micromagnetic structure, we instead use n = 3/2 [42].

$$E_b = k_B T \Delta \left(1 - \frac{H}{H_k}\right)^{3/2} \tag{5.17}$$

$$k_B T \Delta \left(1 - \frac{H_0}{H_k}\right)^{3/2} = k_B T \ln\left(\frac{t_s}{\tau_0}\right) \tag{5.18}$$

$$\left(1 - \frac{H}{H_k}\right)^{3/2} = \frac{\widetilde{\Delta}}{\Delta} = \frac{H_T}{H_k} \tag{5.19}$$

where $H_T = \frac{2\widetilde{\Delta} k_B T}{M_s V}$.

$$H_s = H_k \left(1 - \left(\frac{H_T}{H_k}\right)^{2/3}\right) \tag{5.20}$$

$$H_k(T) = H_k(0) \frac{M_s(T)}{M_s(0)} \tag{5.21}$$

With sufficient data for the fit, one can then calculate the expected thermal stability parameter for any given temperature. However, Equation 5.21 does require knowledge of the temperature dependence of the saturation magnetization M_s. Our collaborators at UCLA in the DARPA STT-RAM program were able to measure the thin films corresponding to the free layer magnetization in these magnetic tunnel junctions. Figure 5.7 shows the temperature dependence of M_s with respect to temperature, which fits the Bloch 3/2 law pretty well in the temperature range where we can operate the cryostat.

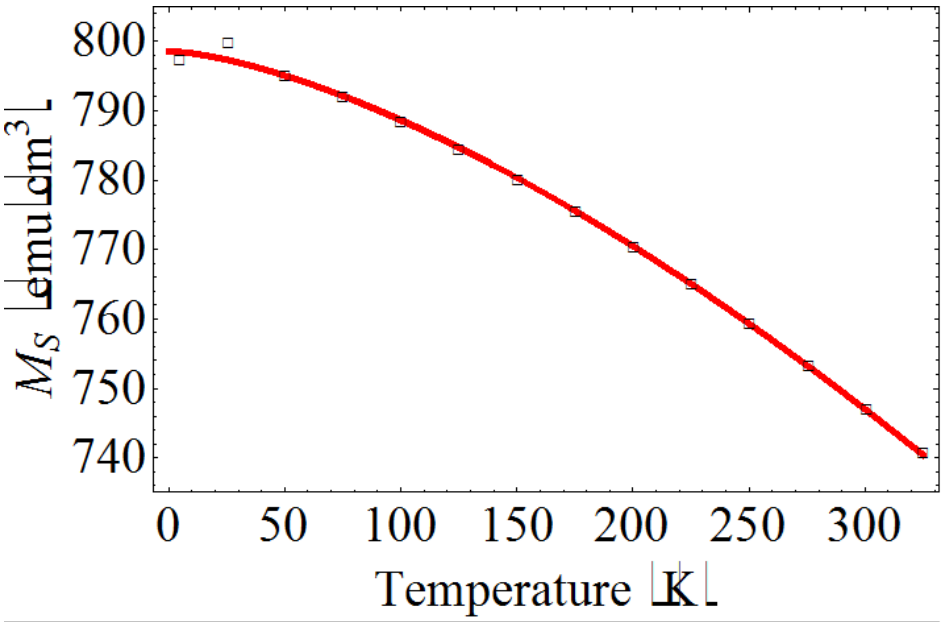

Figure 5.7: **Saturation Magnetization and Bloch Law.** Saturation magnetization of the film corresponding to the free layer material. The dependence on temperature agrees well with the Bloch 3/2 law (red curve).

In addition, measurements were also made of the Stoner-Wohlfarth astroid curve while under the effects of DC bias voltage. These measurements reveal the effects of spin transfer torque on the quasi-static switching of the nanomagnet. The effect of the STT is to pull the magnetization towards the direction of spin polarization, which changes sign upon the reversal of voltage polarity. The net effect is a favoring of the parallel or anti-parallel state of the MTJ, and this is reflected in a shrinking of only one side of the astroid. One minimum of the energy gets excited more readily by STT and thermal fluctuations are enhanced. The other state remains relatively unchanged.

5.3 Comparison with Random Telegraph Noise

One way to verify the calculated values is to compare the calculated thermal stability parameter to an experimentally measured thermal stability. The experimentally measured

quantities are be the actual lifetimes of the magnetic states as measured in random telegraph noise measurements. The measurements were done on the same sample and in the same measurement setup. For a given temperature, the centroid of the astroid was calculated numerically from the measured astroid and the external field was configured to match those coordinates in the $H_x - H_y$ plane.

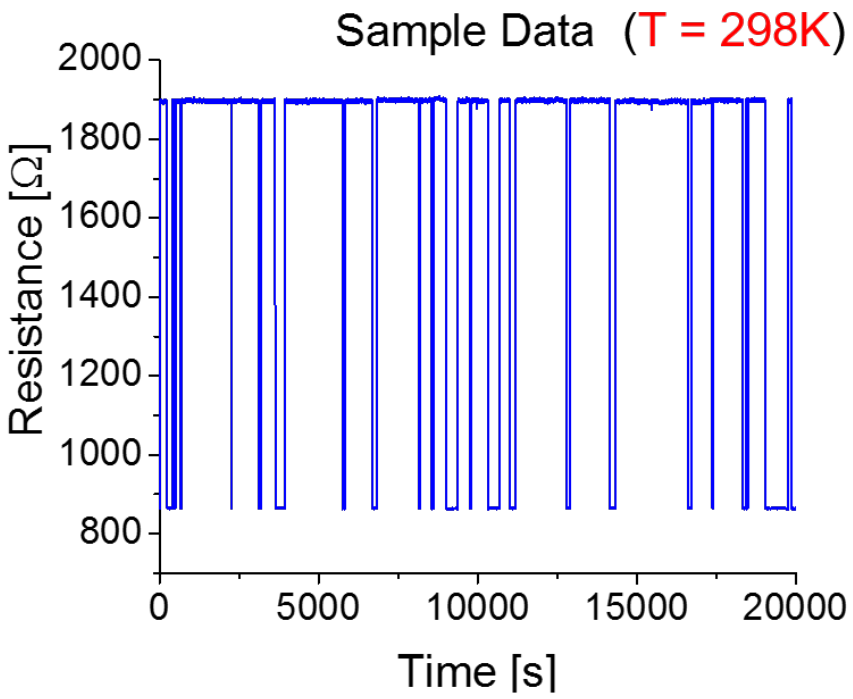

Figure 5.8: **Example Telegraph Data.** Resistance versus time data for the device while the magnetic field is held at the centroid of the astroid, where dwell times should be equal for the P and AP state.

The sample's resistance versus time is then measured using the Keithley multimeter, as shown in the example data in Figure 5.8. Ideally, the sample chosen for this should be a superparamagnetic sample at room temperature or lower. Then, a sufficient number of switches between the parallel and anti-parallel states can be measured and the lifetime of the states recorded. With the field set at the centroid of the astroid, the lifetimes of the parallel and anti-parallel states are expected to be equal. This is then a direct measurement of the thermal stability of the sample.

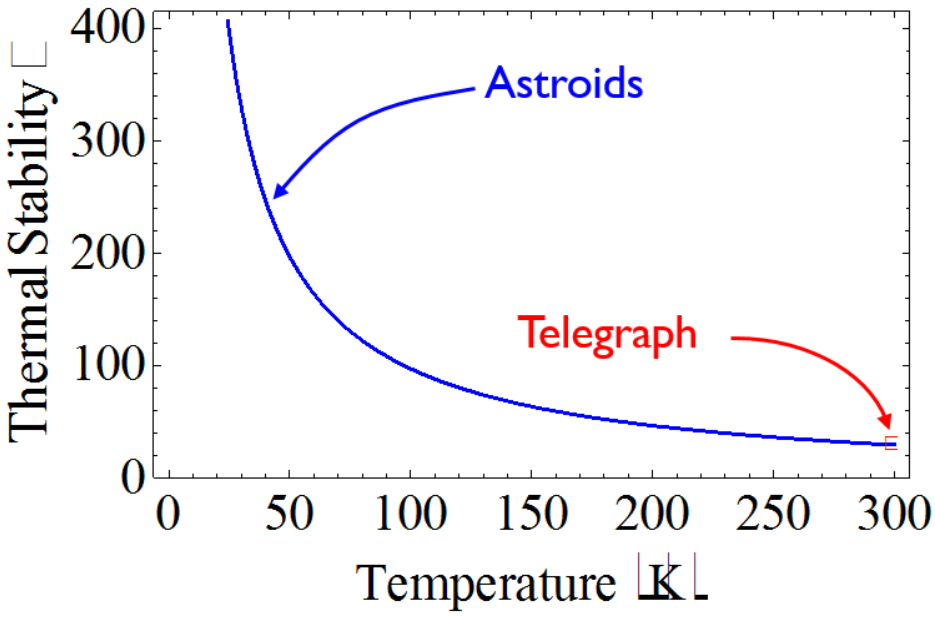

Figure 5.9: **Thermal Stability From Astroids vs. Telegraph.** (blue) Calculated thermal stability from anisotropy fields extracted in astroid measurements. (red) Point indicates thermal stability extracted from telegraph noise measurements.

In order to extract the lifetimes of each state, a Poisson distribution is used to create histograms of the dwell times. The Poisson distribution is appropriate, because the switching is a random process with two states. The dwell time is then extracted from the fit of the decaying exponential to the histogram. Figure 5.9 shows the comparison of astroid measurements to the telegraph noise measurement for extracting the thermal stability information. From the random telegraph noise measurements, the thermal stability parameter is found to be 29.3 on average. This value agrees well with the astroid measurements which calculate the thermal stability parameter at 298 K to be 29.2.

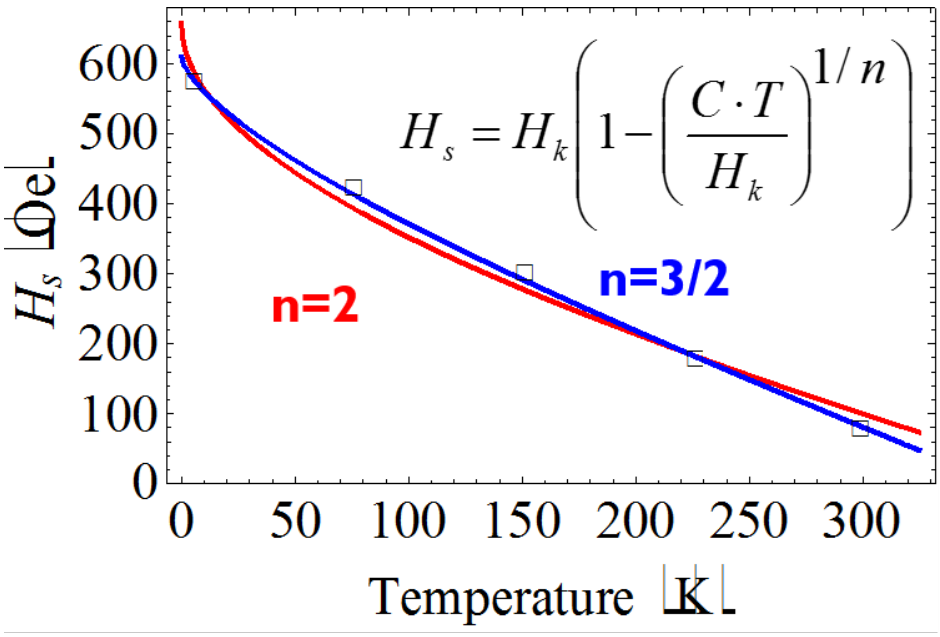

Figure 5.10: **Choice of Exponent on Fit.** Fits of the switching fields as a function of temperature with different choice of exponent.

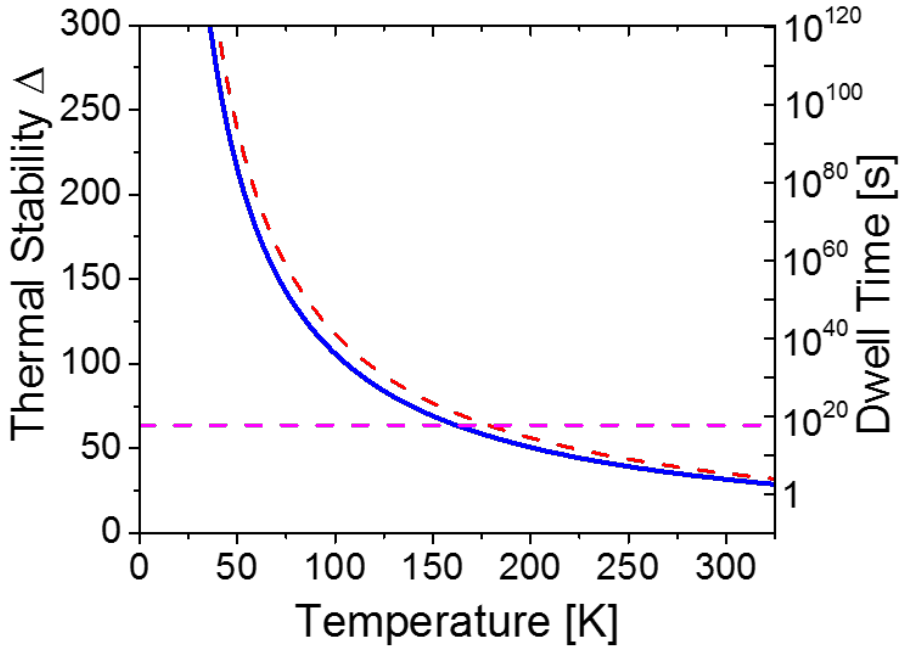

Figure 5.11: **Choice of Exponent on Dwell Times.** Corresponding calculated dwell times from parameters extracted in fitting with different exponents chosen in Figure 5.10.

One could ask whether choosing different energy barrier exponents can have a strong impact on the measured thermal stability. As shown in Figure 5.10, the exponent does make a difference in the fitting procedure. This can also be seen in the corresponding dwell times, included in Figure 5.11. However, the choice of exponent must be matched to experimental conditions and will depend on the mode of switching. In our fitting, the exponent n = 3/2 yielded a thermal stability parameter closer to the telegraph noise measurement than an exponent of n = 2. The difference between n = 2 and n = 3/2 is also slight in our case, which indicates that the free layer is most likely a nearly uniform nanomagnet but with some micromagnetic curvature due to stray fields.

Chapter 6

Conclusion

In summary, this work has shown that magneto-electric coupling can be used to excite parametric resonance of magnetization by electric field. We employed voltage-controlled magnetic anisotropy at the CoFeB/MgO interface to excite parametric oscillations of a CoFeB free layer magnetization in nanoscale magnetic tunnel junctions. The threshold voltage for parametric excitation in this system is found to be well below 1 Volt, which is attractive for applications in energy-efficient spintronic and magnonic nanodevices such as spin wave logic [36]. This work opens a new route for excitation of magnetization dynamics in thin films of metallic ferromagnets and nanodevices based on magnetic multilayers.

In addition, parametric excitation of magnetization is a versatile method for generating short-wavelength spin waves [17]. Part of this work was to develop nanowire devices based on those proposed in [17], using ferromagnetic metals in a nanowire geometry with contacts that utilize VCMA to generate and manipulate propagating spin waves. Preliminary data shows that our device design can work and does, indeed, show voltage control of spin wave propagation.

Future work for these spin wave devices involves experimentally demonstrating that each part of the spin wave logic based on the majority logic gate can be achieved. So far, we have demonstrated the ability to generate spin waves parametrically in a nanomagnet. We also found evidence that we can control propagation of spin waves using VCMA in a nanowire structure. The next goals to achieve are: (1) demonstration of parametric generation of spin waves in a nanowire structure, (2) demonstration of phase control of spin waves, and (3) demonstration of parametric amplification and phase correction of spin waves. The final product will eventually be a fully functional majority logic gate with elements to amplify and control spin wave propagation by VCMA. Such a device would probably take at least a couple of few years to develop, since the device design and fabrication can be quite challenging.

Bibliography

[1] Slonczewski, J. C. Conductance and exchange coupling of two ferromagnets separated by a tunneling barrier. *Phys. Rev. B* **39**, 6995 (1989).

[2] Slonczewski, J. C. Current-driven excitation of magnetic multilayers. *J. Magn. Magn. Mater.* **159**, L1 (1996).

[3] Berger, L. Emission of spin waves by a magnetic multilayer traversed by a current. *Phys. Rev. B* **54**, 9353 (1996).

[4] Gurevich, A. G., & Melkov, G. A. *Magnetization Oscillations and Waves* (CRC, 1996).

[5] L'vov, V. S. *Wave Turbulence Under Parametric Excitation* (Springer, 1994).

[6] O'Handley, R. C. *Modern Magnetic Materials Principles and Applications* (John Wiley and Sons, 2000).

[7] Pozar, D. M. *Microwave Engineering* (Wiley, 2004).

[8] Brown, W. F., Jr. *Micromagnetics* (Wiley, 1963).

[9] Ralph, D. and Stiles, M. Spin transfer torques. *J. Magn. Magn. Mater.* **320**, 1190 (2008).

[10] Butler, W. H. *et al.* Spin-dependent tunneling conductance of Fe—Mgo—Fe sandwiches. *Phys. Rev. B* **63** 054416 (2001).

[11] Julliere, M. Tunneling between ferromagnetic films. *Physics Letters A* **54**, 225 (1975).

[12] Kiselev, S. I. *et al.* Microwave oscillations of a nanomagnet driven by a spin-polarized current. *Nature* **425**, 380 (2003).

[13] Matsukura, F., Tokura, Y., & Ohno, H. Control of magnetism by electric fields. *Nature Nanotech.* **10**, 209-220 (2015).

[14] Shiota, Y. *et al.* Induction of coherent magnetization switching in a few atomic layers of FeCo using voltage pulses. *Nature Mater.* **11**, 3943 (2012).

[15] Nozaki, T. *et al.* Electric-field-induced ferromagnetic resonance excitation in an ultrathin ferromagnetic metal layer. *Nature Phys.* **8**, 491496 (2012).

[16] Zhu, J. *et al.* Voltage-induced ferromagnetic resonance in magnetic tunnel junctions. *Phys. Rev. Lett.* **108**, 197203 (2012).

[17] Verba, R., Tiberkevich, V., Krivorotov, I. N. & Slavin, A. Parametric excitation of spin waves by voltage-controlled magnetic anisotropy. *Phys. Rev. Applied* **1**, 044006 (2014).

[18] Fiebig, M. Revival of the magnetoelectric effect. *J. Phys. D* **38**, R123 (2005).

[19] Chumak, A. V. Vasyuchka, V. I., Serga, A. A., Kostylev, M. P., Tiberkevich, V. S., & Hillebrands, B. Storage-recovery phenomenon in magnonic crystal. *Phys. Rev. Lett.* **108**, 257207 (2012).

[20] Kruglyak, V. V., Demokritov, S. O., & Grundler, D. Magnon spintronics. *J. Phys. D* **43**, 264001 (2010).

[21] Chumak, A. V., Vasyuchka, V. I., Serga, A. A., & Hillebrands, B. Magnon spintronics. *Nature Phys.* **11**, 453461 (2015).

[22] Urazhdin, S., Tiberkevich, V., & Slavin, A. N. Parametric excitation of a magnetic nanocontact by a microwave field. *Phys. Rev. Lett.* **105** 237204 (2010).

[23] Melkov, G. A., Yu, V., Kobljanskyj, A. A., Serga, A. S., Tiberkevich, V. S., & Slavin, A. N. Reversal of Momentum Relaxation. *Phys. Rev. Lett.* **86**, 4918 (2001).

[24] Weisheit, M., Fhler, S., Marty, A., Souche, Y., Poinsignon, C., & Givord, D. Electric field-induced modification of magnetism in thin-film ferromagnets. *Science* **315**, 349 (2007).

[25] Chiba, D. *et al.* Magnetization vector manipulation by electric fields. *Nature* **455**, 515518 (2008).

[26] Maruyama, T. *et al.* Large voltage-induced magnetic anisotropy change in a few atomic layers of iron. *Nature Nanotech.* **4**, 158161 (2009).

[27] Endo, M., Kanai, S., Ikeda, S., Matsukura, F., & Ohno, H. Electric-field effects on thickness dependent magnetic anisotropy of sputtered MgO/Co40Fe40B20/Ta structures. *Appl. Phys. Lett.* **96**, 212503 (2010).

[28] Duan, C.-G. *et al.* Surface magnetoelectric effect in ferromagnetic metal films, *Phys. Rev. Lett.* **101**, 137201 (2008).

[29] Niranjan, M. K., Duan, C.-G., Jaswal, S. S., & Tsymbal, E. Y. Electric field effect on magnetization at the Fe/MgO(001) interface. *Appl. Phys. Lett.* **96**, 222504 (2010).

[30] Amiri, P. K. & Wang, K. L. Voltage-controlled magnetic anisotropy in spintronic devices. *SPIN* **02**, 1240002 (2012).

[31] Tulapurkar, A. A. *et al.* Spin-torque diode effect in magnetic tunnel junctions. *Nature* **438**, 339342 (2005).

[32] Sankey, J. C. *et al.* Spin-transfer-driven ferromagnetic resonance of individual nanomagnets. *Phys. Rev. Lett.* **96**, 227601 (2006).

[33] Wang, C. *et al.* Bias and angular dependence of spin-transfer torque in magnetic tunnel junctions. *Phys. Rev. B* **79**, 224416 (2009).

[34] Bortolotti, P. *et al.* Parametric excitation of magnetic vortex gyrations in spin-torque nano-oscillators. *Phys. Rev. B* **88**, 174417 (2013).

[35] Gonçalves, A. M. *et al.* Spin torque ferromagnetic resonance with magnetic field modulation. *Appl. Phys. Lett.* **107**, 172406 (2013).

[36] Khitun, A., Bao, M. & Wang, K. L. Magnonic logic circuits. *J. Phys. D* **43**, 264005 (2010).

[37] Vansteenkiste, A. *et al.* The design and verification of MuMax3. *AIP Adv.* **4**, 107133 (2014).

[38] Verba, R. *et al.* Theory of ground-state switching in an array of magnetic nanodots by application of a short external magnetic field pulse. *Phys. Rev. B* **87**, 134419 (2013).

[39] Beleggia, M. *et al.* Demagnetization factors for elliptic cylinders. *J. Phys. D: Appl. Phys.* **38**, 3333 (2005).

[40] Donahue, M. J. & Porter, D. G. OOMMF Users Guide, Version 1.0, Interagency Report NISTIR 6376, National Institute of Standards and Technology, Gaithersburg, MD (1999).

[41] McMichael, R. D. & Stiles, M. D. Magnetic normal modes of nanoelements. *J. Appl. Phys.* **97**, 10J901 (2005)

[42] Victora, R. H. Predicted time dependence of the switching field for magnetic materials. *Phys. Rev. Lett.* **63**, 457 (1989).

[43] Khitun, A. & Wang, K. L. Non-volatile magnonic logic circuits engineering. *J. Appl. Phys.* **110**, 034306 (2011).

[44] Upadhyaya, P. *et al.* Thermal stability characterization of magnetic tunnel junctions using hard-axis magnetoresistance measurements. *J. Appl. Phys.* **109**, 07C708 (2011).

[45] Heindl, R. *et al.* Validity of the thermal activation model for spin-transfer torque switching in magnetic tunnel junctions. *J. Appl. Phys.* **109**, 073910 (2011).

[46] Klingler, S. *et al.* Spin-wave logic devices based on isotropic forward volume magnetostatic waves. *Appl. Phys. Lett.* **106**, 212406 (2015).

[47] Nowak, J. J. *et al.* Dependence of Voltage and Size on Write Error Rates in Spin-Transfer Torque Magnetic Random-Access Memory. *IEEE Magn. Lett.* **7**, 1-4 (2016).

Appendices

A Estimation of Microwave Amplitude with Impedance Mismatch

Our microwave generators level the output microwave power according to an assumed $50\,\Omega$ load impedance. Since our sample impedances are usually not $50\,\Omega$, we need to estimate the amplitude of applied microwave voltage or current by modeling the circuit. Typically, the circuit can be modeled as a simple voltage divider with the generator's internal $50\,\Omega$ impedance as one of the impedances while the load impedance is the other.

One can then calculate the power delivered to the sample as:

$$P_L = (1 - \Gamma^2)P_g \tag{A.1}$$

where P_L is the root mean square (rms) power delivered to the sample/load, P_g is the rms power sourced by the generator, and Γ is the voltage reflection coefficient for a microwave transmission line. The reflection coefficient quantifies the amount of voltage that is reflected from a mismatched load impedance that terminates a transmission line. It is defined as:

$$\Gamma = \frac{Z_L - Z_0}{Z_L + Z_0} \tag{A.2}$$

where Z_0 is the impedance of the transmission line (typically $50\,\Omega$) and Z_L is the load impedance. At matched impedance, there is no reflection and the coefficient is zero. At zero impedance (terminated with a short) or at infinite impedance (terminated with an open circuit), all of the power should be reflected and the coefficient is ± 1 (a negative sign indicates a phase shift of π or 180° in the reflected wave). [7]

One can then substitute the reflection coefficient into the expression for power delivered to the sample and calculate the current or voltage at the sample. In either case, the factor $(1 - \Gamma^2)$ is required:

$$1 - \Gamma^2 = 1 - \left(\frac{Z_L - Z_0}{Z_L + Z_0}\right)^2 \tag{A.3}$$

$$= \frac{(Z_L + Z_0)^2}{(Z_L + Z_0)^2} - \frac{(Z_L - Z_0)^2}{(Z_L + Z_0)^2} = \frac{4Z_0 Z_L}{(Z_L + Z_0)^2}. \tag{A.4}$$

For the current, one obtains:

$$P_L = I_L^2 Z_L = \frac{4Z_0 Z_L}{(Z_L + Z_0)^2} P_g \tag{A.5}$$

$$I_L(\text{rms}) = \sqrt{\frac{4Z_0}{(Z_L + Z_0)^2} P_g} \tag{A.6}$$

which gives current in units of Amps for impedances given in Ohms and power given in Watts.

For the voltage, one obtains:

$$P_L = \frac{V_L^2}{Z_L} = \frac{4Z_0 Z_L}{(Z_L + Z_0)^2} P_g \tag{A.7}$$

$$V_L(\text{rms}) = \sqrt{\frac{4Z_0 Z_L^2}{(Z_L + Z_0)^2} P_g} \tag{A.8}$$

which gives voltage in units of Volts for impedances given in Ohms and power given in Watts.

Often, we work with the microwave power in units of dBm, which is power output in units of decibels relative to 1 mW as a reference. The conversion to Watts is therefore:

$$P_g[W] = 0.001W \times 10^{P_g[dBm]/10}. \tag{A.9}$$

Keep in mind that the rms value is different from the amplitude of the output wave by a factor of $\sqrt{2}$, so the above equations become:

$$I_L(\text{amplitude}) = \sqrt{2} I_L(\text{rms}) = \sqrt{\frac{8Z_0}{(Z_L + Z_0)^2} \times 0.001W \times 10^{P_g[dBm]/10}} \tag{A.10}$$

$$V_L(\text{amplitude}) = \sqrt{2} V_L(\text{rms}) = \sqrt{\frac{8Z_0 Z_L^2}{(Z_L + Z_0)^2} \times 0.001W \times 10^{P_g[dBm]/10}} \tag{A.11}$$

which we generally use when calculation of the microwave current or voltage becomes important for the experiment.

We can examine the microwave and current amplitudes as a function of sample impedance. This is important to consider especially in the case of magnetic tunnel junctions, where large changes in the magnetoresistance can occur when microwave voltage is applied to the sample. One finds that

$$I_L(\text{amplitude}) \propto \frac{1}{Z_L + Z_0} \tag{A.12}$$

$$V_L(\text{amplitude}) \propto \frac{Z_L}{Z_L + Z_0} \tag{A.13}$$

Expanding the voltage term, one obtains

$$\frac{Z_L}{Z_L + Z_0} = \frac{1}{1 + Z_0/Z_L} = \sum_{n=0}^{\infty} (-1)^n \left(\frac{Z_0}{Z_L}\right)^n \tag{A.14}$$

Note that above a certain value of the impedance ($Z_L \gtrsim 1000\,\Omega$), the microwave voltage does not vary much (<5%) as a function of sample impedance. The current, however, can change greatly as a function of sample impedance.

B Microwave Probes and Positioners

When handling the Cascade Microtech probe positioners and associated microwave probes, there are some guidelines and procedures to keep in mind that will help prevent damage to the probes and facilitate a longer probe lifetime.

B.1 Probe Handling and Maneuvering

Continuous use of the probes will degrade them due to wear and tear, and they will eventually need to be sent for repairs or replacement.

1. When handling the entire probe positioner and moving it, be sure to raise the vertical axis (z-axis) control to the highest setting (away from the base of the positioner) so that the probe has the highest clearance from the stage surface. This minimizes the chance that the probe will make contact with the stage when lifting or dropping the positioner into place.

2. Hold the probe positioner with two hands when moving the entire positioner: one on the base and one on the arm. Be sure to keep a firm grip, and hold the positioner with the arm tilted upward (probe side up) when possible. This tends to be safest for the probe when putting the base into position.

3. When moving the entire probe positioner, usually for coarse alignment or installing the probes, be sure to release the vacuum base and lift the *entire* probe positioner off

the base for large adjustments in position. Sliding the rubber gasket on the stage will wear out the gasket and result in poorer vacuum seals.

4. To ensure a good seal with the vacuum gasket, be sure to clean the base of the probe positioner from time to time with water. Do NOT use alcohol, or other solvents, or the rubber will be degraded very quickly.

B.2 Probe Installation and Removal

Installation of a picoprobe (especially microwave probes) should be done carefully and slowly. It is better to take more time to properly install a probe than to make a quick mistake and damage it.

1. When installing the picoprobes, be sure to keep the vertical axis (z-axis) control raised to the highest point so that the probe mount is raised well above any surfaces.

2. The positioner should be placed on a flat surface and kept still by the vacuum gasket on the base of the positioner. If the surface is not smooth or continuous enough to hold a good seal, find a better surface.

3. On a typical probe station stage, the positioner should be turned so that there is sufficient room to perform the installation. This can typically be best accomplished by angling the positioner with respect to the stage direction so the arm is extended into the air with nothing beneath the probe mount. Be sure that the vacuum seal with the stage is sturdy and robust, because this precarious position of the probe arm can easily break an expensive probe if the seal fails and the arm swings into contact with something solid (like the stage).

4. The picoprobes are mounted to the positioner's probe arm by two hex screws on either side of the probe mount. The screws are adjustable by a hex key, and the typical size

in imperial units is a 9/64" key. The center post on the probe mount provides some stability along with the step-like design of the probe assembly.

5. The most delicate part of installing the probe is the moment of transfer from box to positioner (or vice versa), when dropping the probe or losing stability can result in irreparable damage. It's best to hold the sides and back the flap with the mounting holes of the probe with a firm grip and to transfer the probe as quickly as possible.

6. The probe should be taken out of its storage box carefully and placed on the positioner's probe mount after the hex screws have been removed. Keep one hand on the probe, and place at least one screw in the mount and sufficiently tighten it to stabilize the probe before letting go.

7. Secure the hex screws so that the probe is secure and there is no play between the separate parts. The probe should move with the arm as a single piece, controlled by the positioner settings.

8. Clean the probe's microwave connector with a small cotton swab applicator (the type with a thin tip) and isopropanol. Then connect a microwave cable to the connector, with its connector also cleaned before making the connection.

9. Secure the body of the microwave cable to the positioner with the positioner's side holder. To avoid pinching the microwave cable upon tightening, a small piece of foam can be inserted around the cable before securing the cable. The screw should be tightened enough so that there is ideally no movement of the cable when the arm is manipulated by the positioner. Try to ensure that any movement of the microwave cable does not cause movement of the probe (this is best checked with the stage optics viewing the probe while testing cable movement).

B.3 Probe Planarization

After installation of the probe, there may be a need to align the plane of the probes to the sample, or "planarize". For this procedure, the Contact Substrate that was shipped with some of the picoprobes will be required.

1. Place the substrate on the sample stage and position the manipulator so that the probe is over the gold surface. Using the microscope, approach the surface of the substrate and land the probe. Unlike normal hard substrates, the gold contact substrate is soft and gives under pressure from the probes.

2. Use the vertical (z-axis) controls to drive the probe further into the substrate to "dig" trenches in the substrate. Do NOT go too far. It is enough to make a back and forth motion with the vertical control to dig into the substrate and leave marks visible on the microscope screen.

3. Use the vertical control to lift the probe sufficiently far from the surface so that tilting the probe side to side will not result in unwanted contact with the surface. Beginners should err on the side of retracting farther than needed (even fully retracted to be completely safe). Then, use the x- and y-axis controls to reveal the trench marks made by the digging of the probe, if any are visible.

4. Observe the depth of the marks and determine which of the (up to) three probe contact points dig furthest. This part can be tricky, because the depth might be hard to see and can require angling the light source or camera slightly to better view the indentations.

5. Once the depths can be determined, the arm's rotational control (rotating about the x-axis) should be adjusted to compensate for any tilt in the plane defined by the probe's contact points.

6. Land the probe again and dig the contacts into the substrate to verify that they are properly aligned. Ideally, the two side leaves (on GSG probes) should make contact with the surface first. Then the center wire should make contact. However, be aware that the center wire is shaped differently (thicker and rounder) than the side leaves, so it can make a deeper indentation in the substrate than the side leaves.

7. Repeat planar adjustments (Steps 2-5) as many times as necessary to achieve proper alignment of the probe in the x-y plane.

Proper determination of planarization is mostly developed through experience. The process is usually iterative, and it can take several attempts to properly planarize the probe. After the procedure is completed, retract the probe entirely and remove the gold substrate for future use.

B.4 Probe Cleaning

From time to time, the quality of electrical probe contact can degrade through regular use. Often, this is due to accumulated dirt on the probe, and the probe requires cleaning and reinstallation. Unfortunately, the probe does wear down and flex over time, and eventually it requires being sent to the manufacturer for repairs or replacement. Visual inspection can immediately signal the need for cleaning or repairs. The following describes a procedure for safely inspecting the probe contacts.

1. Remove the screw and rubber washer holding the probe in its storage box.

2. Carefully remove the probe, flip it upside down, and place it into its holding post. If possible, it's best to place the probe into an empty probe storage box.

3. Secure the probe in place with the screw and rubber washer. During this process, the screw cannot be wound tightly and flush with the probe's mounting flap. Instead, the probe can be secured by tilting with respect to the storage box ledge. Thus, care must be taken to tighten the screw enough so that the probe no longer moves.

4. Place the storage box under a microscope to inspect the probe prongs, and zoom in to focus on the main contact points of the probe (the three prongs and a part of the body of the probe). The standard telescope lenses used for probe stations tend to work well. They provide sufficient zoom to view the probe for inspection and cleaning.

5. Modify a cotton swab tip by manually pulling at the cotton to fray the end and leave extended tendrils of cotton. Apply some isopropanol to the cotton to wet it, and shake the swab to remove excess liquid. Hold the swab with two hands for increased stability.

6. Clean the probe using the modified cotton swab by aligning the cotton tendrils with the probe prongs and gently sweeping the swab back and forth in a length-wise direction while having some small component of up and down motion. Allow the tendrils move between the prongs and over the contact surfaces akin to "flossing" the probe prongs.

7. Repeat the cleaning a with a few swabs as needed, inspecting the probe between cleanings.

Often, it's unclear whether there has been any visual change after cleaning the probe surfaces, but electrical contacts made with the probe should be improved after cleaning. If electrical contact remains poor, and the quality of contacted surface (usually sample leads) is ruled out as a contributing factor, then the probe may be too dirty for in-house cleaning or worn down from continued use. In that case, it's necessary to send the probe to the manufacturer for their inspection and possible repair. Typically, a probe can last 6 months to 1 year, depending on several factors including: the number of contacts made, the surfaces contacted, and the handling of the user.

C Python Codes for Parametric Resonance

Listed here are the main Python codes developed during the parametric resonance experiment for measuring as well as for the data analysis. They serve as a reference for future developments and projects. Currently, included are the main measurement script and the background subtraction script. Other Python codes were used for trace averaging, calculation of integrated power, extraction of the peak power at each microwave drive amplitude and frequency, as well as the simultaneous fitting of the threshold. They are not included here for brevity.

C.1 spectrumAnalyzer_PR_drive.py

This was the main measurement script that controlled the instruments.

```
1  import os
2  import visa
3  import time
4  import datetime
5  import numpy as np
6  import math
7  import pyqtgraph as pg

8  import msvcrt
9  import pickle
10 from msvcrt import getch
11 from msvcrt import kbhit
12 from pyqtgraph.Qt import QtGui, QtCore

13 from calibFile import *
14 from equipFunc import *
15 from powerFlatness2 import *

16 ###################################################
17 maxH = 1.0 #kG
```

```
18 waitH = 0.4
19 dataAvg = 30
20 Hmod = 0.0 #3.779
21 Idc = 20.0   #-40.0    *1e-6
22 Vdc = 100.0 # mV
23 pwr = -2.0

24 waitMW = 1.0

25 #path = 'Micron-7-Die51-Mod53-05'
26 path = '6.4.2-6R-C16-R03'
27 path = path + '_SA'
28 if not os.path.isdir(path):
29     os.makedirs(path)

30 #fnCom = '_AMod'
31 fnCom = ''
32 ######################################################



33 ##### This is the main program #####
34 def main():
35     global startTime, endTime, Htrack, Htrack_kG, waitLockin, dataAvg,
   ↪ waitLockin2, mwGen
36     global current, pwr, kG2v, lastCurr, parkH, Idc, Vdc

37     startTime0 = timeNow()
38     connectEquip()
39     mwGen = ag

40     ### init ###
41     print '... Initization: checking intial condition: Field Off, Kly
   ↪ Off, mw Off ...'
42     #klyOFF(kly)

43     print 'MW output is off: ... ', outputOFF(mwGen)
44     time.sleep(waitMW)

45     parkH = 10 #-1.0        #unit of V    -0.6/-0.036 for AP/P state
46     removeField(parkH)
47     ### END: initi ###

48     #==== FREQUENCY =====
49     lowerF = 1.0  # 2.0
```

```
50      upperF = 4.0 # 15.0
51      delFreq = 0.01 # 0.01

52      print '\''Freq::'\'', lowerF, upperF, delFreq
53      time.sleep(3)
54      frqList = np.arange(lowerF, upperF + delFreq, delFreq)

55      #plotx, ploty, plotx2, ploty2 = livePlot_init(frqList)

56      #==== POWER =====
57      #zList = np.arange(8.0, -6.0 - 0.001, -0.5)
58      zList = [-20.0]
59      print '\''z::pwr::'\'', zList
60      time.sleep(3)

61      #==== BIAS:: Vdc =====
62      mList = [Vdc]
63      #mList = np.arange(-21.0, 21.0  +0.0001, +2.0)
64      print '\''m::Vdc::'\'', mList
65      time.sleep(3)
66      '''
67      #==== BIAS:: Idc =====
68      mList = [Idc]
69      #mList = np.arange(-21.0, 21.0  +0.0001, +2.0)
70      print 'm::Idc::', mList
71      time.sleep(3)
72      '''



73      for m in mList:
74          #pwr = z

75          print '\''... Changing field to saturation ...'\''
76          Htrack, Htrack_kG = gotoH_kG(sr7225, -maxH, waitH, '\''downH'\'')

77          for z in zList:
78              pwr = z

79              #Idc = klyIramp(kly, m*1e-6, Idc)
80              #time.sleep(60*0.1)

81              #time.sleep(60*0.1)
82              #Idc = -m
83              #yo_ramp(Idc*1e-6)
```

```
84              print 'MW pwr = ', pwr, ' dBm ', setP(mwGen,
    ↪ pwr+pwr_correction(pwr,lowerF))
85              time.sleep(waitMW)

86              kGrange1 = np.arange(-0.4, 0.5 +0.0001, 0.05)
87              #kGrange1 = np.arange(-0.5, 0.5 +0.0001, 0.1)
88              #kGlist = np.concatenate((kGrange99, kGrange1))
89              kGlist = kGrange1
90              #kGlist = [-0.4]

91              print 'kG::',kGlist
92              time.sleep(2)

93              for j in kGlist:

94                  print '... Changing field to set value ...'
95                  Htrack, Htrack_kG = gotoH_kG(sr7225, j, waitH, 'upH')

96                  #Rval, Vval = klyRes(kly, 20, 0)

97                  startTime = timeNow()
98                  sname = path
99                  fn0 = path + '/'+ str(int(dHMS())-0) + '_' + sname +
    ↪ '_FMR'
100                 fnH1 = '_H('+str(round(j,3))+'kG_'
101                 fnH2 = str(Htrack)+'V)'
102                 fnHmod = '_Hmod('+str(Hmod)+'Vrms)'
103                 fnAvg = '_avg('+str(dataAvg)+')'
104                 fnPwr = '_pwr('+str(pwr)+')'
105                 #fnBias = '_Idc(' + str(Idc) + 'uA)'
106                 fnBias = '_Vdc(' + str(Vdc) + 'mV)'
107                 fnMindex = ''
108                 #fnR =
    ↪ '_R('+str(round(Rval,2))+')_V('+str(round(Vval,4))+')'

109                 filename =  fn0 + fnH1 + fnH2 + fnHmod + fnAvg + fnPwr +
    ↪ fnBias + str() + fnCom + '.txt'
110                 f = open(filename, 'w')
111                 filehead(f,filename)

112                 # set MW freq
113                 falseRead(mwGen, sr7225, lowerF, 'offon') #mw OFF
    ↪ before lowerF is set.. mw ON after lowerF is set and stays ON

114                 for freq in frqList:
```

```
115                     print 'H(', j,'kG):: f = ', freq, ' GHz ',
    ↪ setF(mwGen,freq)
116                     print 'Corrected P =
    ↪ ',pwr+pwr_correction(pwr,freq),'dBm, cal =
    ↪ ',round(pwr,0),'dBm',setP(ag, pwr+pwr_correction(pwr,freq))
117                     time.sleep(waitLockin2) # 5.0 x tc
    ↪ #time.sleep(waitLockin) # 5.0 x tc

118                     # SA MEASUREMENT HERE

119                     # Maybe nanovoltmeter reading here?

120                     #Xval1, Yval1 = measureSRS830(srs830, dataAvg)
    ↪ #phase is fixed to zero, not reading
121                     Xval2, Yval2 = measureLockin(sr7225, dataAvg,
    ↪ lockSEN2)
122                     #Rval, Vval = klyRes(kly, 30, 0)

123                     '''
124                     # Update graph
125                     plotx = np.roll(plotx, -1)
126                     ploty = np.roll(ploty, -1)
127                     plotx[-1] = freq
128                     #ploty[-1] = Xval1
129                     ploty[-1] = Xval2
130                     p1.plot(plotx,ploty, pen = 'g', clear = True)
131                     app.processEvents()

132                     plotx2 = np.roll(plotx2, -1)
133                     ploty2 = np.roll(ploty2, -1)
134                     plotx2[-1] = freq
135                     #ploty2[-1] = Yval1
136                     ploty2[-1] = Yval2
137                     p2.plot(plotx2,ploty2, pen = 'g', clear = True)
138                     app.processEvents()
139                     # END update graph
140                     '''

141                     print >> f, freq, Xval2, Yval2 #, Xval1, Yval1 #,
    ↪ Rval, Vval

142                     if  msvcrt.kbhit() :
143                         z =  msvcrt.getch()
144                         if  z == "q":
145                             print " "
```

```
146                                 print "Setting all equipment to zero"
147                                 print 'mw OFF: ... ', outputOFF(mwGen)
148                                 time.sleep(1)
149                                 removeField(parkH)
150                                 quit()

151                     f.close()
152                     endTime = timeNow()
153                     endTimeInsert(filename, endTime, 3)


154                 ### END: j-Loop ###
155             ### END: m-Loop ###
156         ### END: z-Loop ###

157         ### End of measure routine ###
158         print '\n'
159         print '========= End of Measurement ========='
160         print 'mw OFF: ... ', outputOFF(mwGen)
161         #gotoOSCamp(srs830, 1.2, 0.1, 0.1)
162         #klyIramp(kly, math.copysign(5.0e-6, Idc), Idc)
163         #klyOFF(kly)
164         #yo_ramp(-5.0*1e-6)
165         removeField(parkH)

166         print '====================================='
167         print 'start: ', startTime0
168         print 'end  : ', timeNow()
169         #raw_input()


170 ##### End: main #####


171 ##### Live plot initiate #####
172 def livePlot_init(dataList):
173     global win, app, p1, p2, plotx, ploty, plotx2, ploty2

174     plotLength = len(dataList)
175     nameWindow = 'FMR!'
176     nameTitle1 = 'X-Ch'
177     nameTitle2 = 'Y-Ch'
178     yLabel = 'Lock-in'
179     yUnit = 'V'
180     xLabel = 'f'
```

```
181     xUnit = 'GHz'

182     app = pg.mkQApp()
183     win = pg.GraphicsWindow(title = nameWindow)
184     win.resize(1200,800)
185     win.move(300,0)

186     p1 = win.addPlot(title = nameTitle1)
187     p1.setLabel('left', yLabel, units= yUnit)
188     p1.setLabel('bottom', xLabel, units = xUnit)
189     p1.showGrid(x=True, y=True, alpha = 1.0)

190     p2 = win.addPlot(title = nameTitle2, row=1, col=0)
191     p2.setLabel('left', yLabel, units= yUnit)
192     p2.setLabel('bottom', xLabel, units = xUnit)
193     p2.showGrid(x=True, y=True, alpha = 1.0)

194     app.processEvents()
195     win.show()
196     app.processEvents()
197     #------
198     plotx = np.empty(plotLength)
199     ploty = np.empty(plotLength)
200     plotx.fill(None)
201     ploty.fill(None)

202     plotx2 = np.empty(plotLength)
203     ploty2 = np.empty(plotLength)
204     plotx2.fill(None)
205     ploty2.fill(None)

206     return plotx, ploty, plotx2, ploty2
207 ##### END: Live plot initiate #####

208 ##### Data file header #####
209 ''' File Header '''
210 def filehead(f,filename):
211     #f.write("#GMW3470@VFPS: " + filename + " \n")
212     f.write("#GMW5403@MOKE: " + filename + " \n")
213     f.write("#Start: "+ str(startTime)+"\n")
214     f.write("#\n")
215     #f.write("#Bias(Keithley):: "+str(Idc)+" uA\n")
216     f.write("#Bias(Keithley):: "+str(Vdc)+" mV\n")
217     f.write("#Modulation:: field by Lock-in["+oscFrq2+", "+oscAmp2+"
    ↪  ("+str(Hmod)+" Arms)]\n")
```

```
218     #f.write("#SRS:: SEN(" + str(lockSEN) + "), TC(" + str(tc) + "s),
    ↪ phase(" + str(refphase) + "), offset(off)\n") #:: SR7225:: SEN(" +
    ↪ str(lockSEN2) + "), TC("+str(tc2) + "s), ACgain(" + str(acgain2) +
    ↪ "), phase(" + str(refphase2) + "), offset(off)\n")
219     f.write("#SR7225:: SEN("+str(lockSEN2)+"), TC("+str(tc2)+"s),
    ↪ ACgain("+str(acgain2)+"), phase(" + str(refphase2) + "),
    ↪ offset(off)\n")
220     f.write("#Microwave (ag+DCBlock):: pwr(" + str(pwr) +
    ↪ "dBm)::Sec1(4ft)Sec2(2x6ft)_stepF(0.002)_ag_-10dB@ag_front\n")
221     f.write("#Field:: Field wait("+str(waitH)+" sec),
    ↪ maxH("+str(maxH)+"kG)\n")
222     f.write("#Data:: dataAvg("+str(dataAvg)+")\n")
223     f.write("#f(GHz) SR7225_x SR7225_y \n")# SRS_x SRS_y \n")
224 ##### Data file header #####

225 ##### Utility #####
226 def falseRead(mw_device, lockin, freq, *args):
227     if 'offon' in args:
228         print 'mw OFF: ... ', outputOFF(mw_device)
229         time.sleep(waitMW)
230         print 'f = ', freq, ' GHz ', setF(mw_device,freq)
231         time.sleep(waitMW)
232         print 'mw ON: ... ', outputON(mw_device)
233         time.sleep(waitMW)
234     else:
235         print 'f = ', freq, ' GHz ', setF(mw_device,freq)
236         time.sleep(waitMW)

237     time.sleep(waitLockin2) #time.sleep(waitLockin)
238     print '===== false reading: ON ====='
239     for n in np.arange(0, 10, 1):
240         #measureSRS830(lockin, 10) #False reading
241         measureLockin(sr7225, 10, lockSEN2)
242     time.sleep(1)
243     print '===== false reading: DONE! ====='

244 ##### End of measure routine #####
245 def removeField(target):
246     print "Removing Field...."
247     gotoH2(sr7225, target, 0.05)

248 ##### Connecting equipments #####
249 def connectEquip():
250     ###################################''' CONNECT TO EQUIPMENT '''
251     #os.system('cls')
```

```
252     global kly, srs830, sr7225, ag, yo, sa
253     global lockSEN, refphase, tc, oscAmp, oscFrq, waitLockin
254     global lockSEN2, refphase2, tc2, acgain2, slope2, oscAmp2, oscFrq2,
    ↪   waitLockin2

255     print '\n'
256     print '=============== Connecting to Equipments ==============='
257     print 'Instruments found: ',visa.get_instruments_list(),'\n' # Check
    ↪   all equip. connections

258     #yo = visa.instrument('GPIB0::1')


259     sr7225 = visa.instrument('GPIB0::12') #SR7225 Lock-In
260     print sr7225,('...is... \n'),sr7225.ask('ID')
261     lockSEN2 = float(sr7225.ask('SEN.'))
262     refphase2 = str(sr7225.ask('refp.'))
263     acgain2 = str( int(sr7225.ask('ACGAIN'))*10 )+'dB'
264     slope2 = str(( int(sr7225.ask('slope'))+1 )*6)+ 'dB/oct'
265     tc2 = str(sr7225.ask('tc.'))
266     #ie2 = str(sr7225.ask('ie'))
267     oscAmp2 = str(sr7225.ask('oa.'))+' Vrms'
268     oscFrq2 = str(sr7225.ask('of.'))+' Hz'
269     waitLockin2 = float(tc2)*5.0
270     print 'tc2',tc2
271     print 'waitLockin2',waitLockin2

272     #print '\n__________\nRohde and Schwarz is being connected to ...
    ↪   '
273     #rs = visa.instrument('GPIB0::28')
274     #print 'Identity of ... ', rs, ' is ... \n', rs.ask('*idn?')
275     #print 'RS initialized. \n__________\n'


276     kly = visa.instrument('GPIB0::28') #Keithley 2400 Soucemeter # 25
    ↪   at VFPS
277     print kly,('...is... \n'),kly.ask('*IDN?')

278     ag = visa.instrument('GPIB::9') #Agilent
279     print ag,('...is... \n'),ag.ask('*IDN?')
280     ##ag.write('*RST')
281     ##print '\n__________\nFollowing device has been reset\nag on
    ↪   GPIB0::40 is ... ', ag, '\nIts identity is
    ↪   ...',ag.ask('*IDN?'),'\nSystem error? ...',
    ↪   ag.ask(':system:error?'),'\n__________\n'
```

```
282     #outputOFF(ag)

283     #ht = visa.instrument('GPIB0::30') #Hittite
284     #print ht,('...is... \n'),ht.ask('*IDN?')
285     #ht20.write('*RST')
286     #print '\n__________\nFollowing device has been reset\nht20 on
    ↪   GPIB0::40 is ... ', ht20, '\nIts identity is
    ↪   ...',ht20.ask('*IDN?'),'\nSystem error? ...',
    ↪   ht20.ask(':system:error?'),'\n__________\n'
287     #outputOFF(ht)

288     sa = visa.instrument('GPIB0::18::INSTR', timeout=1000000)
289     print sa,('...is... \n'),sa.ask('*IDN?')

290     """
291     srs830 = visa.instrument('GPIB0::20') #Stanford Research System
    ↪   830
292     srs830.write('rest') #need this to avoid error in reading
293     #time.sleep(1.0)
294     #srs830.write('*cls') #need this to avoid error in reading
295     #time.sleep(1.0)
296     srsid = srs830.ask('*IDN?')
297     print srs830,('...is... \n'), srsid
298     #srs830.ask('*IDN?')


299     #''' ##SRS830
300     lockSEN = float(srs830.ask('SENS?'))
301     refphase = float(srs830.ask('PHAS?'))
302     tc = int(srs830.ask('OFLT?'))
303     if tc == 4: tc = 0.001
304     if tc == 5: tc = 0.003
305     if tc == 6: tc = 0.01
306     if tc == 7: tc = 0.03
307     if tc == 8: tc = 0.1
308     if tc == 9: tc = 0.3
309     oscAmp = str(srs830.ask('SLVL?'))+' Vrms'
310     oscFrq = str(srs830.ask('FREQ?'))+' Hz'

311     waitLockin = float(tc)*5.0
312     print 'tc:', tc
313     print 'waitLockin: ', waitLockin
314     time.sleep(3)
315     #'''
316     """
```

```
317     print '\n'
318 ######## END: Connecting equipments ##############

319 ##### FR estimate #####
320 def approxFR(kG, *args):
321     if 'mode1' in args:
322         #samsung611_02_01@mode 1@VFPS
323         c1 = 2.966297918407267
324         c2 = 3.6005953346652415
325         c3 = 3.6006074217996105
326         print 'mode 1 is used'
327     if 'Pstate' in args:
328         #samsung611_02_01@mode 3@VFPS
329         c1 = 3.0088696737758966
330         c2 = -3.6429232619043233
331         c3 = -3.642920702224528
332         print 'mode 3 is used'

333     f = c1*math.sqrt((kG-c2)*(kG-c3))
334     return round(f,3)
335 ##### END: FR estimate #####

336 def yo_ramp(x):
337     now = float(yo.ask(':source:level?'))
338     if np.sign(x)*np.sign(now)<0.9:
339         print 'ERROR !!!The Yokogawa Level must be set wrong.'
340         raw_input('I freeze...')
341     step = 0.1e-6 * np.sign(x-now)
342     for y in np.arange(now,x+0.5*step,step):
343         yo.write(':source:level %g' %(y))
344         time.sleep(0.200)
345     return float(yo.ask(':source:level?'))


346 if __name__ == '__main__':
347     main()
```

C.2 __bgsubtract.py

This was the script that calculated background subtraction of the signal traces with traces taken at high field. In the high field regime, the standing waves remain similar (so long as

resistance does not change too much) but the signal does not appear at the scanned frequency range. Thus, the background subtraction helps to remove the standing wave contributions.

```
#!/usr/bin/python

from __future__ import division
import numpy as np
import os, sys, glob
import re
import matplotlib.pyplot as plt
import argparse

def numkeys(text):
    return [float(item) for item in re.findall("([-\+]*[\d\.]*\d+)",text)[2:]]

parser = argparse.ArgumentParser(description = 'Search [directory]/*combined*.txt SA traces and background subtract.')

parser.add_argument('directory', nargs = '?', action = 'store', default = os.curdir, help = 'Directory containing measurement data')
#parser.add_argument('-l','--logscale', action = 'store_true', default = False, help = 'Plot dispersion with log scale')

results = parser.parse_args()
path = results.directory

# Regex definitions for picking out correct traces
# for combined files
Hstr = "([-\+]*[\d\.]*\d+)kG"
pwrstr = "([-\+\.\d]+)dBm"
freqstr = "([\d\.]+)GHz"
numstr = "([-\+]*[\d\.]*\d+)"
#TRstr = "\((\d+)of(\d+)\)"
Vdcstr = "([-\+]*[\d\.]*\d+)mV"
# matching multiple groups in pattern gives list of tuples with group matches!

# Grab files:
datafiles = glob.glob(os.path.join(path, "*combined*.txt"))
datafiles.sort(key = numkeys)
print len(datafiles)
```

```
28 if len(datafiles) < 1:
29     print "No files found"
30     raw_input()
31     exit()

32 # Make target directory
33 # for combined files folder
34 newdir = os.path.join(path,'..','bgproc')
35 if not os.path.isdir(newdir):
36     os.makedirs(newdir)

37 print datafiles[0]

38 # Background data file (first file in list, lowest frequency)
39 data0 = np.loadtxt(datafiles[0],unpack = True)
40 N = len(data0[0])

41 for i in range(0,len(datafiles)):
42     H = re.findall(Hstr,datafiles[i])[0]
43     pwr = re.findall(pwrstr,datafiles[i])[0]
44     freq = re.findall(freqstr,datafiles[i])[0]
45     Vdc = re.findall(Vdcstr,datafiles[i])[0]
46     #print datafiles[i]
47     #print 'H',H,'pwr',pwr,'f',freq,'Vdc',Vdc
48     dstfname = os.path.join(newdir,'{:02d}'.format(i) + 'bgproc_' + H +
    ↪ 'kG_' + Vdc + 'mV_' + pwr +' dBm_' + freq + 'GHz.txt')
49     dstfile = open(dstfname,'w')
50     print dstfname
51     srcfile = open(datafiles[i],'r')
52     while True:
53         srcline = srcfile.readline().rstrip('\n')
54         if srcline[0:2] == '#f':
55             print >> dstfile,'#f(GHz) BG(W) Raw(W) Raw-BG(W)
    ↪ (Raw-BG)<BG>/BG(W)'
56         elif srcline[0] == '#':
57             print >> dstfile,srcline
58         else:
59             srcfile.close()
60             break

61     data = np.loadtxt(datafiles[i], unpack = True)
62     np.savetxt(dstfile, np.transpose([ data[0], data0[1], data[1],
    ↪ data[1]-data0[1], (data[1]-data0[1])/data0[1]*np.mean(data0[1]) ]) )

63     dstfile.close()
```